
Characteristics of Merging Shear Layers and Turbulent Wakes of a Multi-Element Airfoil

Desmond Adair
W. Clifton Horne
Ames Research Center, Moffett Field, California

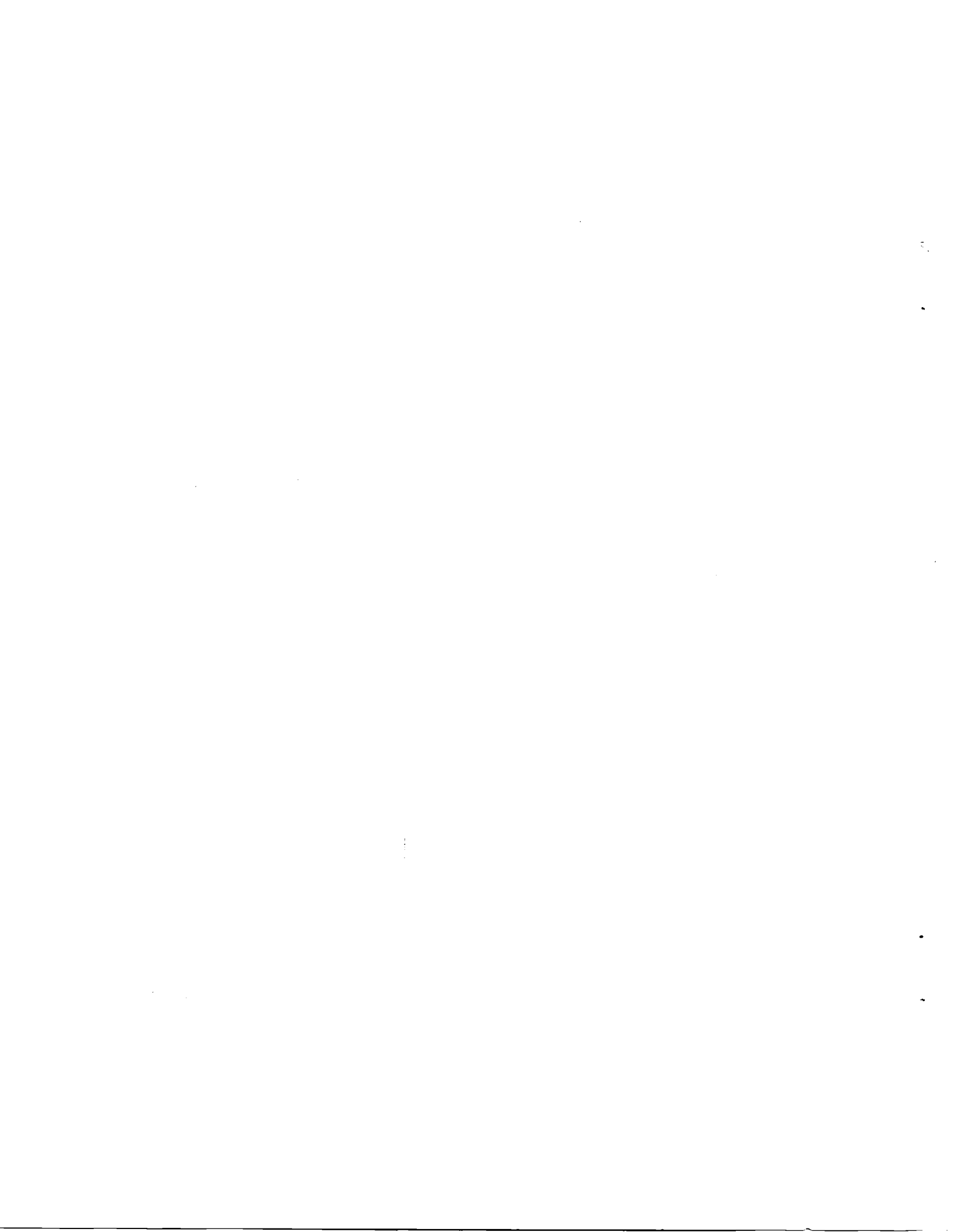
February 1988



National Aeronautics and
Space Administration

Ames Research Center
Moffett Field, California 94035

NS8-24900 #



SYMBOLS

c	airfoil reference chord
C_f	skin friction coefficient
C_L	lift coefficient airfoil lift/ $(1/2)\rho U_\infty^2 c$
C_M	moment coefficient (moment around quarter chord)/ $(1/2)\rho U_\infty^2$
C_p	pressure coefficient, $(P - P_\infty)/(1/2)\rho U_\infty^2$
FG	flap gap
FO	flap overlap
H	shape factor, δ^*/θ
k	turbulence kinetic energy
L_e^u	length scale of free-stream turbulence
n^*	location of $0.5(U_m + U_e)$
n, s	boundary-layer coordinate system over the flap (normal and tangential to local surface)
P	static pressure
R_e	reference chord Reynolds number, $\rho U_\infty c/\mu$
U_s	velocity scale
U_∞	reference free-stream velocity
U_δ	velocity at edge of flap boundary layer
u_τ	friction velocity
U, W, V	mean velocities (in boundary-layer coordinate system and in tunnel coordinates downstream)
$\langle u^2 \rangle$	U-component of turbulence energy
$\langle -uv \rangle, \langle -uw \rangle$	Reynolds shear stress

$\langle v^2 \rangle$	V-component of turbulence energy
$\langle w^2 \rangle$	W-component of turbulence energy
X,Z,Y	wind tunnel coordinate system (horizontal, vertical, spanwise)
α	angle of attack, deg
Δ	length scale of boundary-layer turbulence
δ	boundary-layer thickness
δ_f	flap deflection, deg
δ^*	boundary-layer displacement thickness, $\int_0^\delta (1 - U/U_e) dZ$
θ	boundary-layer momentum thickness, $\int_0^\delta U/U_e (1 - U/U_e) dZ$, or flap normal angle relative to vertical
μ	absolute viscosity
ν	kinematic viscosity
ρ	fluid density
ϵ	turbulence dissipation
γ_{pu}	probability of downstream velocity
$\langle \rangle$	time or ensemble average

Subscripts

e	edge of boundary layer
∞	reference free-stream quantity

Superscripts

'	perturbation from mean value
m	minimum

SUMMARY

Flow characteristics in the vicinity of the trailing edge of a single-slotted airfoil flap are presented and analyzed. The experimental arrangement consisted of a NACA 4412 airfoil equipped with a NACA 4415 flap whose angle of deflection was 21.8° . The flow remained attached over the model surfaces except in the vicinity of the flap trailing edge where a small region of boundary-layer separation extended over the aft 7% of flap chord. The flow was complicated by the presence of a strong, initially inviscid jet emanating from the slot between airfoil and flap, and a gradual merging of the main airfoil wake and flap suction-side boundary layer. Downstream of the flap, the airfoil and flap wakes fully merged to form an asymmetric curved wake.

The airfoil configuration was tested at an angle of attack of 8.2° , at a Mach number of 0.09, and chord based Reynolds number of 1.8×10^6 in the Ames Research Center 7- by 10-Foot Wind Tunnel. Surface pressure measurements were made on the airfoil and flap and on the wind tunnel roof and floor. It was estimated that the wall interference increased the C_L by 7% and decreased the C_M by 4.5%. Velocity characteristics were quantified using hot-wire anemometry in regions of flow with preferred direction and low turbulence intensity. A 3-D laser velocimeter was used in regions of flow recirculation and relatively high turbulence intensity.

Detailed measurements of pressure and velocity characteristics are reported in the following sections with emphasis on flow over the suction surface of the flap and in the downstream wake. The relative importance of the terms in the momentum and turbulence kinetic energy equations is quantified for flow in the vicinity of the flap trailing edge.

I. INTRODUCTION

During takeoff and landing, flow over the aft portion of a multi-element airfoil can be subjected to strong adverse pressure gradients and involve merging shear layers, strong interaction between the inviscid flow, nonequilibrium turbulent boundary layers, streamline curvature, and asymmetric wakes. While prediction of such a complicated flow has improved in recent years as higher-order theories such as Navier-Stokes solutions (ref. 1) are gradually developed, the current ability to calculate these flows is not yet satisfactory (ref. 2). This is due in part to the limited availability of measurements necessary for a fuller understanding of flows in the neighborhood of the flap trailing edges. Generally, present prediction methods still require that the flow remains attached on the downstream element for successful theoretical predictions of pressure, mean velocity, and Reynolds

stress. It is frequently the case, however, that optimum configurations require strong flow interaction between wakes and boundary layers (ref. 3), and between viscous and inviscid flow regions, and a limited amount of boundary layer separation.

The transport of momentum and energy by turbulence present in flow around multi-element airfoils usually plays a dominant role in determining the aerodynamic performance of airfoils equipped with mechanical high-lift systems (ref. 4). Therefore, development of mathematical models suitable for prediction of flows over and downstream of the aft section of a multi-element airfoil depends on sufficient knowledge and understanding of these turbulent processes. Of particular interest is the relative importance of the terms in the momentum and turbulence kinetic energy equations in the merging shear layers, the recirculating region, and the near wakes. An improved knowledge of the complex flow interactions associated with the confluent boundary layer and merging shear layers to which a computational model must be responsive, and for which a turbulence model is adequate, is also desirable (ref. 1).

The present work describes one of a series of experiments designed to improve the understanding of turbulent flow over high-lift airfoils as a function of the angle of attack. Similar tests have been reported by references 4 and 5 for the present two-element airfoil. The first was for a moderate flap deflection angle and had no boundary-layer separation, whereas the second had a flap deflection angle which led to massive separation over the aft 61% of the flap. Work has also been completed on the single element NACA 4412 airfoil (ref. 6) operating close to maximum lift. Progress as reported, for example, in references 7-9 has been made elsewhere in the provision of mean and turbulence field data for analysis and calculation method development of single-element trailing edge flows experiencing separation. Similar provision, with the exception of reference 10, is not evident for multi-element arrangements. Work related to the present investigation has been completed on static pressure measurements, flap optimization and mean velocity characteristics described, for example, in references 11 and 12 but turbulence quantities are not reported to any extent in these studies. Reference 13 is a report on the flow structure of the confluent region of an airfoil wake and turbulent boundary layer. Basic studies of interest to the present experiment are reported in references 14 and 15 where a confluent boundary layer and the initial region of boundary-layer separation have been investigated, respectively.

In the following sections, the surface static pressure and detailed velocity characteristics are reported for flow over a NACA 4412 airfoil equipped with a NACA 4415 flap. An emphasis is put on reporting and analyzing flow over the suction surface of the flap and on the downstream wakes. The characteristics were quantified using hot-wire anemometry and a 3-D, backscatter, laser velocimeter. The relative importance of the terms in the momentum and turbulence kinetic energy equations are quantified.

II. EXPERIMENTAL ARRANGEMENT

Wind Tunnel and Model

The test was conducted in the 7- by 10-Foot Wind Tunnel No. 1 at NASA Ames Research Center, Moffett Field, California. The closed-circuit wind tunnel has a working section 4.57 m in length, a constant height of 2.13 m, and a width which varies linearly from an initial value of 3.05 m to a final value of 3.09 m. There are no turbulence-reducing screens in the wind-tunnel circuit. The test section RMS turbulence levels, u'/U , v'/U , and w'/U , were equal to 0.0025, 0.0085, and 0.0085, respectively, for the chosen test conditions.

A cross section of the airfoil/flap configuration is shown in figure 1, and the model installation is shown in figure 2. It comprises a NACA 4412 main airfoil section equipped with a NACA 4415 flap airfoil section. The chord length (c) of the main airfoil is 0.90 m and that of the flap 0.36 m. The main airfoil angle of attack (α) was 8.2° . The geometric location of the flap relative to the main airfoil was specified by the flap gap (FG), the flap overlap (FO), and flap deflection (δ_f) as defined in figure 1. For the pressure and velocity characteristics presented in this paper, $FG = 0.035 c$, $FO = 0.028 c$, and $\delta_f = 21.8^\circ$. The model had a span of 3.05 m and was mounted horizontally in the test section to reduce optical flare when working close to the model surface. The intersections between walls and airfoil sections were sealed using felt pads to eliminate leakage between pressure and suction flows. Boundary-layer trips, about 0.15-mm thick and 4-mm wide, had a saw-tooth leading-edge. They were mounted on the suction and pressure surfaces of the main airfoil to ensure uniform flow transition across the span at x/c values of 0.025 and 0.010, respectively, from the pressure minimum. A similar trip was mounted on the suction side of the flap at an x/c value of 0.008 downstream of the flap pressure minimum.

Surface static pressures were measured at 66 static orifices located on the centerline of the main airfoil and at 42 static pressure orifices located on the centerline of the flap. Two additional chordwise rows of 56 orifices each on the main airfoil and 42 orifices each on the flap were located at 0.35-span and at 0.65-span. In addition, a spanwise row of 22 upper surface orifices was located at the 0.25-chord of the main airfoil and two spanwise rows of 12 upper-surface orifices each were located at the 0.25-chord and 0.85-chord locations on flap. The static pressure at these 350 static-pressure orifices was measured using eight 48-port scanivalves equipped with $\pm 7 \text{ kN/m}^2$ pressure transducers. The transducer voltages were digitized and recorded on magnetic tape and the data then reduced to coefficient form. Repeatability in surface pressure data proved to be good at all test conditions with a maximum change in C_p of 0.6% noted between test runs. Integration of the pressure coefficients produced the section force and moment coefficients C_L and C_M .

Test Conditions

The data presented in this paper are for a Mach number of 0.09 and a chord Reynolds number of 1.8×10^6 corresponding to a tunnel velocity (U_∞) of 30.0 m/sec. The velocity was monitored using a Pitot-static probe located 1.4 chord lengths upstream of the main airfoil leading-edge and 0.61 m from the wind-tunnel floor. Extensive probing of the wind-tunnel wall boundary layers was conducted using tufts and surface oil visualization. No evidence of boundary-layer separation could be found in those regions. The test conditions resulted in a steady flow field with no flow separation over the main airfoil but with a small region of boundary-layer separation over the aft 7% of the flap. Streamwise flow fences encircling the main airfoil were installed at 0.175-span and 0.825-span locations to shield the central airfoil section from tunnel wall boundary layer interference. Tufts and surface oil visualization showed the flow to be two-dimensional over the central 65% of the main airfoil's span. The two-dimensionality of the flow over the airfoil flap was also investigated and tuft patterns are shown on figure 3. Over a stalled flap, it has been shown (ref. 16) that the flow can depart significantly from two-dimensionality. An effort was made to alleviate this using adjustable flow fences. The fences are shown in figure 3 and extended 30% of chord length on the upper and lower sides of the flap. It was not possible to use fences which ran the full length of the flap as optical access was required by the laser velocimeter. The final positions occupied by the flow fences were at 0.36-span and 0.64-span, and the two-dimensionality of the flow in the vicinity of the flap trailing-edge was estimated to occupy 25% of the flap span.

In addition to surface oil and tuft visualization, two dimensionality of the flow was quantified using pressure and velocity characteristics. Chordwise distributions of pressure at several spanwise locations as shown on figure 4(a) were taken on the model centerline and at 482 mm to each side of the centerline, and are in good agreement. Figure 4(b) presents the mean spanwise velocity profiles over the flap and in the downstream wake at the centerline of the model. Spanwise velocities can be seen to be generally less than 3% of the free-stream velocity. Profiles of spanwise Reynolds normal stress are presented in figure 4(c) showing the development of main airfoil and flap wakes and their gradual merger. The spanwise Reynolds shear stress is also presented in figure 4(c) with values generally tending toward zero except in the near wake of the flap where values of around 7% of boundary-layer edge velocity can be found.

For the mean velocity and turbulence measurements, profiles were made normal to the main airfoil or flap surfaces upstream of the flap trailing edge as described in table 1 and figure 5. In the downstream wake, profiles were made using wind-tunnel coordinates. Table 2 presents the orientation of the profiles relative to the vertical, the development of the boundary-layer edge velocity, and the physical thickness of the boundary layers and free shear layers.

Instrumentation

Pressure characteristics were obtained using surface static pressure taps as reported in an earlier section. A sting-mounted Pitot-static tube of outside diameter 6.35 mm was used to obtain pressure measurements in the tunnel and roof boundary-layers. Vertical surveys were made at the mid-span location in the plane of the reference Pitot-static probe and at 1.5 c downstream of the flap trailing edge.

Upstream of separation and for most of the wake, the flow had a preferred direction and comparatively low turbulence intensities. In these regions it was possible to quantify the velocity characteristics with stationary hot-wire anemometry. The sensors were first orientated to measure U , W , u' , w' , and $\langle -uw \rangle$, followed by an orientation to obtain V , v' , and $\langle -uv \rangle$, where U , W , and V indicate streamwise, cross-stream, and spanwise velocities, respectively. Straight wire (DISA 55P10) and cross-wire (DISA 55P64) probes were operated with constant temperature anemometers (DISA 55M10) and the instantaneous voltages were recorded digitally using an HP1000 computer prior to analysis. The wires were operated at an overheat ratio of 1.8 and large signal amplifiers were used in the processing of the signal. The bandwidth of the data acquisition system was 20 kHz and the nonlinearized signals were sampled simultaneously at a rate of 10 samples/sec over a minimum period of 100 sec. Calibration of both flow velocity and flow angle was performed using a DISA hot-wire calibration rig with the resulting linearizations stored in the computer.

In regions of reversed flow and high turbulence intensity, a 3-D laser velocimeter (described in refs. 17 and 18) was used. The LV system, shown in figure 6, is capable of measuring all three instantaneous velocity components (U, W, V) simultaneously by means of three independent dual beam channels that operate in backscatter mode. To improve the sampling rate the method of coupling the three channels as reported in reference 15 was modified orthogonal coupling of the colors violet (476.5 nm) and green (514.5 nm) of an 8-W argon-ion laser to obtain samples of streamwise and cross-stream components of the mean velocity and the stress tensor components. This was followed by a second sample using nonorthogonal coupling of the blue (488.0 nm) and green colors to obtain the spanwise velocity. Vertical and streamwise motions of the focal volume were accomplished by moving the entire laser velocimeter on a digitally controlled platform. The repeatable positioning of the focal volume was better than 0.5 mm. The support platform was slightly yawed by 2° with respect to wind-tunnel coordinates, and was pitched downward by 2.75° to allow grazing contact of the focal volume at the semispan of the wing. The small pitch and yaw angles of the optical table result in slight coupling of all three velocity components and it is estimated that neglect of the spanwise component leads to a decrease in U , W , u' , and w' of 0.6%, 0.54%, 1.1%, and 0.92%, respectively. An inherently poor signal-to-noise ratio is common to laser velocimeters using backscatter. To alleviate the problem, it is desirable to minimize the processing bandwidth. However, this can lead to biasing of the incoming data. The present laser velocimeter incorporates programmable frequency synthesizers that generate mixing frequencies for each channel that can be varied under program control to

maintain the mean signal frequency at the center of the bandwidth. Frequency shifting by Bragg cells was employed to resolve directional ambiguity in the measured velocities.

The laser was operated at a power setting of between 1.75 and 2 W, and the effective probe volume for each channel was found to be 5 mm for the green and violet beams and 2.5 mm for the blue. A mineral oil aerosol of nominal particle diameter 5 μm was introduced into the diffuser of the closed-circuit wind tunnel to provide nearly uniform seeding in the test section.

Comparison was made between the hot-wire and laser velocimeter measuring techniques by comparing mean velocity and turbulence characteristics at two streamwise locations, the results of which are reported in reference 5. Good agreement was found between the two measuring techniques when recirculating flow was not present.

III. EXPERIMENTAL RESULTS

Mean Flow-Pressure

Static pressure distributions measured over the main airfoil and flap surfaces at mid-span are presented in figure 7. Boundary-layer separation occurred over the aft 7% of flap chord (2.8% of chord), and can be recognized by the appearance of a short region of constant pressure close to the trailing edge of the flap. A localized increase in the flap suction pressure was noted at 20% of flap chord (8% of chord), just downstream of the main airfoil trailing edge. Integration of the pressure coefficients produced the section force (C_L) and moment (C_M) coefficients for the present setting. The uncorrected values of C_L and C_M were found to be 3.19 and 0.99, respectively, and are comparable in magnitude to those reported in references 10 and 12. The coefficient of drag, C_D , was estimated as 0.066 using a velocity profile measured one chord length downstream from the flap trailing edge.

Wind-Tunnel Wall Interaction

Static pressure measurements were made along the wind tunnel centerline close to the roof and floor of the test section. These measurements are shown in figure 8 for the present study. The pressure signature on the tunnel walls extended upstream to the plane of the reference Pitot-static probe and downstream into the diffuser. Velocity profiles in the roof and floor boundary layers at the centerline of the tunnel in the plane of the flap trailing edge were obtained to give an indication of the displacement effect of the tunnel wall boundary layers. For the roof boundary layer, δ , δ^* , and θ were found to be 130 mm, 15 mm, and 12 mm, respectively. For the floor the same quantities were 146 mm, 18 mm, and 14 mm, respectively. Also presented in figure 8 are static pressure measurements taken along vertical traverses. These traverses were located at 1.4 chord lengths upstream of the main airfoil leading edge and at 1.28 chord lengths downstream of the flap trailing

edge. Flow angularity, measured using a five-tube Pitot probe in the plane of the reference Pitot probe, proved to be within $\pm 0.2^\circ$ from the tunnel centerline.

To characterize the effect of tunnel-wall interference, calculations with and without wind-tunnel walls were made using the method of reference 19. For a flap deflection of 21.8° , the wall interference caused a 7% increase in C_L and a 4.5% decrease in C_M relative to the unconfined case. The correction for C_L is in close agreement with that found when using the method for two-dimensional boundary corrections reported by reference 20. Thus it is recommended that the effect of wall interference should be taken into account when calculating this flow.

Mean Flow-Velocity

The characteristic boundaries and general organization of the flow domains are shown in figure 9 where γ_{pu} is the fraction of laser velocimeter samples having a positive value of streamwise velocity, U . Boundary-layer detachment was noted at 25 mm upstream of the flap trailing edge and a small region of intermittent separation occurred upstream of this. Negative flow was found to persist to about 27 mm beyond the trailing edge and a thin region of intermittent negative flow enveloped the mean negative flow. The maximum height of the recirculating flow was found to be 10 mm.

The mean velocity vectors are plotted in figure 10. The strength of the jet emanating from the slot between main airfoil and flap is emphasized and the basic structure of the jet is seen to persist downstream of the flap trailing edge. This is in strong contrast to the mean velocity characteristics over the flap reported in reference 5, where the flap deflection was set at 5° more than the present configuration. In that case, the jet profile was found to have dissipated 90 mm from the main airfoil trailing edge. In common with results reported for single element trailing edge separation (ref. 7) the recirculating flow was found to be relatively weak in comparison to the mean velocity above. The mean flow streamlines in the region of the flap and in the near wake are shown in figure 11. The negative mean velocity region was bounded by the zero velocity streamline. In common with the flow of reference 9, the present boundary-layer separated under the action of adverse pressure gradient with convex curvature present and the curvature of the streamlines was less than that of the surface.

Integral parameters for the flow over and downstream of the flap are presented in figure 12. The parameters were obtained by integrating the mean velocity profiles from and in a direction normal to the flap surface until the flap trailing edge. Downstream of the flap trailing edge, the integration was carried out across the entire wake in a vertical direction. Shown in figure 12 is the development of the displacement and momentum thicknesses for the flap boundary layer, the main airfoil wake and the wake downstream of the flap trailing edge. Integration across the main airfoil wake showed that both displacement and momentum thickness steadily increased as the shear layer met increasingly adverse pressure gradients. In the wake, the same quantities gradually decayed and the shape factor (H) defined as δ^*/θ asymptotically approached 1.0. Integration of the mean velocity profiles for

the inner flap boundary layer up to the edge of the low turbulence jet indicated a steady growth in the shape factor. H was found to be 2.89 at 25 mm upstream of the flap trailing edge, and just upstream of the flap trailing edge, it was found to be 3.6. Care should be taken when interpreting the shape factor because of the fact that the jet flow has significant turbulence present especially close to the trailing edge. Reference 21 has shown that this may lead to an overestimation of the shape factor.

Profiles of streamwise mean velocity are shown in figure 13 for the 22 stations of table 1. The velocity profile over the main airfoil is consistent with that boundary layer in an adverse pressure gradient. Just downstream of the main airfoil trailing edge (station Nos. 4-6), the turbulent boundary layer on the flap was found to be initially thin but gradually broadened with downstream distance. The magnitude of the reversed flow in the vicinity of the trailing edge was very small with a maximum of 1.2 m/sec noted. The initially inviscid jet dominates the near wall flow over the flap. The jet flow structure can be seen in the mean velocity profile beyond the flap trailing edge at x/c of 1.322 (station No. 14) separating the main airfoil and flap wakes. In the near wake, the strength of the jet gradually decayed and at 400 mm (station No. 17) downstream of the main airfoil trailing edge, only a remnant of the jet remained. Downstream, the main airfoil and flap wakes fully merged. Profiles farther downstream were similar to that at station No. 18 indicating the development of an asymmetric wake.

The cross-stream velocity is presented in figure 14. Generally its value over the main airfoil and initial flap surfaces tended to zero. In the vicinity of the flap trailing edge, cross-stream velocities in the outer region of the airfoil wake reach values of up to 40% of edge velocity and close to the surface negative values of just less than 20% of edge velocity are found. Strong variations in cross-stream velocity were found in the wake close to the flap trailing edge. This variation tends to diminish with streamwise distance until an almost zero cross-stream velocity profile is noted at x/c of 2.558 (station No. 22).

The laser velocimeter gave information on the probability of downstream flow, γ_{pu} , in the vicinity of separation as shown in figure 15. Intermittent reversed flow started at 9% of flap chord length from the flap trailing edge and the γ_{pu} values decreased with downstream distance. γ_{pu} was never found to be zero, indicating no constant fully reversed flow in any part of the recirculating flow. The lowest value of γ_{pu} was found to be 0.2 just after the flap trailing edge.

Turbulence

The development of Reynolds stresses over the main airfoil and flap suction surfaces and in the downstream wake are shown in figures 16-18. Comparison of the data obtained at $x/c = 0.989$ (station No. 3) with that obtained at $x/c = 1.031$ (station No. 5) in figures 16 and 17 shows that there was a slight change (10%) in the level of turbulence energy near the centerline of the wake as the boundary layer on the upper surface of the wing moved into the near wake. The peak in the streamwise Reynolds normal stresses originating from the main airfoil suction-side

boundary layer continued to increase with streamwise distance until the flap trailing edge. This well-accepted trend for flows in strong adverse pressure gradients is also noted for the peak in the streamwise Reynolds normal stresses originating from the main-airfoil pressure-side boundary layer. Just before the trailing edge, these dual peaks have merged to form a broad maximum for the streamwise Reynolds normal stress profiles (fig. 16) whereas a distinct minimum still existed in the cross-stream Reynolds normal stress profiles (fig. 17) in the region of jet flow. The flap boundary layer was found to be initially thin with low turbulence present. Downstream at the flap trailing edge ($x/c = 1.308$ (station No. 12)) this inner layer was still relatively thin but the peak value of streamwise Reynolds normal stresses had increased dramatically (by 130%) when compared to its value at $x/c = 1.031$ (station No. 5). This marked increase in the turbulence level for the inner flap boundary layer close to the flap trailing edge was also found for the cross-stream Reynolds normal stresses. A gradual increase in the turbulence level accompanied by a reduction in its width with streamwise distance was noted for the low turbulence region of jet flow.

The Reynolds shear stress profile (fig. 18) just downstream of the main airfoil trailing edge ($x/c = 1.031$ (station No. 5)) shows a 40% increase in its peak value when compared to the profile at $x/c = 0.989$ (station No. 3). The negative peak in the Reynolds shear stress profile emanating from the pressure side main airfoil boundary layer was found to grow more negative with streamwise distance over the flap. The value of Reynolds shear stress increased in the thin inner flap boundary layer with streamwise distance and on approaching boundary layer separation its value tended to zero very close to the flap wall. Its value did not go negative as would be expected when boundary layer separation is present, possibly because of the limitations of the 3-D laser velocimeter in making measurements close to the flap surface.

In the region just downstream of the flap trailing edge, for about 50 mm, both the streamwise and cross-stream Reynolds normal stress profiles were double peaked and did not exhibit much change near the wake centerline. The suction-side peak in the streamwise Reynolds normal stress profiles (fig. 16) increased by some 25% in this region whereas the turbulence energy in the pressure side peak remained fairly constant. Downstream rapid changes occurred in the Reynolds normal stress profiles (figs. 16 and 17) near the wake centerline, and for both streamwise and cross-stream components the pressure side peak gradually decayed and broadened across the layer. The streamwise Reynolds normal stresses (fig. 16) developed single peaked profiles just after $x/c = 2.558$.

In the very near wake, the Reynolds shear stress remained fairly constant in the suction-side shear layer even under the combined influence of adverse pressure gradient and destabilizing streamline curvature. There was a slight increase in its positive peak value from $x/c = 1.336$ (station No. 15) to $x/c = 1.558$ (station No. 18) after which there was a gradual decay. The negative peak in the Reynolds shear stress profile gradually decayed from just downstream of the flap trailing edge to $x/c = 1.808$ (station No. 19) after which it remained fairly constant until the final profile measured at $x/c = 2.558$ (station No. 22).

IV. DISCUSSION

The flow in the vicinity of the main airfoil trailing edge was subjected to adverse pressure gradients with no boundary layer separation present. A universal velocity profile has been proposed in reference 23 for such flows providing that for a given velocity profile $(\langle -uw \rangle)_{\max} / u_{\tau}^2 > 1.5$ (as was found in the present flow) where u_{τ} is the friction velocity. The proposed similarity parameters used in the universal velocity profile were a velocity scale U_s and a length scale Δ , where

$$U_s = 8 \left[\left(\frac{\Delta}{L} \right)^{1/2} \right] [\langle -uw \rangle^{1/2}]_{\max} \quad (1)$$

and

$$\Delta = 2.86\delta * \left[\frac{U_e}{U_s} \right] \quad (2)$$

L is the distance from the wall to the maximum shear location. Velocity profiles measured in the suction-side boundary layer of the main airfoil are compared with the Perry-Schofield proposal in figure 19. Good agreement is noted except for the profile taken at the trailing edge. In the original Perry-Schofield analysis of attached boundary layers, the quadratic turbulence terms were neglected as making negligible contributions to the shear stress. The proposal of reference 24 to redefine $[\langle -uw \rangle^{1/2}]_{\max}$ and L using a "pseudo shear stress" to alleviate this disagreement has been used in references 25 and 26. The "pseudo shear stress" was defined as

$$\left[\langle -uw \rangle + \int_n^{\infty} \frac{\partial (\langle u^2 \rangle - \langle w^2 \rangle)}{\partial x} dn \right]_{\max}$$

Agreement between the profile taken at $x/c = 0.989$ and the Perry-Schofield proposal was improved when the "pseudo shear stress" was used. In common with the findings of reference 25, increase scatter with increasing adverse pressure gradients was noted in the velocity profiles.

Flow structure was obtained for the near wall region in the attached boundary layer and reversed flow regions over the flap. The velocity at the edge of the flap boundary layer (U_{δ}) was used to plot the Clauser charts in figure 20. It can be seen from the plots of U/U_{δ} versus $\log(nU_{\delta}/\nu)$ that a law-of-the-wall profile is evident. This is in agreement with the findings of reference 13. The skin friction (C_f) values deduced from these Clauser charts and listed in figure 20 may be in error. Normally the flow above a boundary layer has no--or at most very low--turbulence present. In the present study, the flap boundary layer lies beneath a jet whose turbulence intensity increases with streamwise distance, and it has been recently realized that a change in the combination of free-stream turbulence

intensity and length scale will cause the skin friction to change (ref. 21). The empirical parameter

$$\frac{u'}{U_\delta} \times 100 \left/ \left[\frac{L_e^u}{\delta} + 2.0 \right] \right.$$

has been suggested to correct for the imposition of free-stream turbulence on the skin friction coefficient (ref. 21). L_e^u is the length scale of the free stream turbulence defined as

$$U_e \frac{d(\langle u^2 \rangle)_e}{dx} = \frac{-(\langle u^2 \rangle)_e^{3/2}}{L_e^u} \quad (3)$$

While noting that in the present flow the free-stream length scale and turbulence was increasing with streamwise direction, whereas it was decreasing in the flow of reference 21, use of the correction technique suggests that for $x/c = 1.127$ the C_f value found from figure 20 may be estimated low by as much as 18%.

Reference 13 has proposed a single algebraic formulation to describe the mean velocity profiles for the main airfoil wake such as

$$[U - U_m]/[U_e - U_m] = \left[1 - \cos \left[\frac{\pi}{2} \left[\frac{n - n_{U_m}}{n^* - n_{U_m}} \right] \right] \right]^{1/2} \quad (4)$$

In this equation, U_e refers to the shear-layer edge velocity, n_{U_m} to the location of minimum mean velocity, and n^* to the ordinate of the point when the velocity is $0.5(U_m + U_e)$. Because of the asymmetric nature of the wake, it is evident that the wake should be subdivided with U_e representing the upper and lower shear-layer edge velocities as appropriate. Profiles of the present data taken in the main airfoil wake over and downstream of the flap are shown in figure 21. The proposed velocity profile represents the present data with reasonably good accuracy although more scatter was noted in the present measurements than found by Bario in reference 13. This is a similar result to that reported in reference 10. It would appear that the use of velocity and length scales in the form of equation (4) will successfully collapse the mean velocity profiles of the airfoil wake. Turbulence quantities are also important in this region but it is doubtful that scaling similar to that for the mean velocity profiles can be applied because of their complexity.

Reynolds shear correlation coefficient $\langle uw \rangle / [\langle u^2 \rangle^{1/2} \cdot \langle w^2 \rangle^{1/2}]$ is shown in figure 22 for flow over the suction side of the flap and including the main airfoil wake. In general, the profiles are similar in nature to those found in reference 13 with an maximum absolute value of 0.52. This higher-than-normal value (usually the Reynolds shear correlation coefficient's value never exceeds 0.48 (ref. 27)) was explained in reference 13 as being in accordance with the presence of large eddies in the turbulent flow for low Reynolds number flows. This may be the explanation, but it is also the case that the maximum correlation value found in the present flow is within experimental error of that found by reference 27.

The terms in the streamwise and cross-stream momentum equations were examined using the measurements described in the previous sections. The momentum equations in two dimensions are

$$U \frac{\partial U}{\partial x} + W \frac{\partial U}{\partial z} = - \frac{1}{\rho} \frac{\partial P}{\partial x} + \frac{\partial \langle -uw \rangle}{\partial z} - \frac{\partial \langle u^2 \rangle}{\partial x} \quad (5)$$

$$U \frac{\partial W}{\partial x} + W \frac{\partial W}{\partial z} = - \frac{1}{\rho} \frac{\partial P}{\partial z} + \frac{\partial \langle -uw \rangle}{\partial x} - \frac{\partial \langle w^2 \rangle}{\partial z}$$

The terms are plotted in figures 23 and 24 where the locations shown were at 35% and 3.5% of flap chord upstream of the flap trailing edge, and at 14% of flap chord downstream of the flap trailing edge. At the first location, the main airfoil wake and flap boundary layer had not merged; and at the second location, there was a small region of boundary layer separation close to the surface and significant turbulence in the jet. At the location in the wake some intermittent backflow was still present. For both momentum equations the viscous terms were neglected as they proved to be much smaller than the remaining terms. For the streamwise momentum equation at the upstream location, the pressure gradient is opposed mainly by the Reynolds normal and shear gradients close to the flap wall whereas convection is dominant farther out in the profile because of the presence of the low turbulence jet. Downstream at $x/c = 1.296$ the Reynolds normal and shear stress component are important close to the wall. Convection is seen to be important for $0.2 < n/\delta < 0.4$ again because of the presence of the jet. Downstream in the wake the Reynolds shear stress gradient becomes the dominant quantity in the vicinity of the flap trailing edge.

An increase by an order of magnitude in the maximum cross-stream pressure gradient was found when its value at the upstream location was compared with those in the vicinity of the trailing edge. At the station $x/c = 1.187$, the cross-stream pressure gradient is principally opposed by the Reynolds normal stress gradient with convection playing a minor role. Downstream at $x/c = 1.296$ the Reynolds normal stress gradient is important in the cross-stream momentum equation especially close to the wall in the vicinity of boundary-layer separation. This was also reported in references 8 and 12. In the wake, the cross-stream pressure gradient generally decreases across the shear layers except for a small region downstream of the flap trailing edge where large values are noted balancing convection and the Reynolds normal stress gradient terms.

The turbulence kinetic energy equation is

$$\frac{U}{2} \frac{\partial k}{\partial x} + \frac{W}{2} \frac{\partial k}{\partial z} = - \frac{\partial}{\partial z} \left(v \left(\frac{P}{\rho} + \frac{k}{2} \right) \right) - \langle uw \rangle \frac{\partial U}{\partial z} - (\langle u^2 \rangle - \langle w^2 \rangle) \frac{\partial U}{\partial x} + \epsilon \quad (6)$$

where the terms on the left-hand side are advection and on the right-hand side are turbulent diffusion, turbulent-shear-stress production, normal stress production and dissipation, respectively. The terms of the equation are plotted in figure 25. The turbulence energy equation components were examined for the same locations as for the momentum transport equations. Dissipation was not measured and appears in the imbalance of figure 25. At $x/c = 1.187$ advection was found to be important in the

jet flow whereas shear-stress production was dominant close to the flap wall and in the lower half of the airfoil wake. Close to the flap trailing edge of the wake all three terms' advection, shear stress production and normal stress production become important at various regions of the two stations examined. Shear stress production is very prominent in the near wake close to the flap trailing edge and in the main airfoil wake.

V. CONCLUDING REMARKS

Measurements of the mean values of pressure and velocity have been presented for the flow over and in the downstream wake of a single-slotted airfoil/flap configuration. The results indicate a rapid growth of turbulence in the inner boundary layer in the vicinity of the flap trailing edge. The initially inviscid jet had a dominant influence on the near wall flow over the flap and in the near wake. There is a log-linear region in the flap boundary layer but care may be needed in deducing the skin friction caused by the presence of substantial turbulence in the jet flow above. The Reynolds normal stress gradient in the cross-stream momentum equation proved to be important for the flow over the flap and in the near wake.

The model was relatively large when compared to the wind-tunnel cross-section. Thus it is recommended that the effects of wind-tunnel wall interference should be considered when calculating the flow field.

ACKNOWLEDGMENTS

The authors gratefully acknowledge the support and helpful suggestions of Mr. V. Corsiglia and Dr. L. Olson during the experimental phase of the work.

REFERENCES

1. Schuster, D. M.; and Birkelbaw, L. D.: Numerical Computations of Viscous Flowfields about Multiple Component Airfoils. AIAA Paper 85-0167, Jan. 1985.
2. Cebeci, T.; Stewartson, K.; and Whitelaw, J. H.: The Calculation of Two-Dimensional Flow Past Airfoils. Numerical and Physical Aspects of Aerodynamic Flows II. Springer-Verlag, 1983.
3. Loudet, C.: Contribution Theorique et Experimentale a L'Etude des Grilles D'Aubes en Tandem a Forte Deflexion et a Forte Change. Thesis, Institut von Karman, Belgique, 1971.
4. Olson, L. E.; and Orloff, K. L.: On the Structure of Turbulent Wakes and Merging Shear Layers of Multielement Airfoils. AIAA Paper 81-1238, June 1981.
5. Adair, D.; and Horne, W. C.: Characteristics of a Separating Confluent Boundary-Layer and the Downstream Wake. NASA TM-100046, 1987.
6. Wadcock, A. J.: Investigation of Low-Speed Turbulent Separated Flow Around Airfoils. NASA CR-177450, 1987.
7. Nakayama, A.: Measurements of Attached and Separated Turbulent Flows in the Trailing-Edge Regions of Airfoils. Numerical and Physical Aspects of Aerodynamic Flows II. Springer-Verlag, 1984.
8. Viswanath, P. R.; and Brown, J. L.: Separated Trailing-Edge Flow at a Transonic Mach Number. AIAA J., vol. 21, no. 6, 1983, pp. 801-807.
9. Adair, D.: Characteristics of a Trailing Flap Flow with Small Separation. Expts. in Fluids, vol. 5, 1987, pp. 114-128.
10. Braden, J. A.; Whippley, R. R.; Jones, G. S.; and Lilley, D. E.: Experimental Study of the Separating Confluent Boundary-Layer. NASA CR-3655, 1983.
11. van den Berg, B.: Boundary Layer Measurements on a Two-Dimensional Wing with Flap. NLR Report TR 79009U, National Aerospace Lab., Amsterdam, 1979.
12. Ljungstrom, B.: Wind Tunnel High Lift Optimization of a Multiple Element Airfoil. FFA TN AU-778, The Aeronautical Research Institute of Sweden, 1976.
13. Bario, F.; Charnay, G.; and Papailiou, K. D.: An Experiment Concerning the Confluence of a Wake and a Boundary Layer. J. Fluids Eng., vol. 104, 1982, pp. 18-24.

14. Pot, P. J.: A Wake Boundary Layer Mixing Experiment. Turbulent Shear Flows II (Ed. Bradbury), Springer-Verlag, 1979.
15. Simpson, R. L.; Chew, Y. T.; and Shivaprasad, B. G.: The Structure of a Separating Boundary Layer. Parts 1-3, J. Fluid Mech., vol. 113, 1981, pp. 23-90.
16. Winkelmann, A. E.: Flow Fields Surveys of Separated Flow on a Rectangular Planform Wing. AIAA Paper 81-0255, Jan. 1981.
17. Orloff, K. L.; Snyder, P. K.; and Reinath, M. S.: Laser Velocimetry in the Low-Speed Wind Tunnels at Ames Research Center. NASA TM-85885, 1984.
18. Snyder, P. K.; Orloff, K. L.; and Reinath, M. S.: Reduction of Flow- . Measurements Uncertainties in Laser Velocimeters with Nonorthogonal Channels. AIAA J., vol. 22, no. 8, 1984, pp. 1115-1123.
19. Maskew, B.: Program VSAERO, a Computer Program for Calculating the Non-Linear Aerodynamic Characteristics of Arbitrary Configurations. NASA CR-166476, 1982.
20. Rae, W. H.; and Pope, A.: Low-Speed Wind Tunnel Testing. Wiley, New York, 1984.
21. Hancock, P. E.; and Bradshaw, P.: The Effect of Free-Stream Turbulence on Turbulent Boundary Layers. J. Fluids Eng., vol. 105, 1983, pp. 284-289.
22. Chevray, R.; and Kovasznay, L. S. G.: Turbulence Measurements in the Wake of a Thin Flat Plate. AIAA J., vol. 7, no. 8, 1969, pp. 1641-1643.
23. Perry, A. E.; and Schofield, W. H.: Mean Velocity and Shear Stress Distributions in Turbulent Boundary Layers. Phys. Fluids, vol. 16, no. 12, 1973, pp. 2068-2074.
24. Simpson, R. L.; Strickland, J. H.; and Barr, P. W.: Features of a Separating Turbulent Boundary Layer in the Vicinity of Separation. J. Fluid Mech., vol. 79, no. 3, 1977, pp. 553-594.
25. Schofield, W. H.: Two-Dimensional Separating Boundary Layers. AIAA J., vol. 24, no. 10, 1986, pp. 1611-1620.
26. Nakayama, A.: Characteristics of the Flow Around Conventional and Supercritical Airfoils. J. Fluid Mech., vol. 160, 1985, pp. 155-179.
27. Murlis, J.; Tsai, H. M.; and Bradshaw, P.: The Structure of Boundary Layers at Low Reynolds Numbers. J. Fluid Mech., vol. 122, 1982, pp. 13-56.

TABLE 1.- VELOCITY SURVEY STATIONS (refer to figure 5)

Station number	x/c	Type of shear layer	Orientation of survey line
1	0.495	Boundary layer	Normal to airfoil surface
2	0.756	Boundary layer	Normal to airfoil surface
3	0.989	Boundary layer	Normal to airfoil surface
4	1.000	Wake	Normal to flap surface
5	1.031	Wake and boundary layer	Normal to flap surface
6	1.091	Confluent boundary layer	Normal to flap surface
7	1.127	Confluent boundary layer	Normal to flap surface
8	1.187	Confluent boundary layer	Normal to flap surface
9	1.236	Confluent boundary layer	Normal to flap surface
10	1.284	Separated boundary layer	Normal to flap surface
11	1.296	Separated boundary layer	Normal to flap surface
12	1.308	Separated boundary layer	Normal to flap surface
13	1.315	Wake with recirculating flow	Tunnel coordinates
14	1.322	Wake with recirculating flow	Tunnel coordinates
15	1.336	Wake with recirculating flow	Tunnel coordinates
16	1.364	Wake	Tunnel coordinates
17	1.447	Wake	Tunnel coordinates
18	1.558	Wake	Tunnel coordinates
19	1.808	Wake	Tunnel coordinates
20	2.058	Wake	Tunnel coordinates
21	2.308	Wake	Tunnel coordinates
22	2.558	Wake	Tunnel coordinates

TABLE 2.- SUCTION-SIDE SURFACE

Station number	x/c	U_e , m/s	$\delta_{0.995}$, mm	θ , Deg
1	0.495	49.82	18	13
2	0.756	48.92	23	17
3	0.989	46.79	36	23
4	1.000	45.00	82	8
5	1.031	44.71	88	14
6	1.091	43.52	95	28
7	1.127	42.65	114	33
8	1.187	41.6	127	37
9	1.236	40.07	152	43
10	1.284	33.20	175	43.5
11	1.296	30.30	180	43.8
12	1.308	29.35	190	44

WAKE

Station number	x/c	U_e (Upper), m/s	U_e (Lower), m/s	$\delta_{0.995}$, mm
13	1.315	35.57	29.95	190
14	1.322	33.09	29.44	195
15	1.336	31.63	29.07	197
16	1.364	30.77	28.95	205
17	1.447	30.38	28.30	200
18	1.558	29.94	28.49	203
19	1.808	28.96	28.23	206
20	2.058	28.60	28.98	210
21	2.308	28.57	28.73	215
22	2.558	28.33	28.31	220

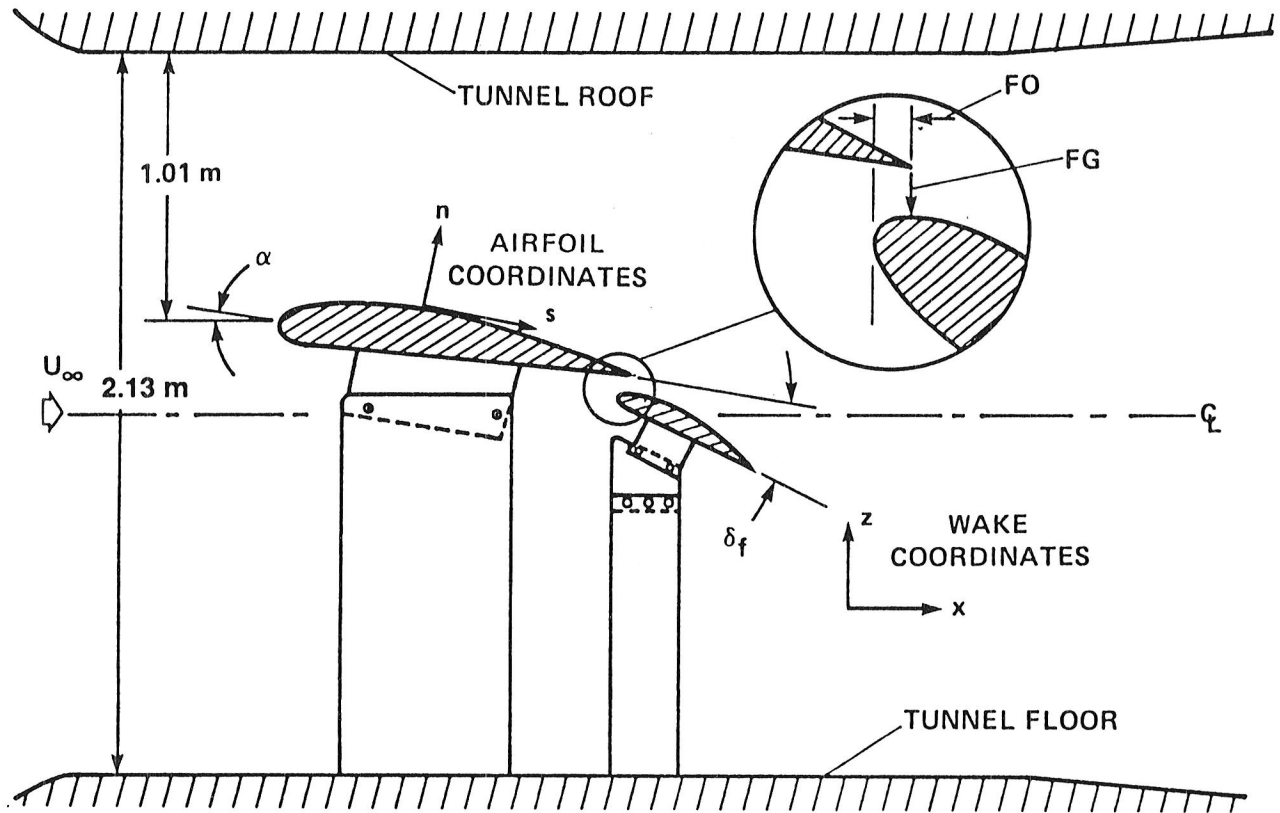


Figure 1.- Installation of airfoil in the Ames 7- by 10-Foot Wind Tunnel.

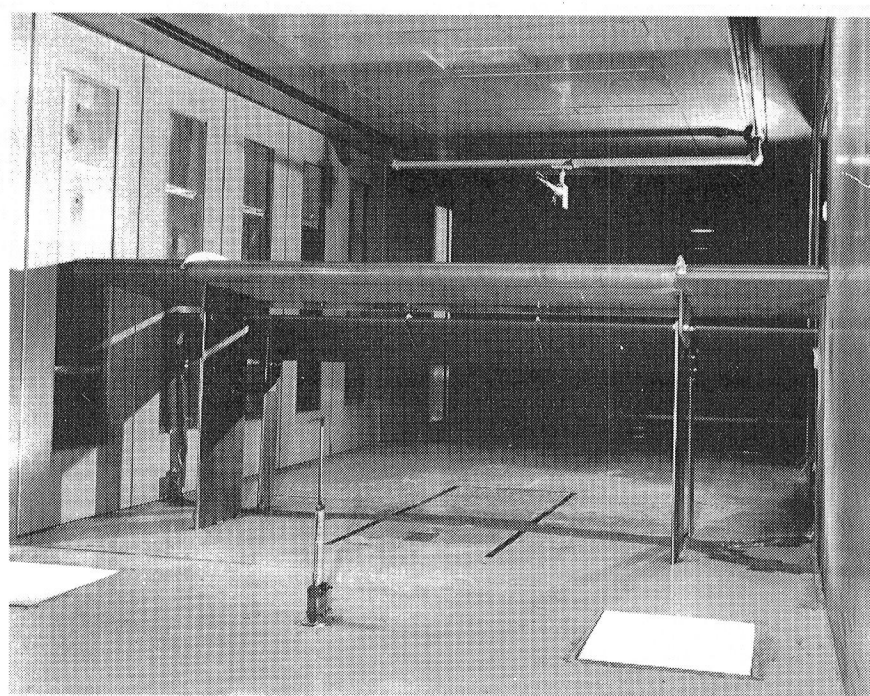


Figure 2.- Photograph of model installation in the Ames 7- by 10-Foot Wind Tunnel.

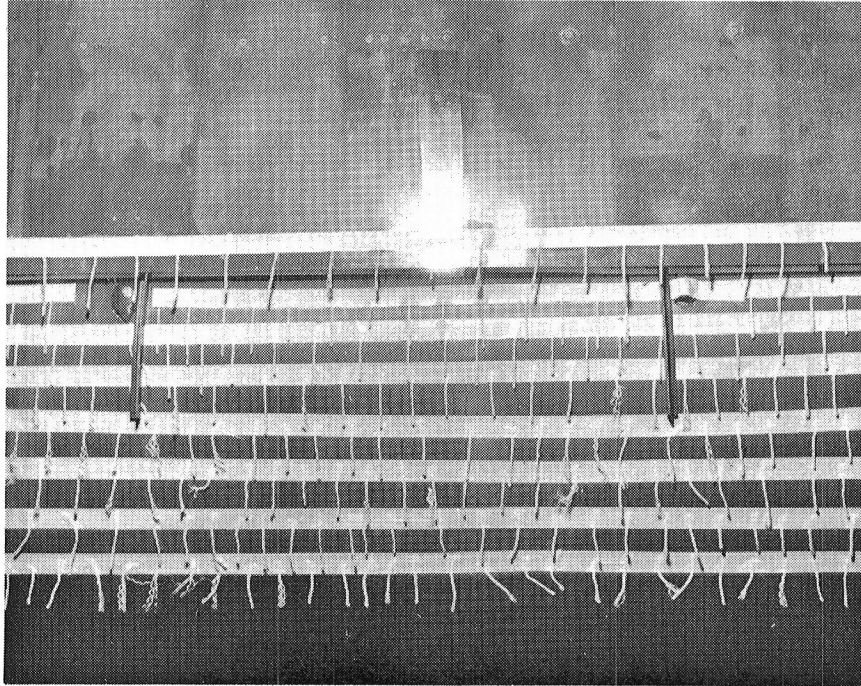


Figure 3.- Flow visualization of the flap trailing-edge region using tufts.

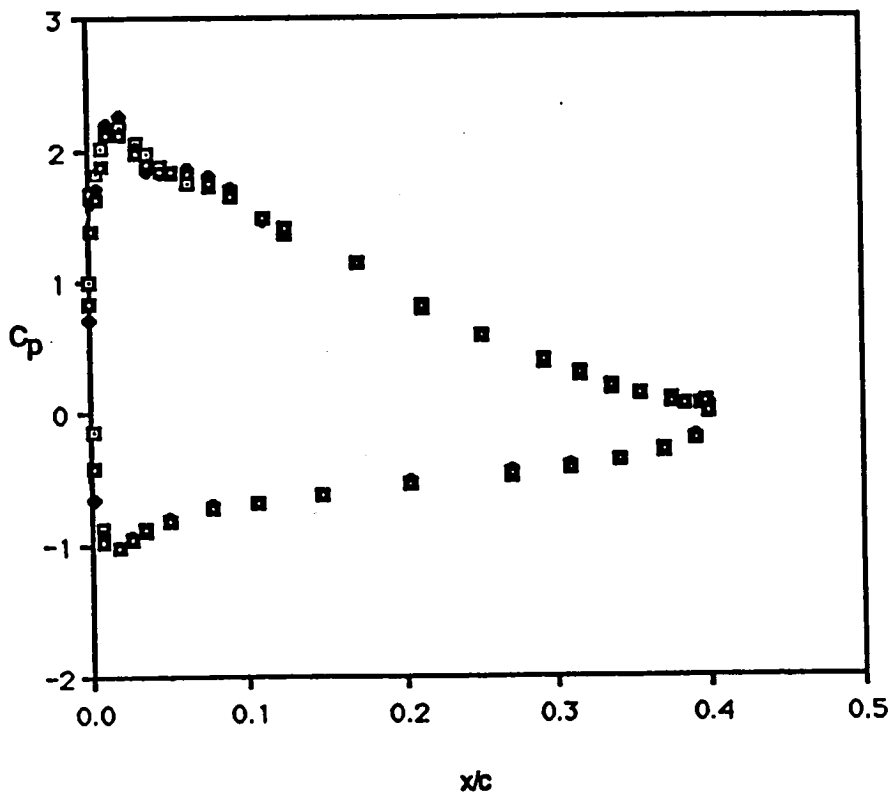
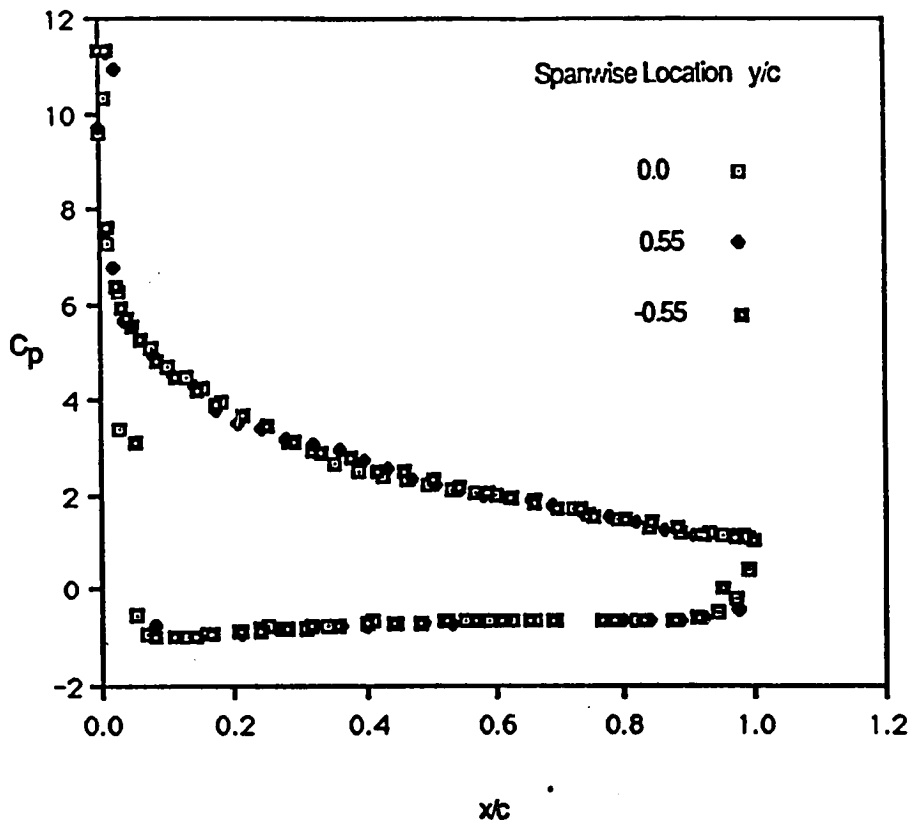


Figure 4(a).- Spanwise mean pressure measurements.

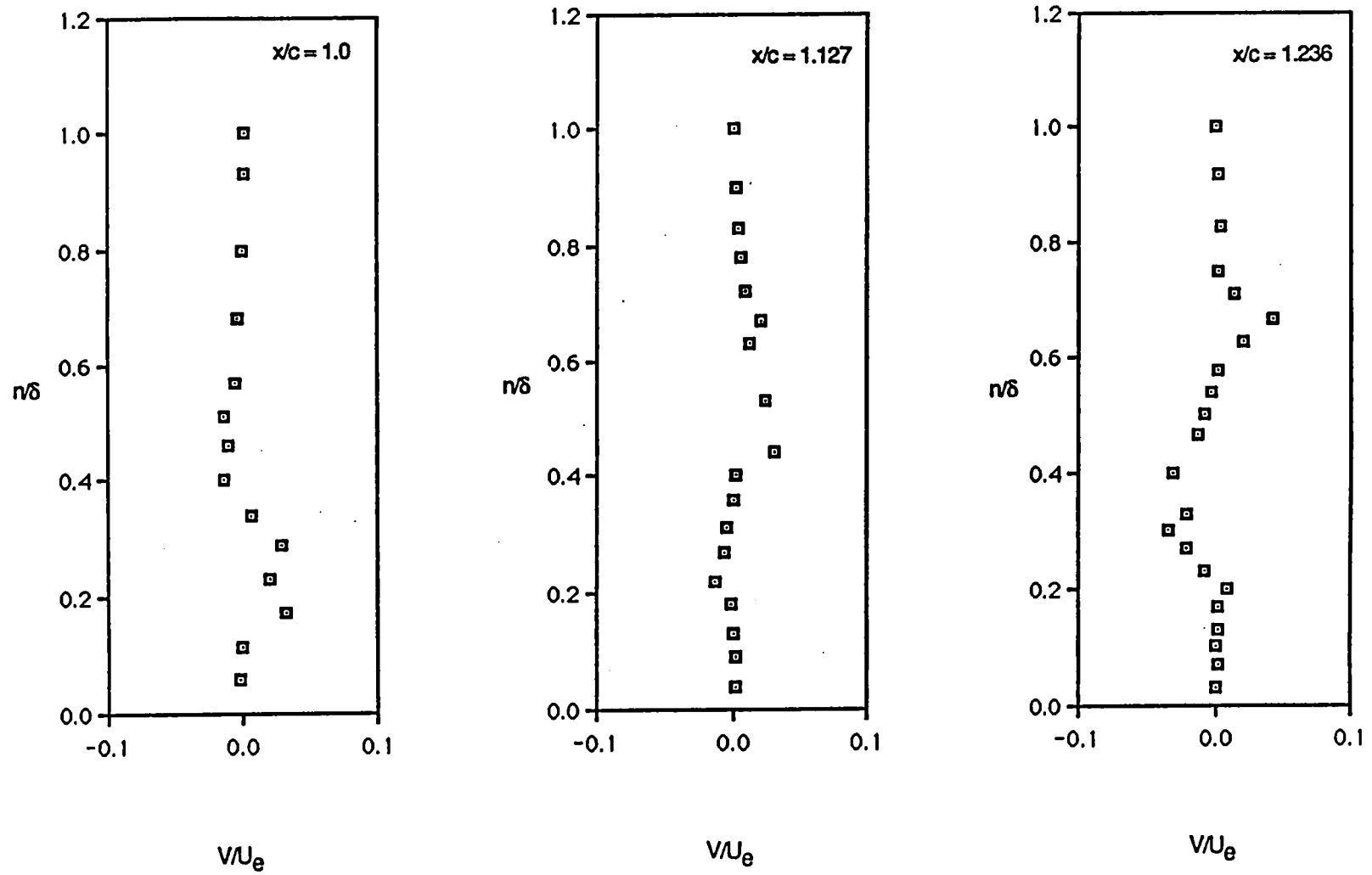


Figure 4(b).- Spanwise mean velocity measurements upstream of separation.

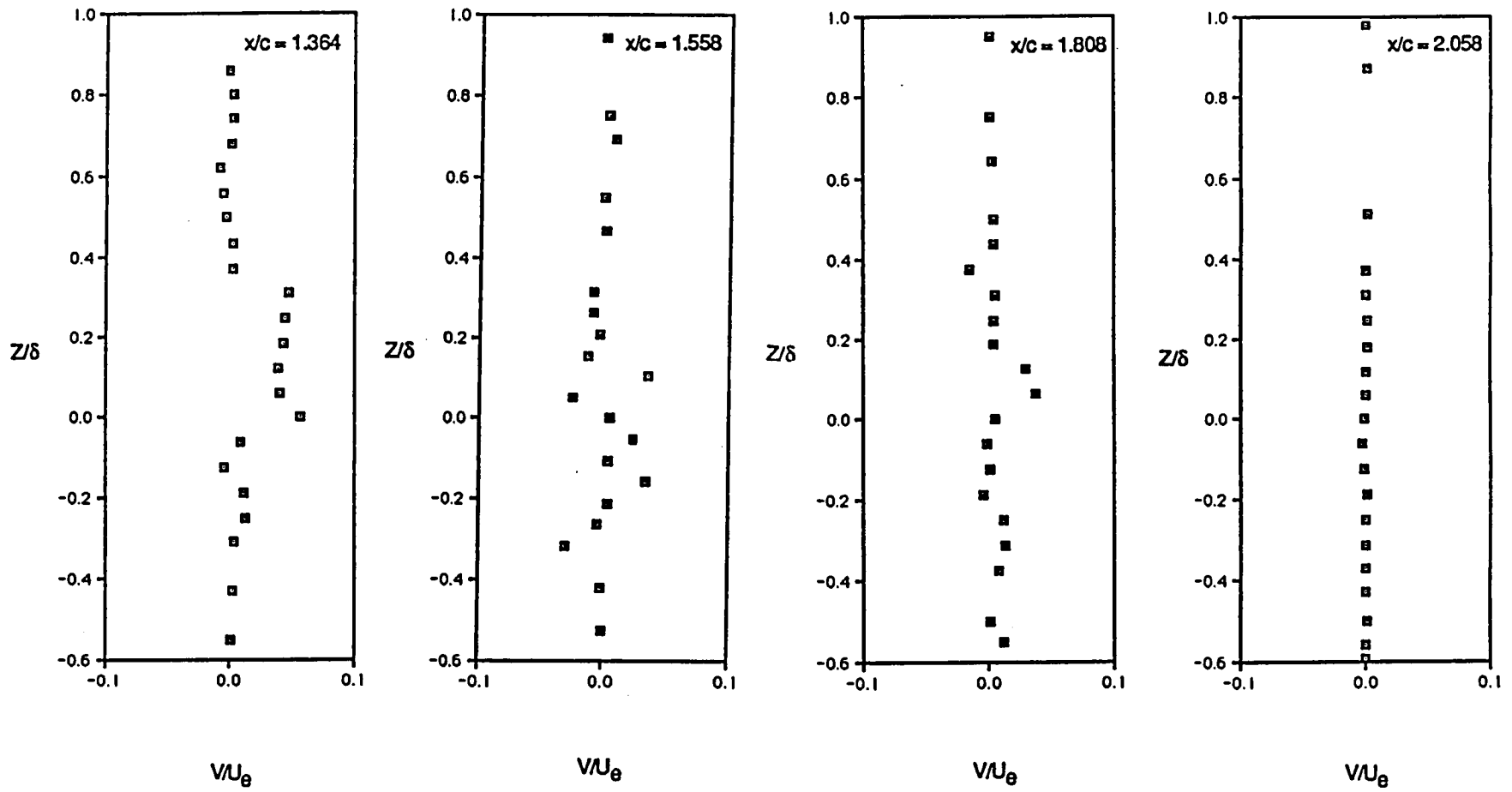


Figure 4(b).(concluded)- Spanwise mean velocity measurements in the downstream wake.

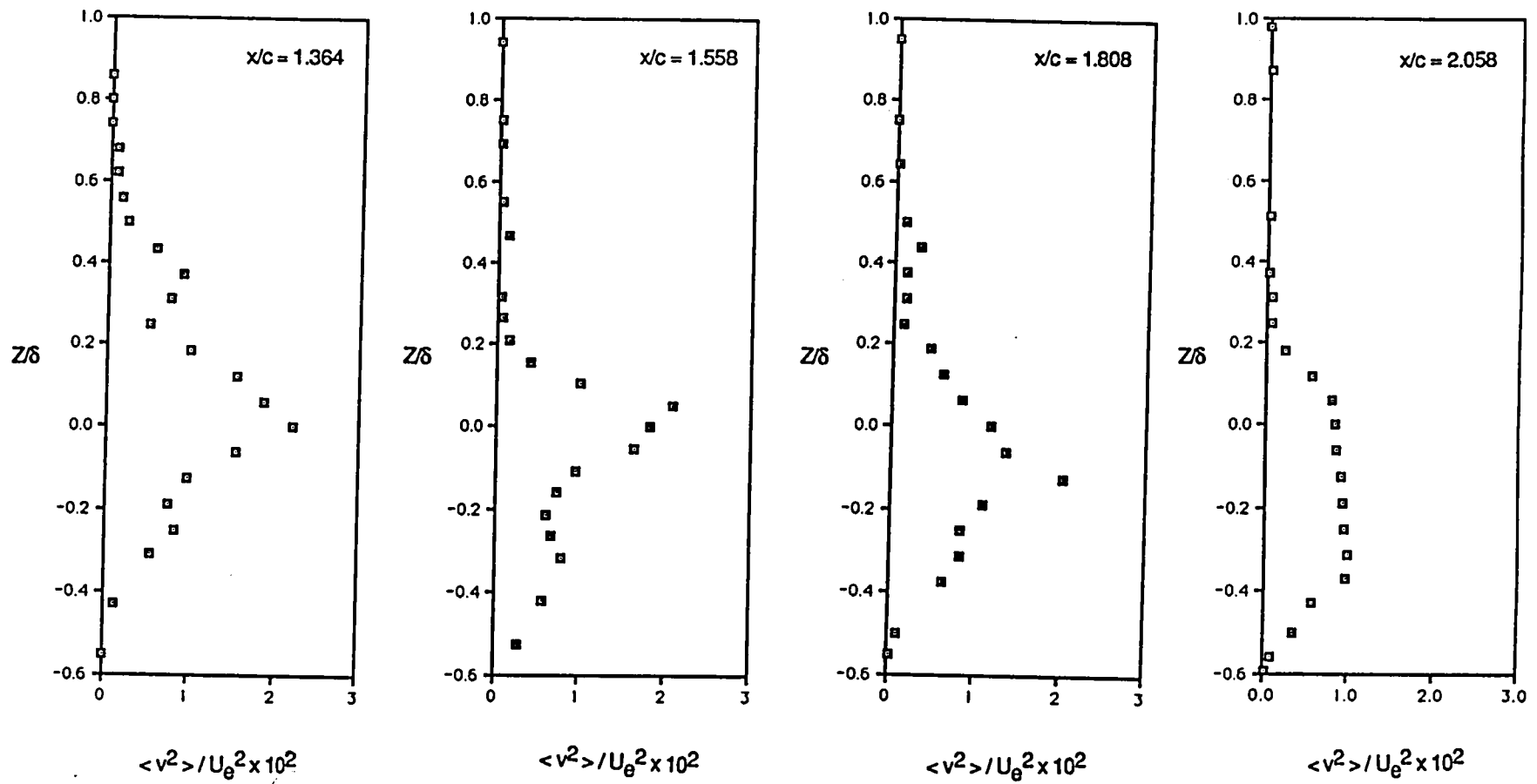


Figure 4(c).- Spanwise Reynolds normal stresses in the downstream wake.

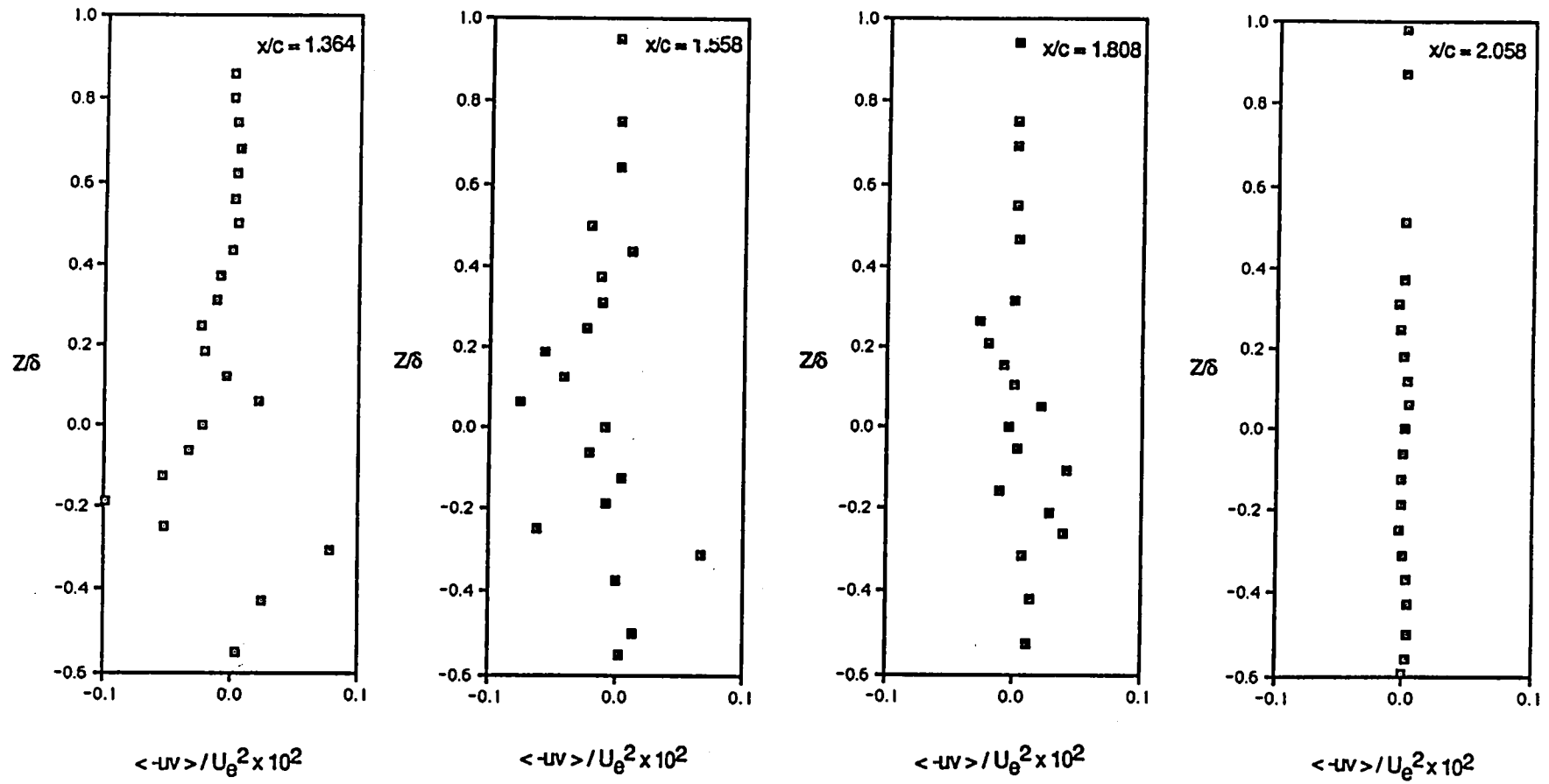


Figure 4(c).(cont'd)- Spanwise Reynolds shear stresses in the downstream wake.

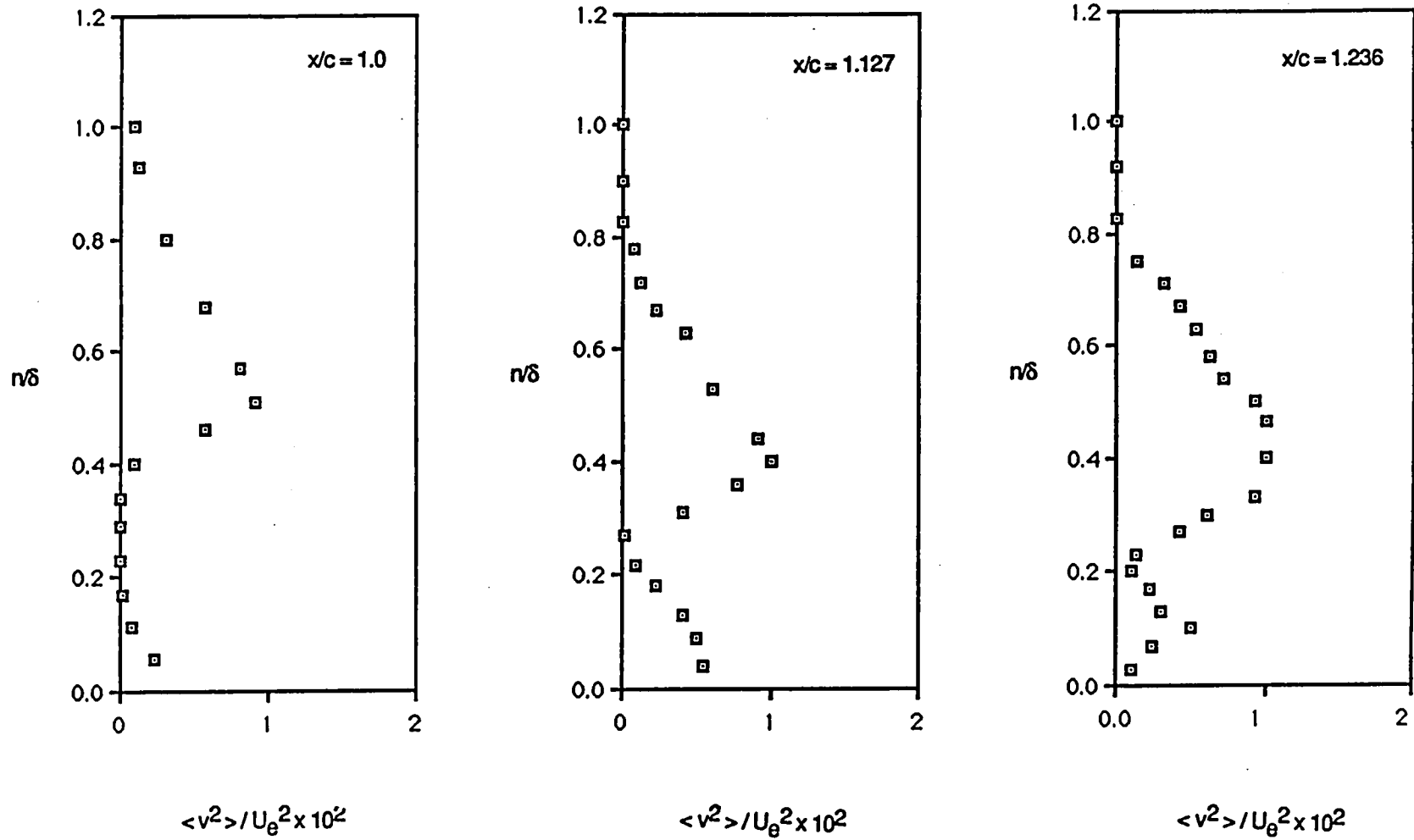


Figure 4(c).(cont'd)- Spanwise Reynolds normal stresses upstream of separation.

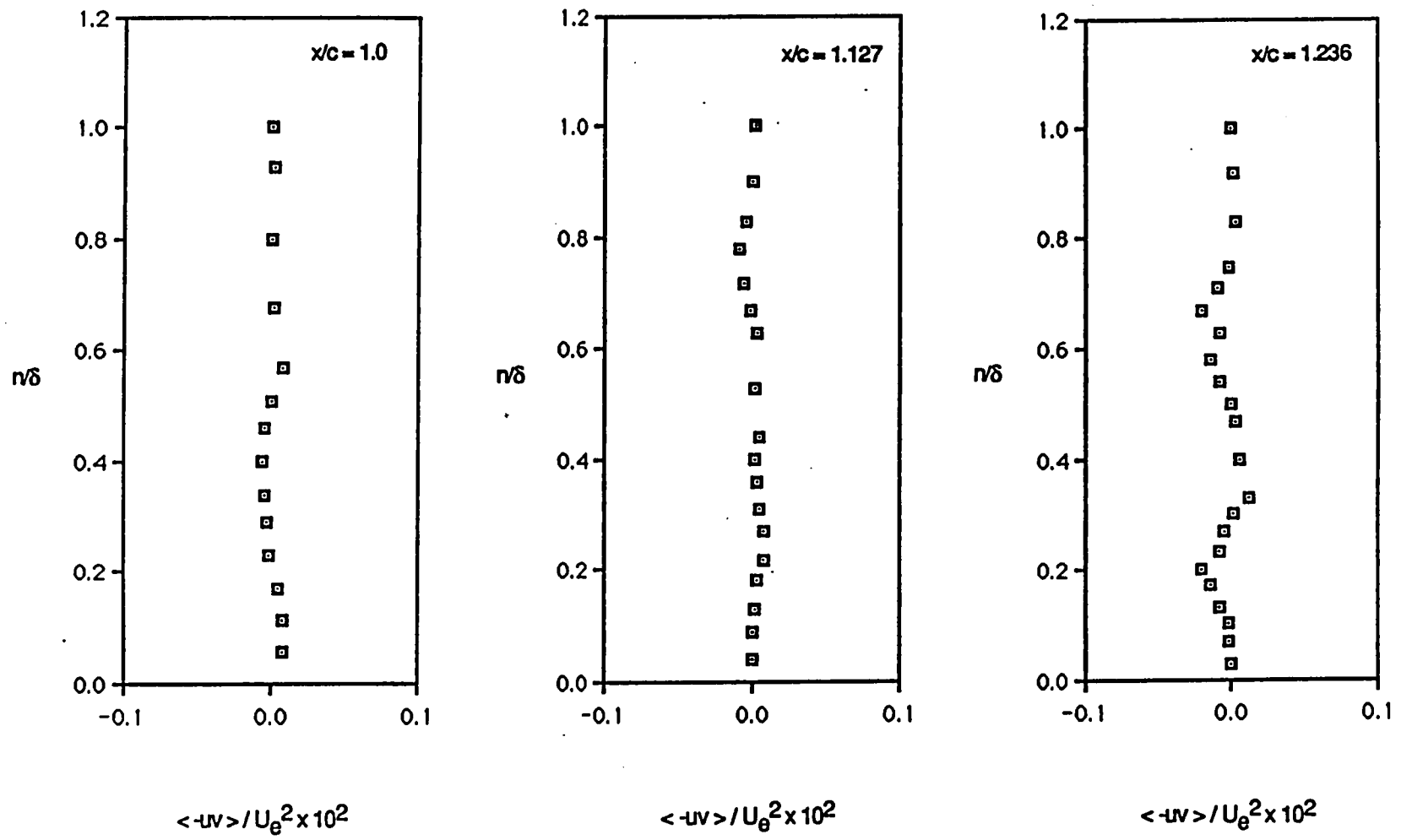
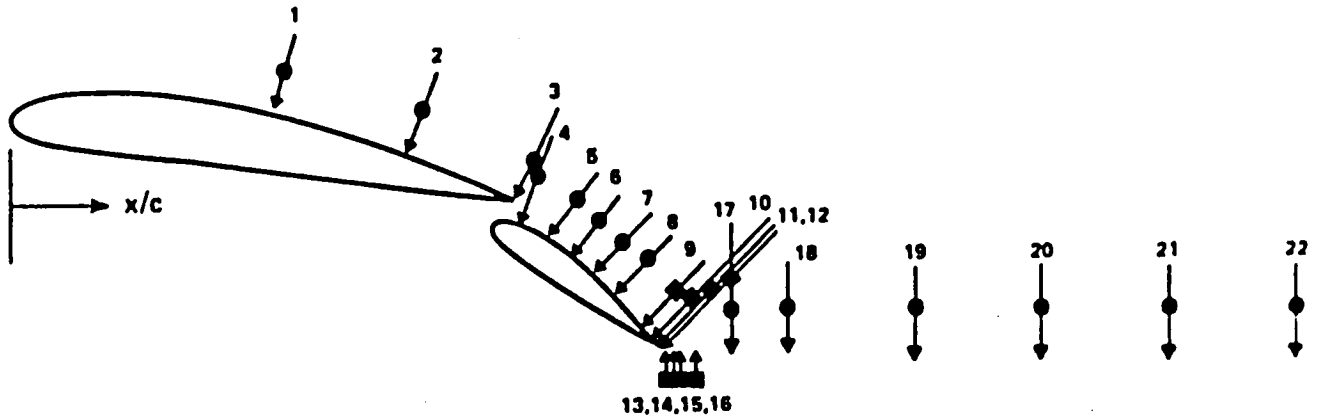


Figure 4(c).(concluded)- Spanwise Reynolds shear stresses upstream of separation.



EXPERIMENTAL PROFILES

- HOT-WIRE
- LDV

Figure 5.- Orientation and location of velocity profiles.

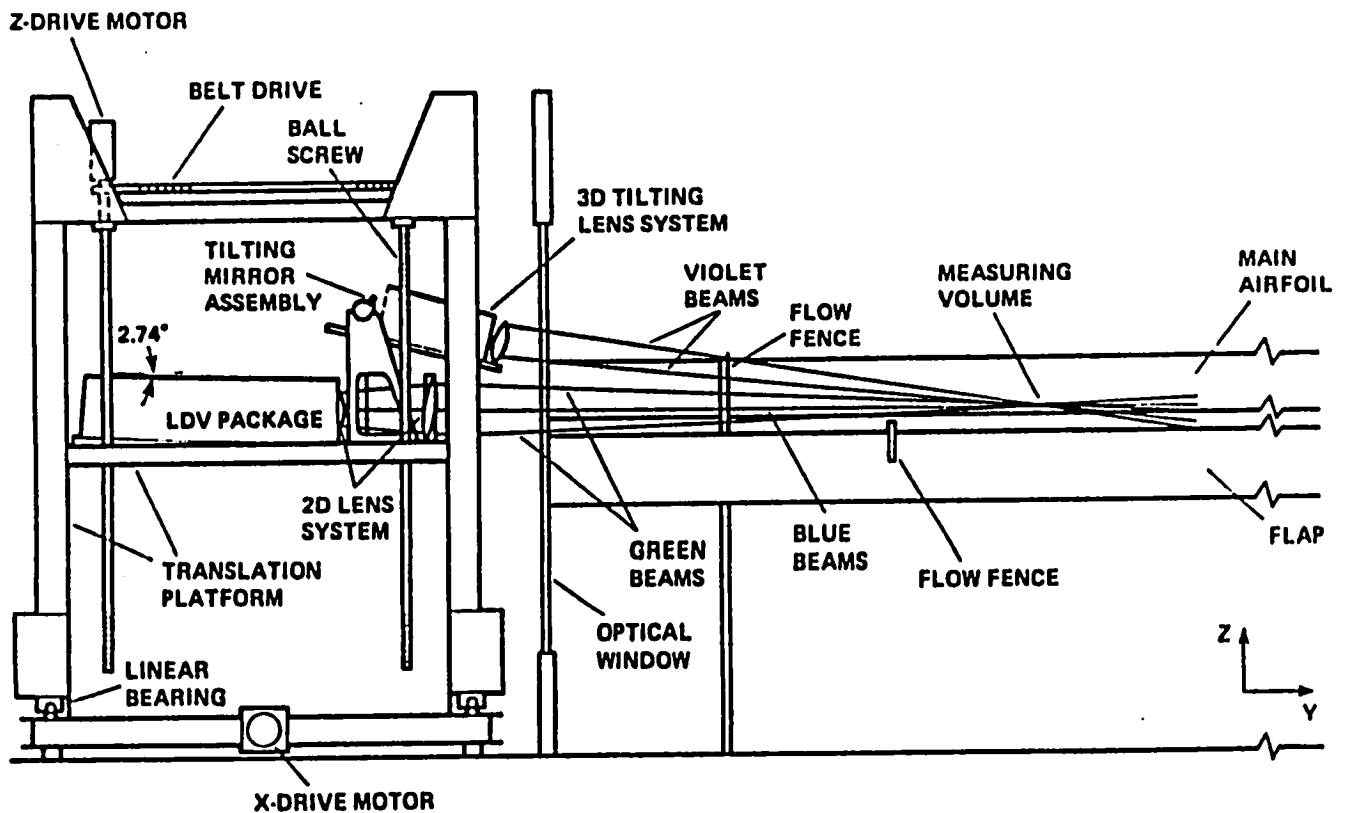


Figure 6.- 3-D Laser velocimeter in relation to the wind-tunnel and model.

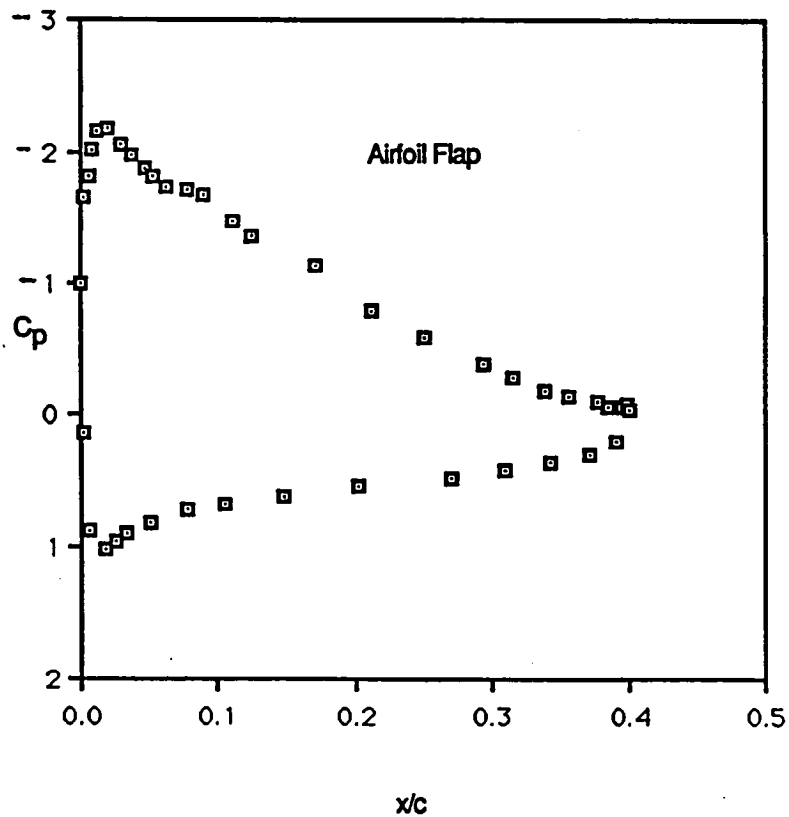
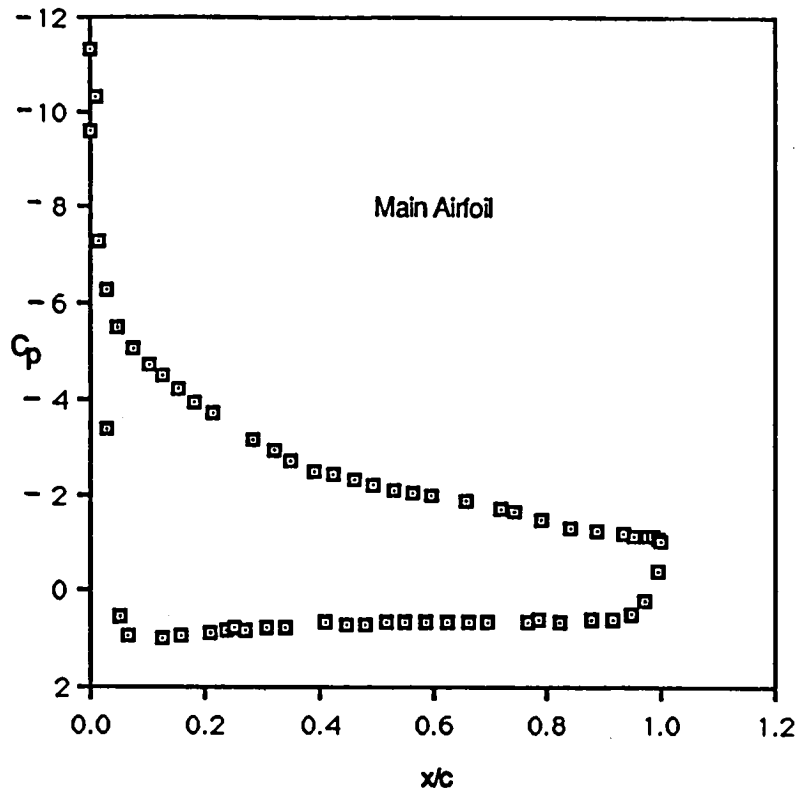


Figure 7.- Surface pressure distributions for the present configuration; $\alpha = 8.2^\circ$, $\delta_f = 21.8^\circ$, $FG = 0.035c$, $FO = 0.028c$.

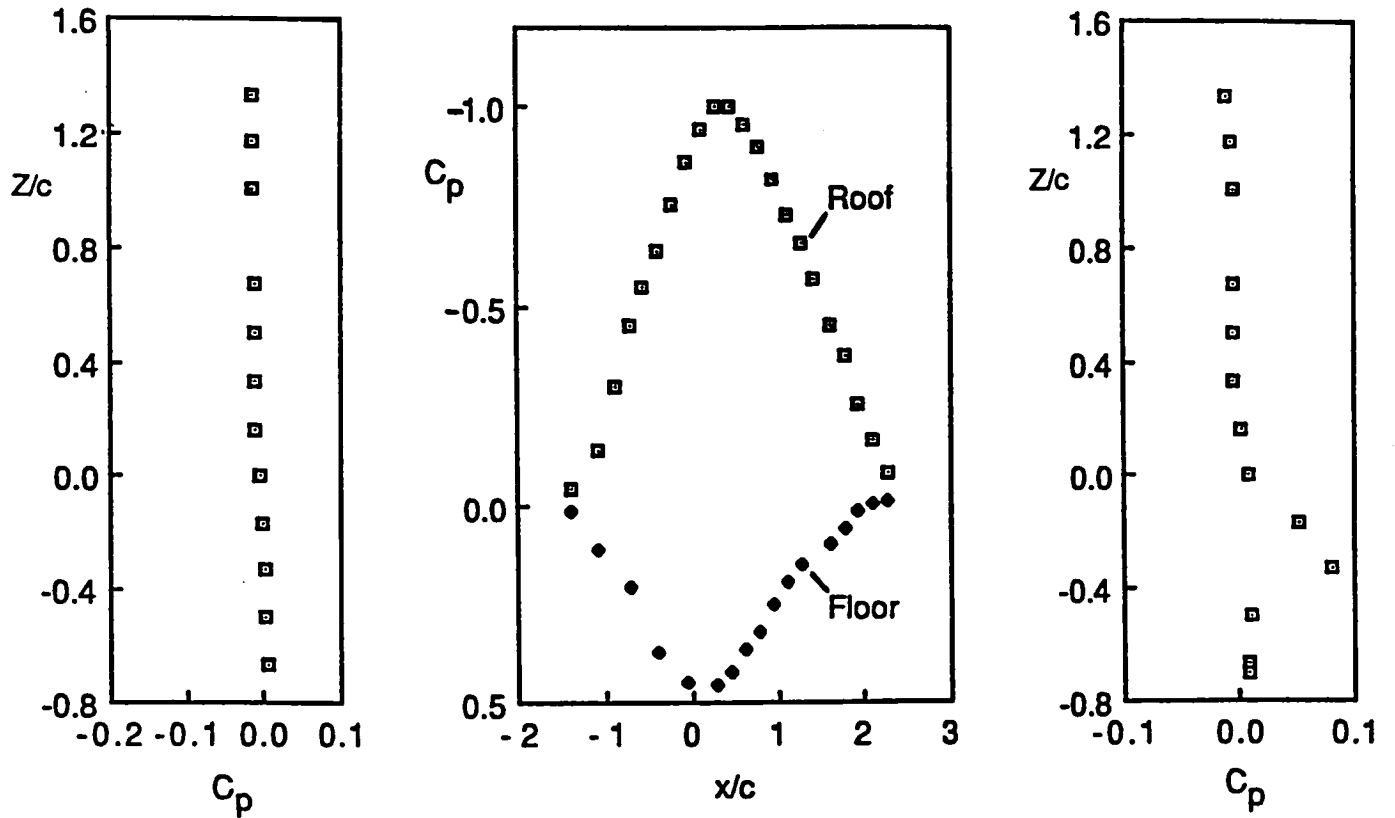


Figure 8.- Tunnel wall pressure measurements.

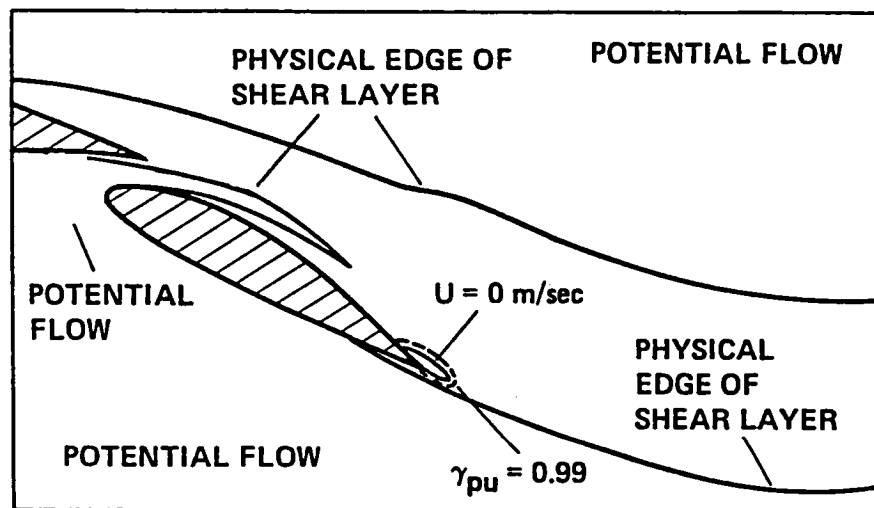


Figure 9.- Flow domains in the vicinity of the airfoil flap trailing edge.

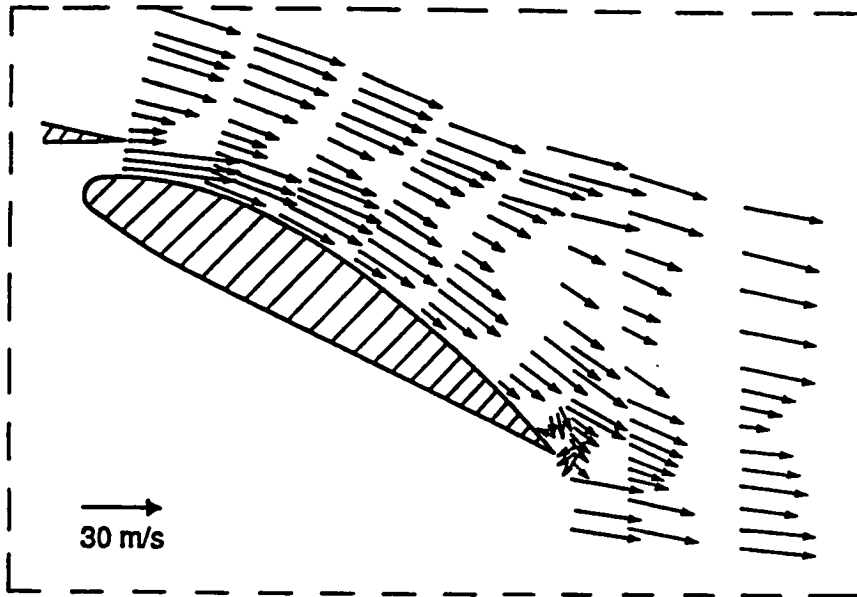


Figure 10.- Vectors representing mean velocity in the vicinity of recirculation.

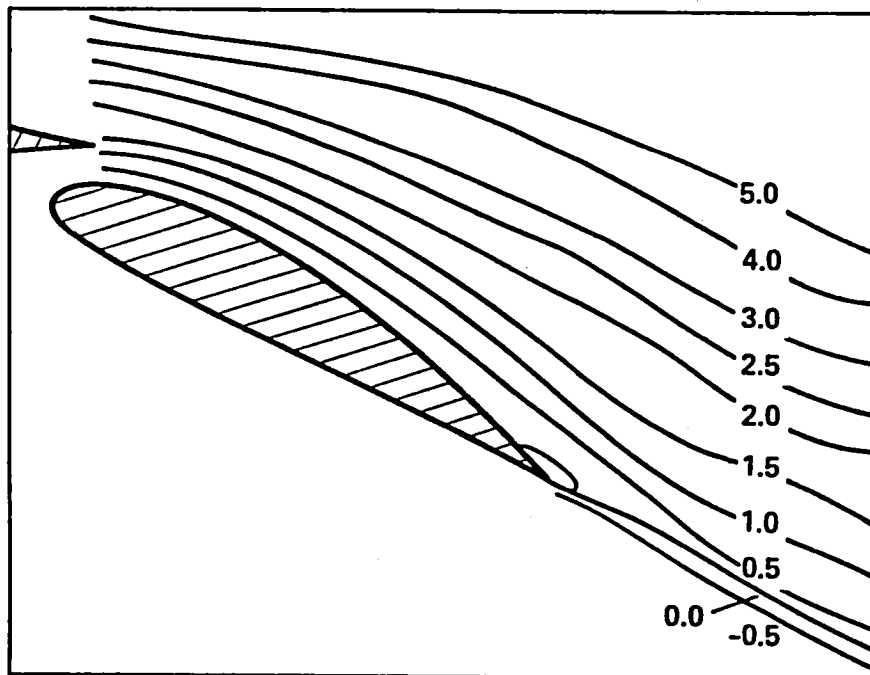


Figure 11.- Streamlines in the vicinity of recirculation.

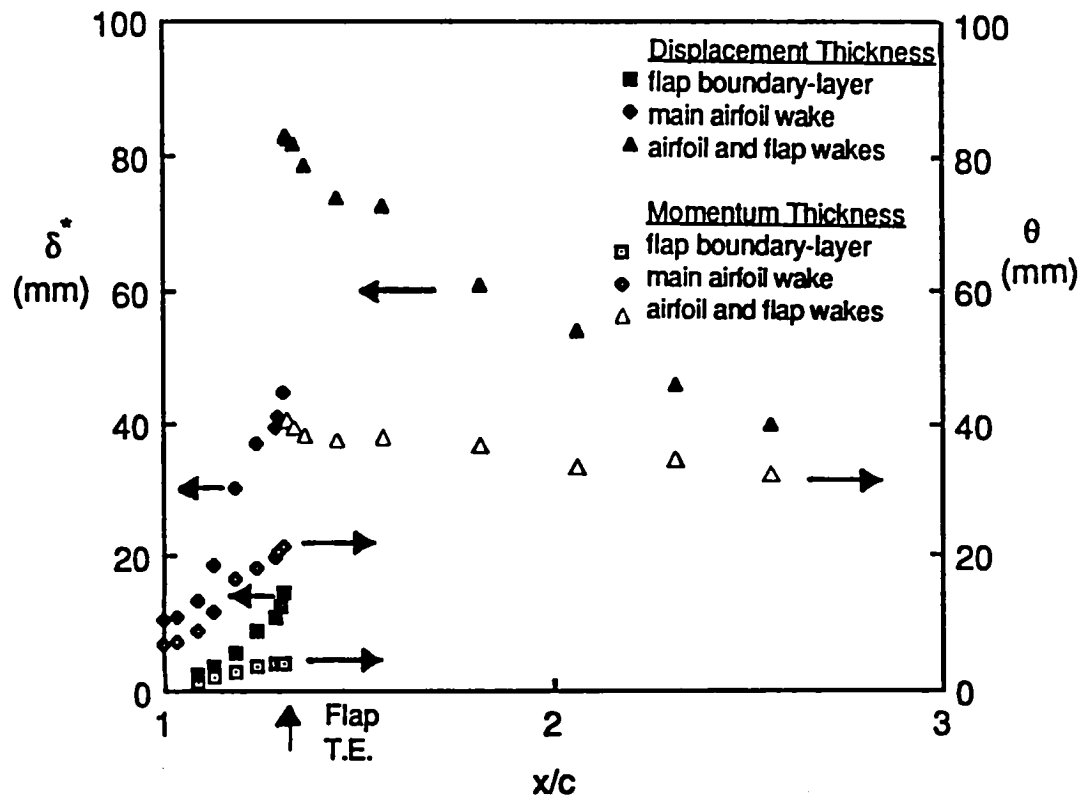


Figure 12.- Integral parameters of mean-flow development.

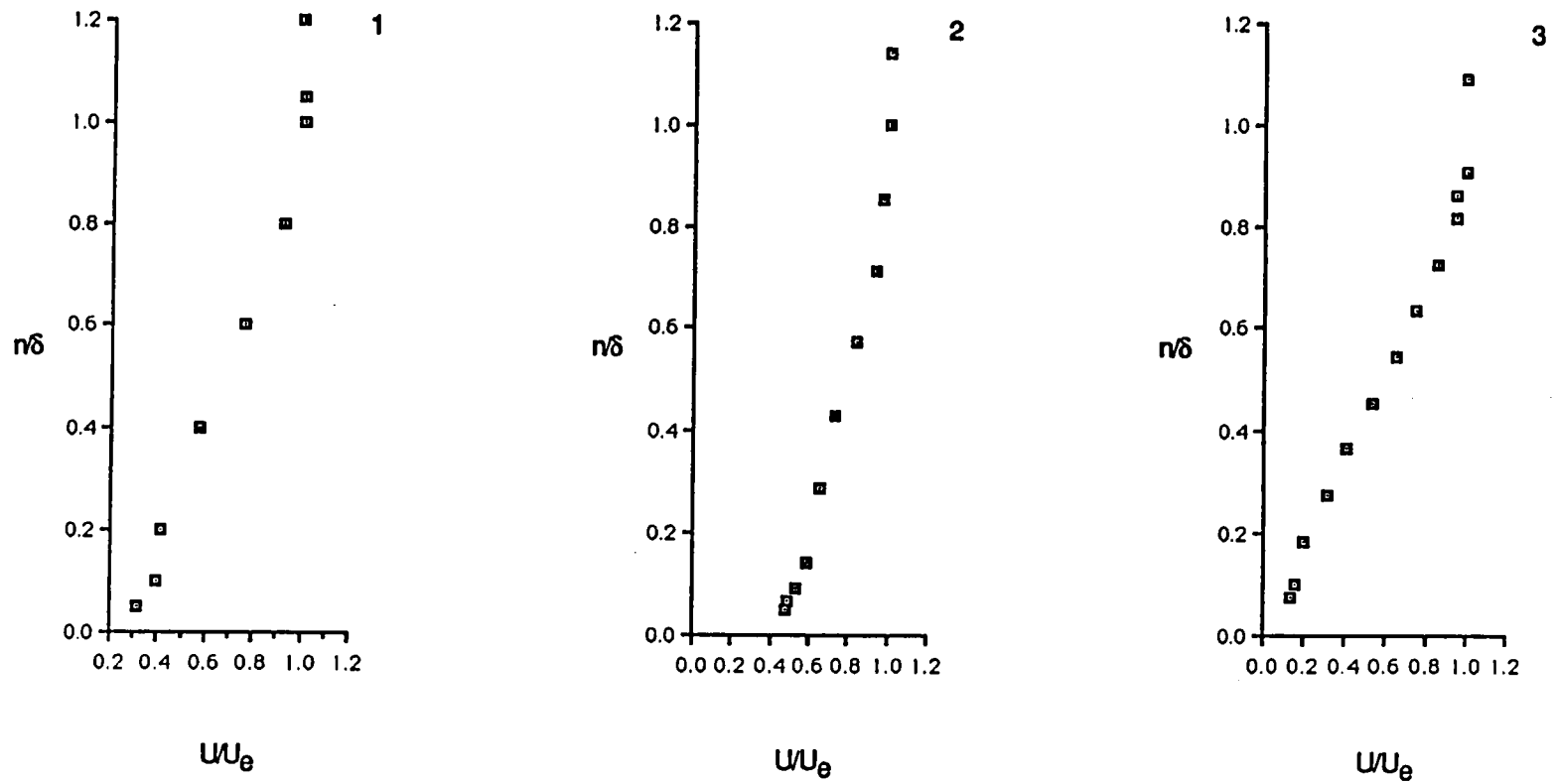


Figure 13.- Distribution of streamwise mean velocity (Station numbers refer to Table 1 and Fig. 5).

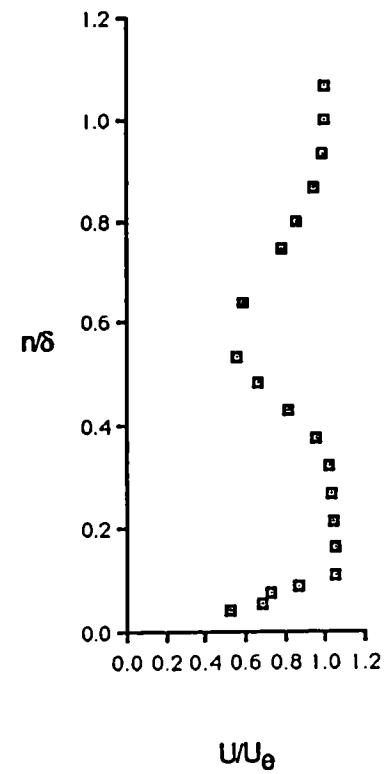
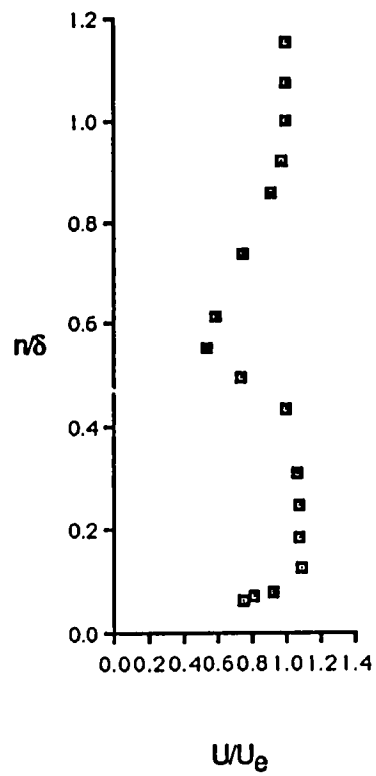
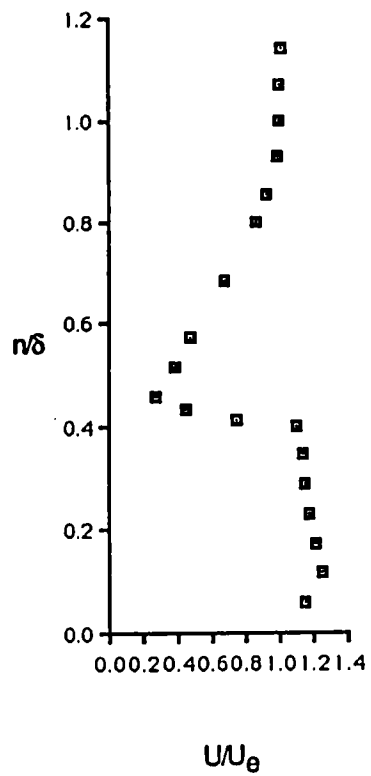


Figure 13.(cont'd)- Distribution of streamwise mean velocity (Station numbers refer to Table 1 and Fig. 5).

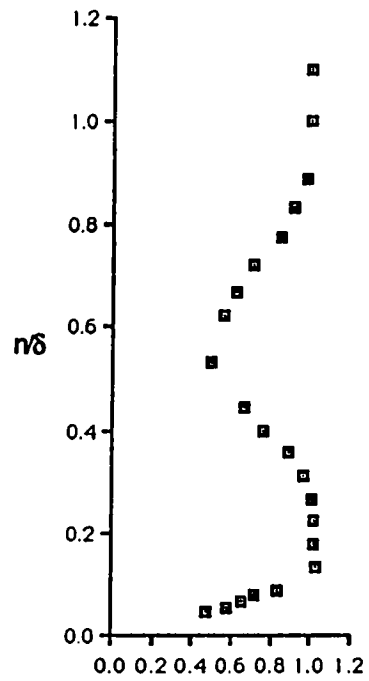
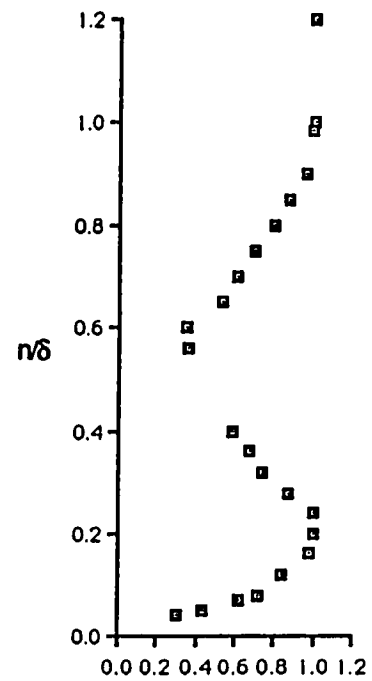
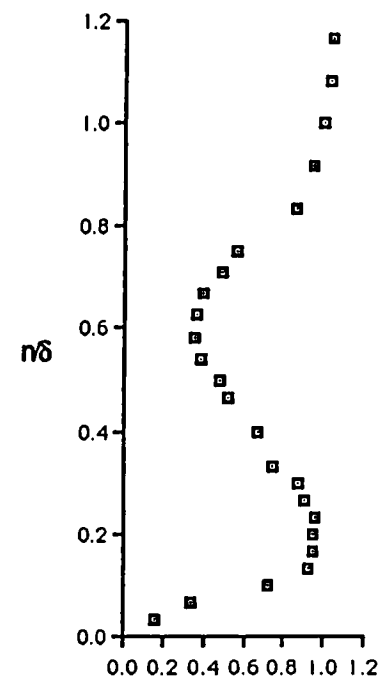
 U/U_e  U/U_e  U/U_e

Figure 13.(cont'd)- Distribution of streamwise mean velocity (Station numbers refer to Table 1 and Fig. 5).

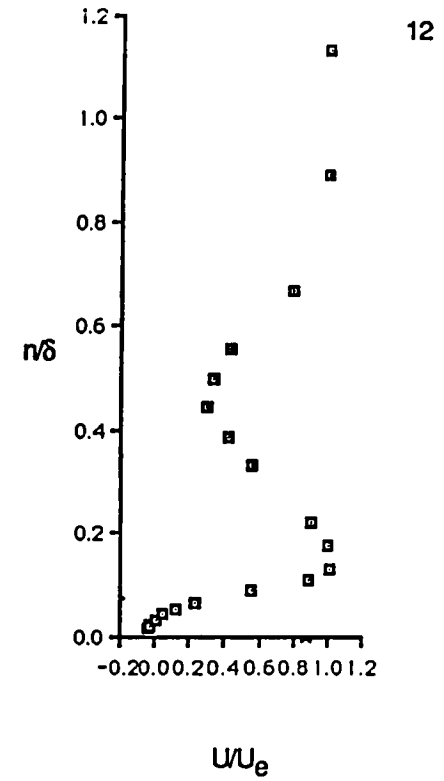
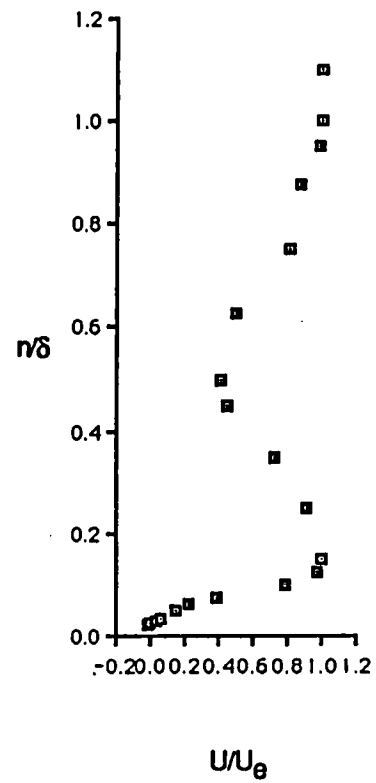
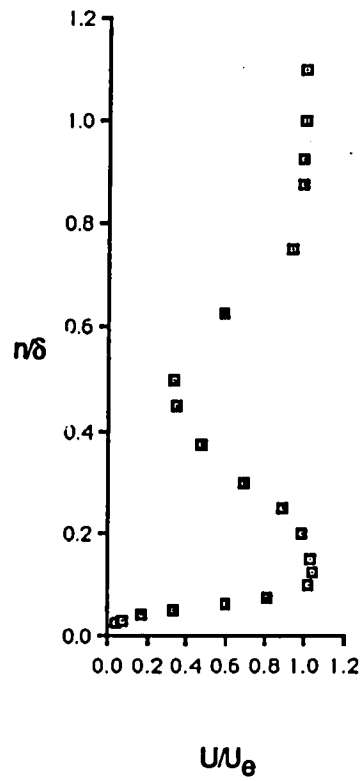


Figure 13.(cont'd)- Distribution of streamwise mean velocity (Station numbers refer to Table 1 and Fig. 5).

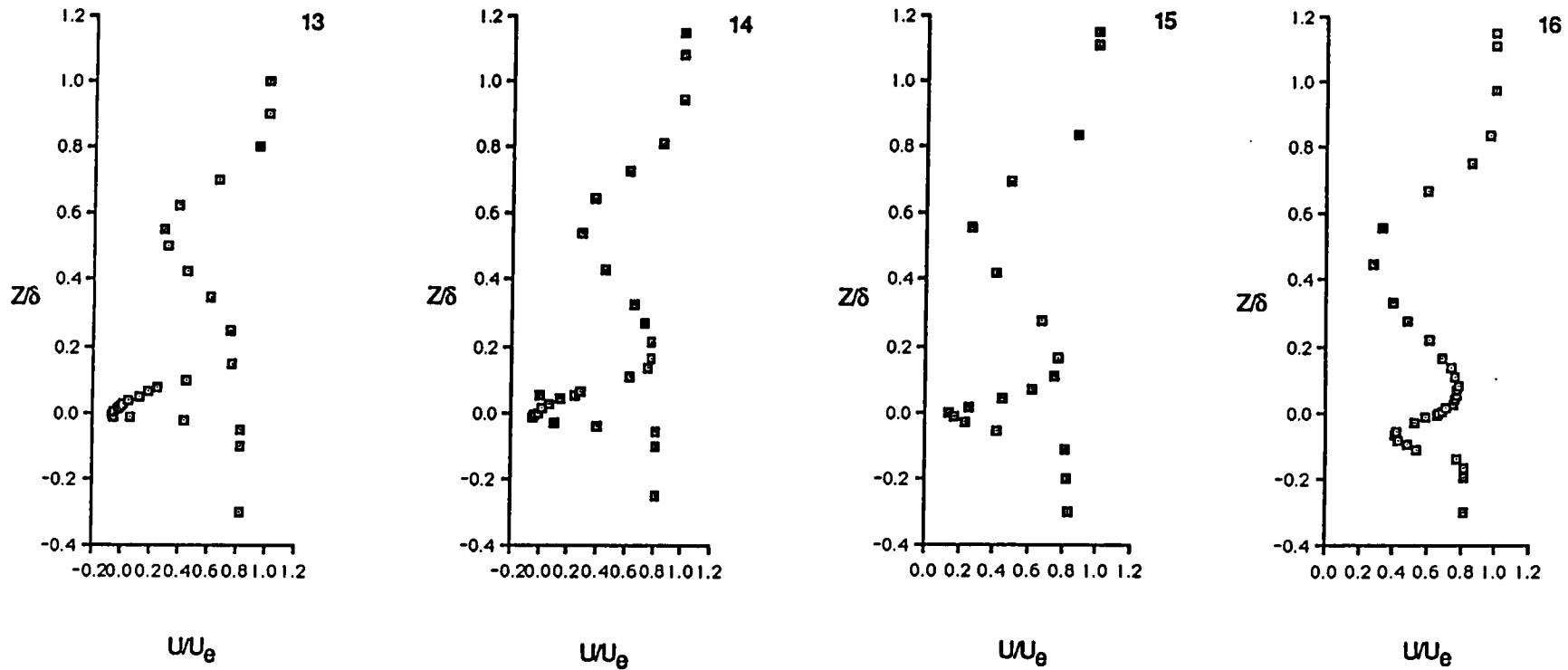


Figure 13.(cont'd)- Distribution of streamwise mean velocity (Station numbers refer to Table 1 and Fig. 5).

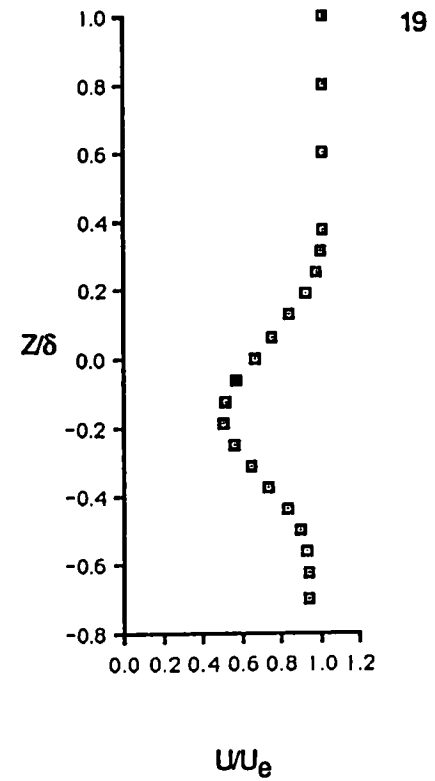
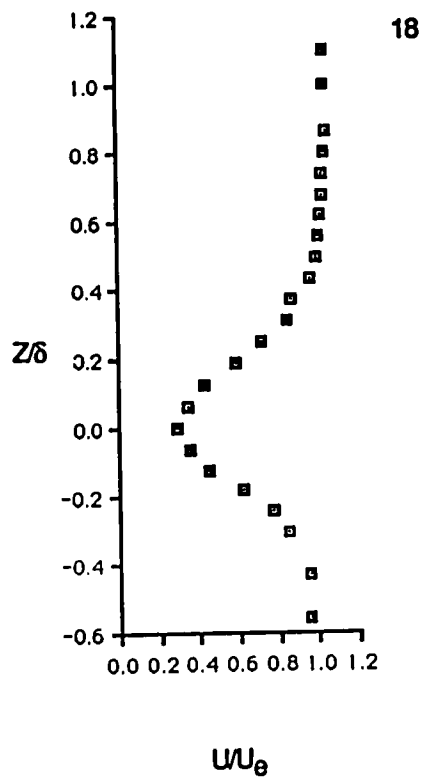
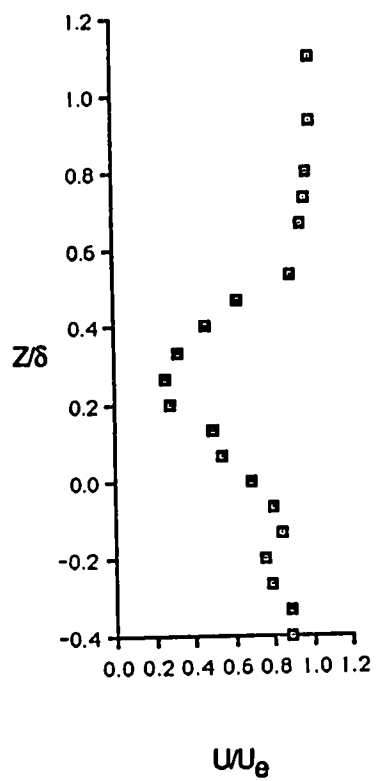


Figure 13.(cont'd)- Distribution of streamwise mean velocity (Station numbers refer to Table 1 and Fig. 5).

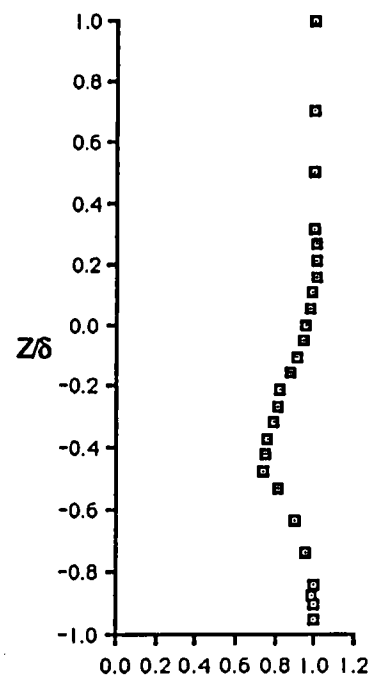
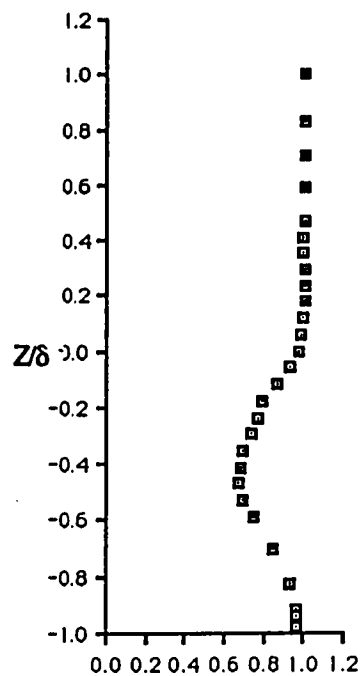
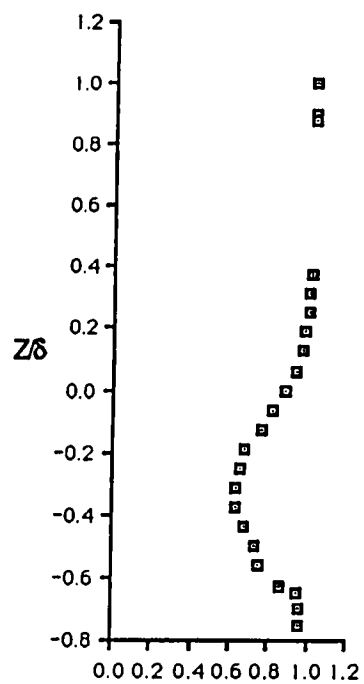


Figure 13.(concluded)- Distribution of streamwise mean velocity (Station numbers refer to Table 1 and Fig. 5).

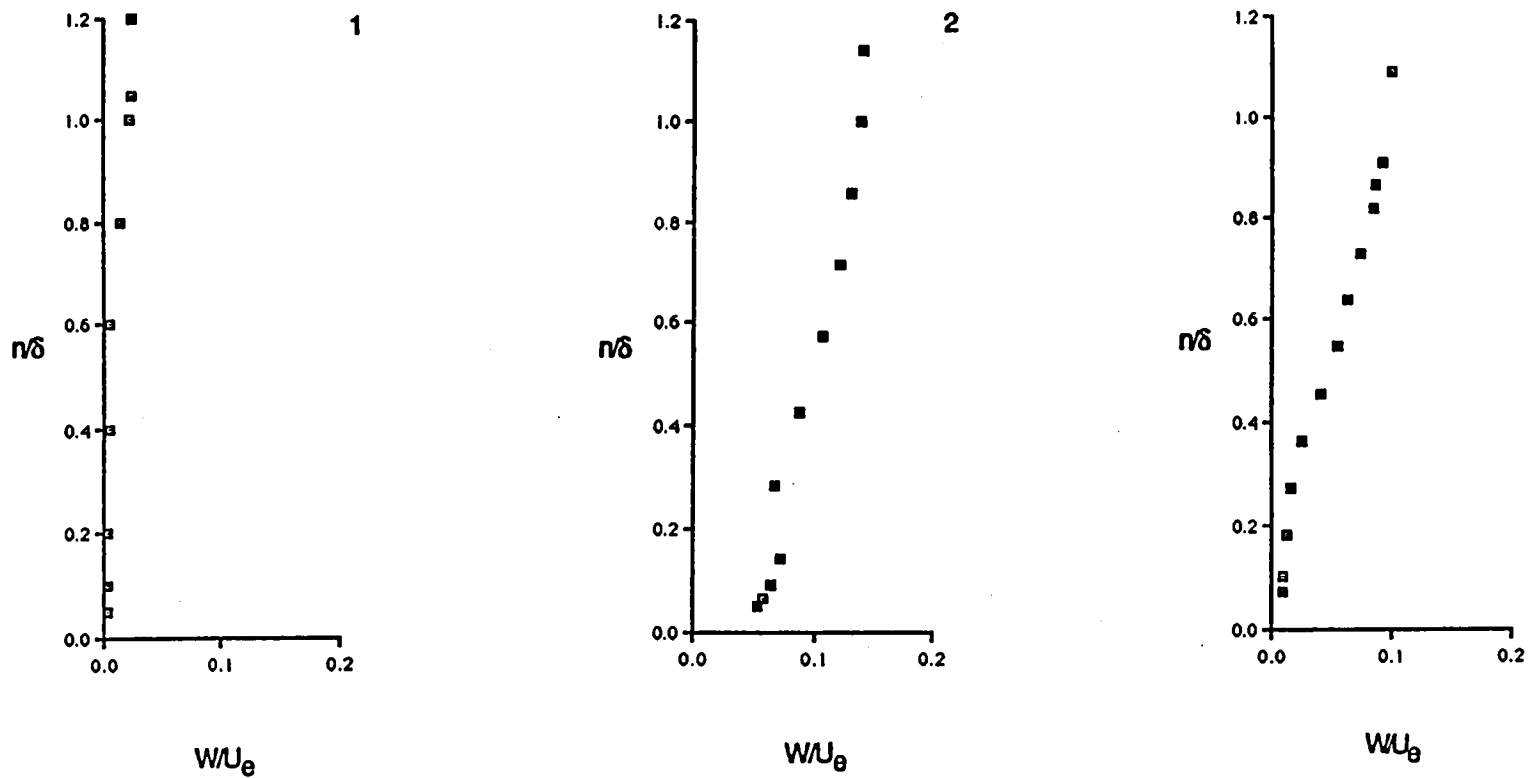


Figure 14.- Distribution of cross-flow mean velocity (Station numbers refer to Table 1 and Fig. 5).

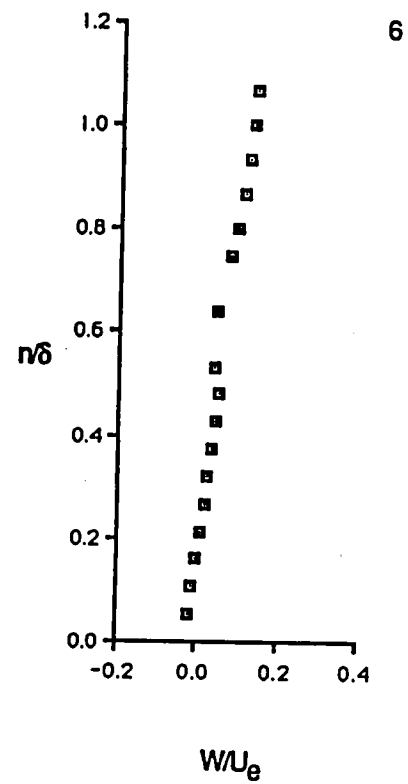
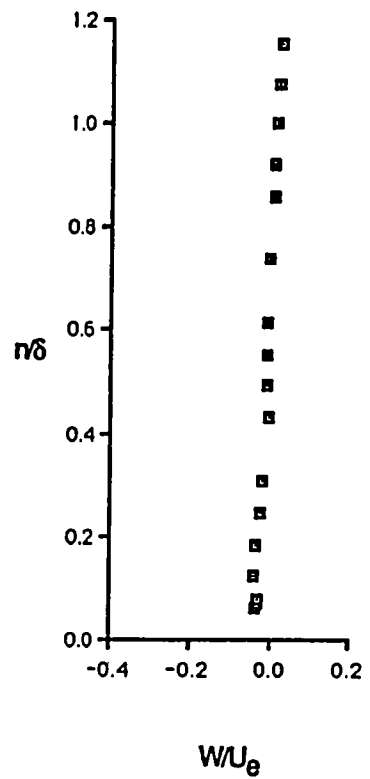
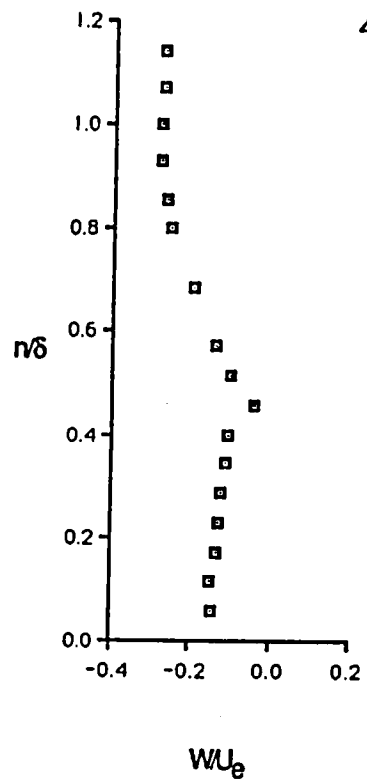


Figure 14.(cont'd)- Distribution of cross-flow mean velocity (Station numbers refer to Table 1 and Fig. 5).

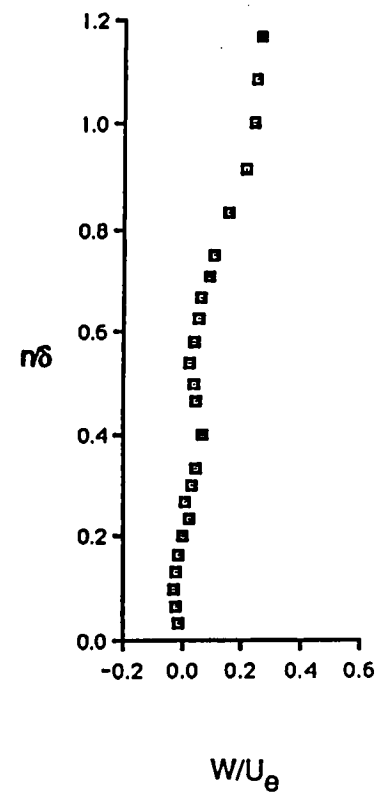
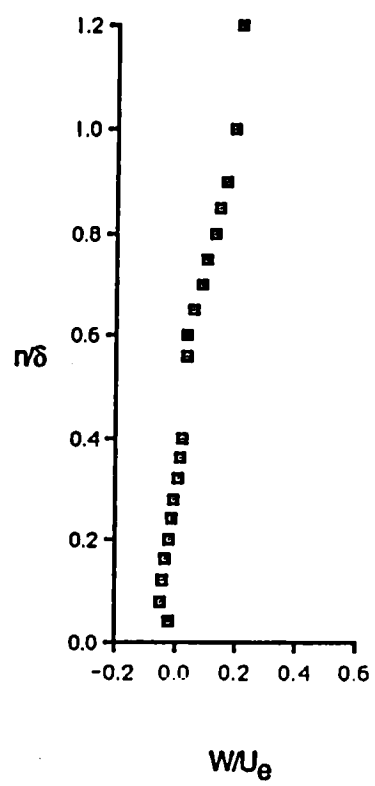
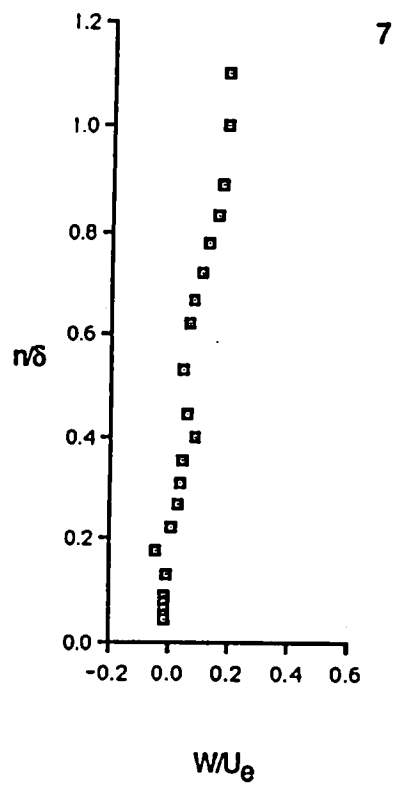


Figure 14.(cont'd)- Distribution of cross-flow mean velocity (Station numbers refer to Table 1 and Fig. 5).

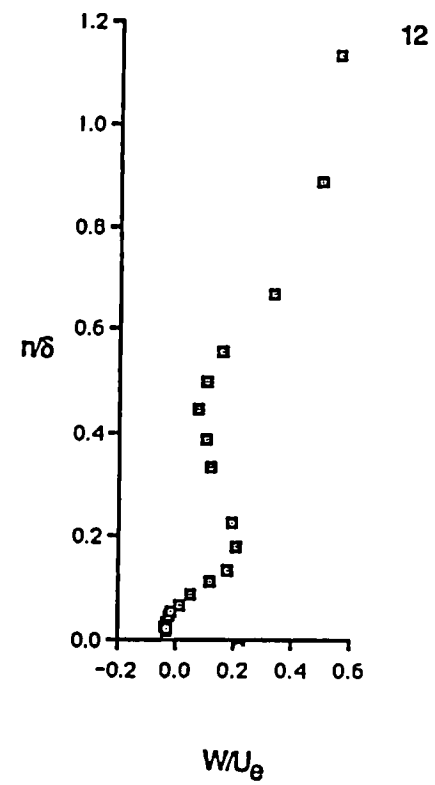
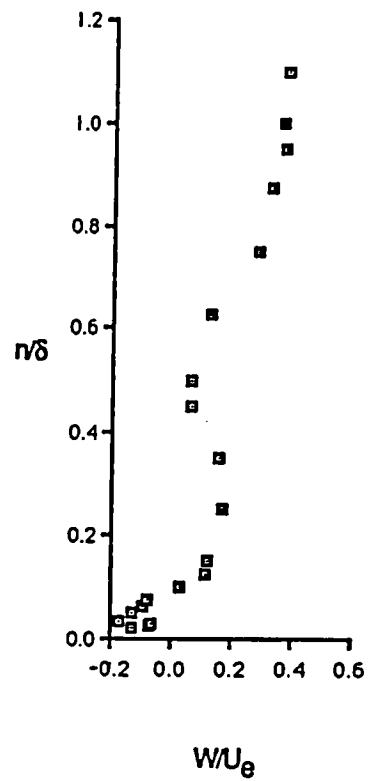
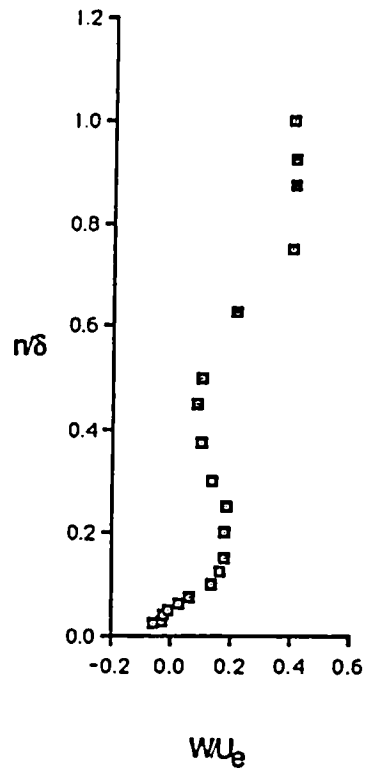


Figure 14.(cont'd)- Distribution of cross-flow mean velocity (Station numbers refer to Table 1 and Fig. 5).

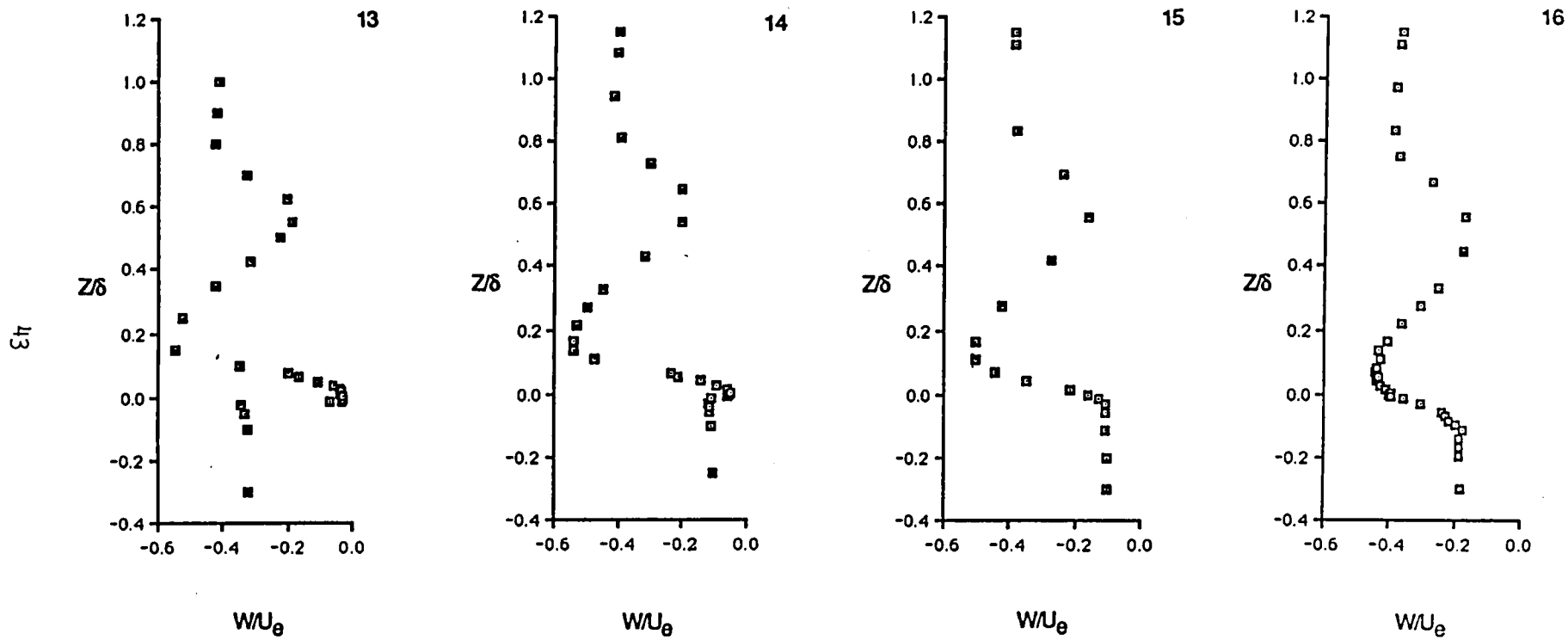


Figure 14.(cont'd)- Distribution of cross-flow mean velocity (Station numbers refer to Table 1 and Fig. 5).

\bar{w}/U_e

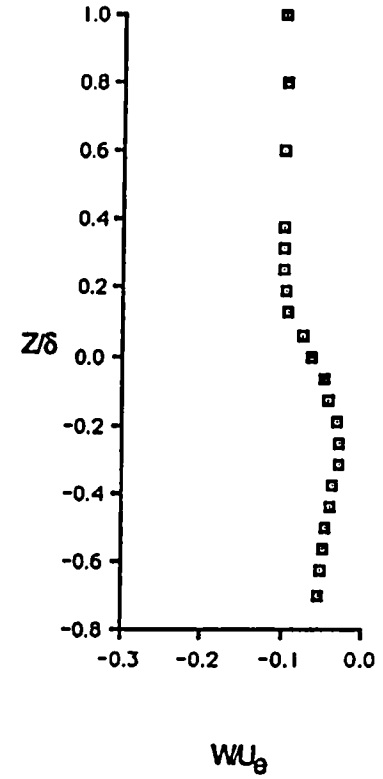
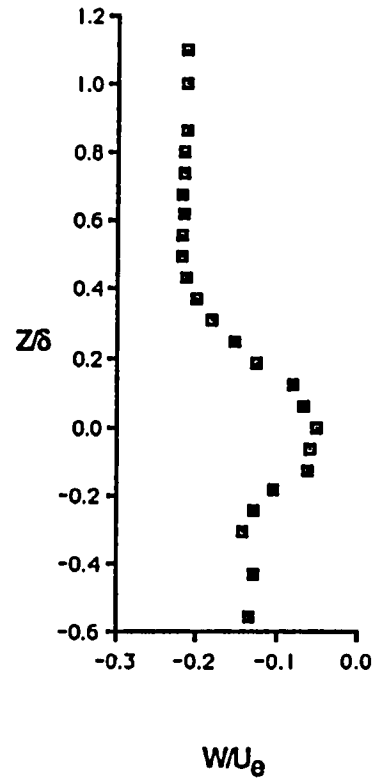
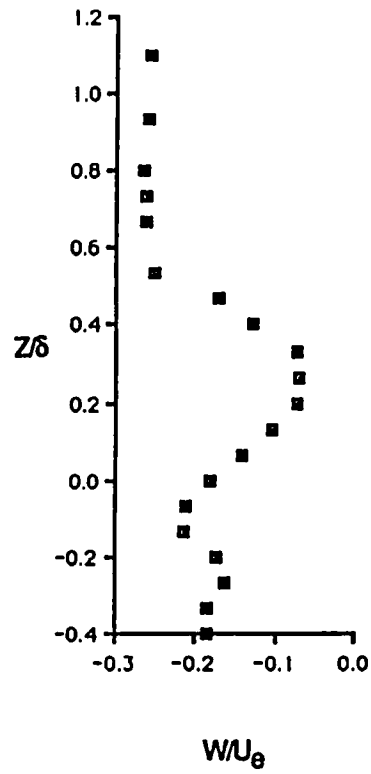
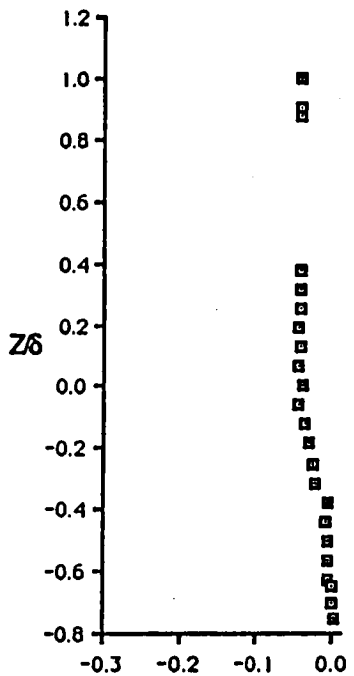
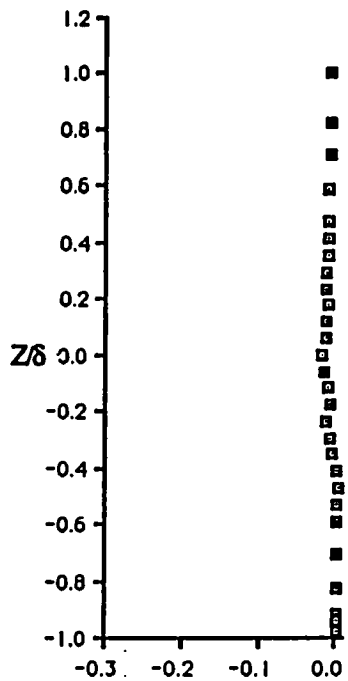


Figure 14.(cont'd)- Distribution of cross-flow mean velocity (Station numbers refer to Table 1 and Fig. 5).

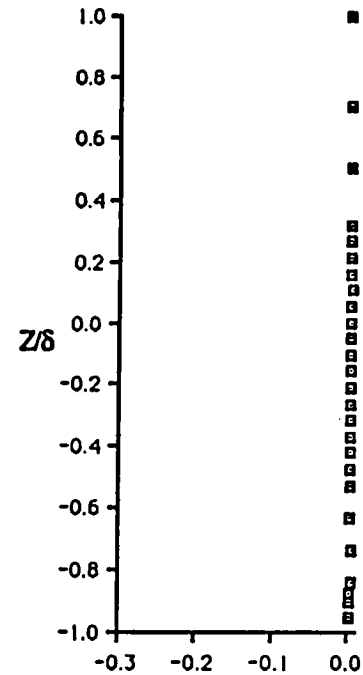
54r



W/U_θ



W/U_θ



W/U_θ

Figure 14.(concluded)- Distribution of cross-flow mean velocity (Station numbers refer to Table 1 and Fig. 5).

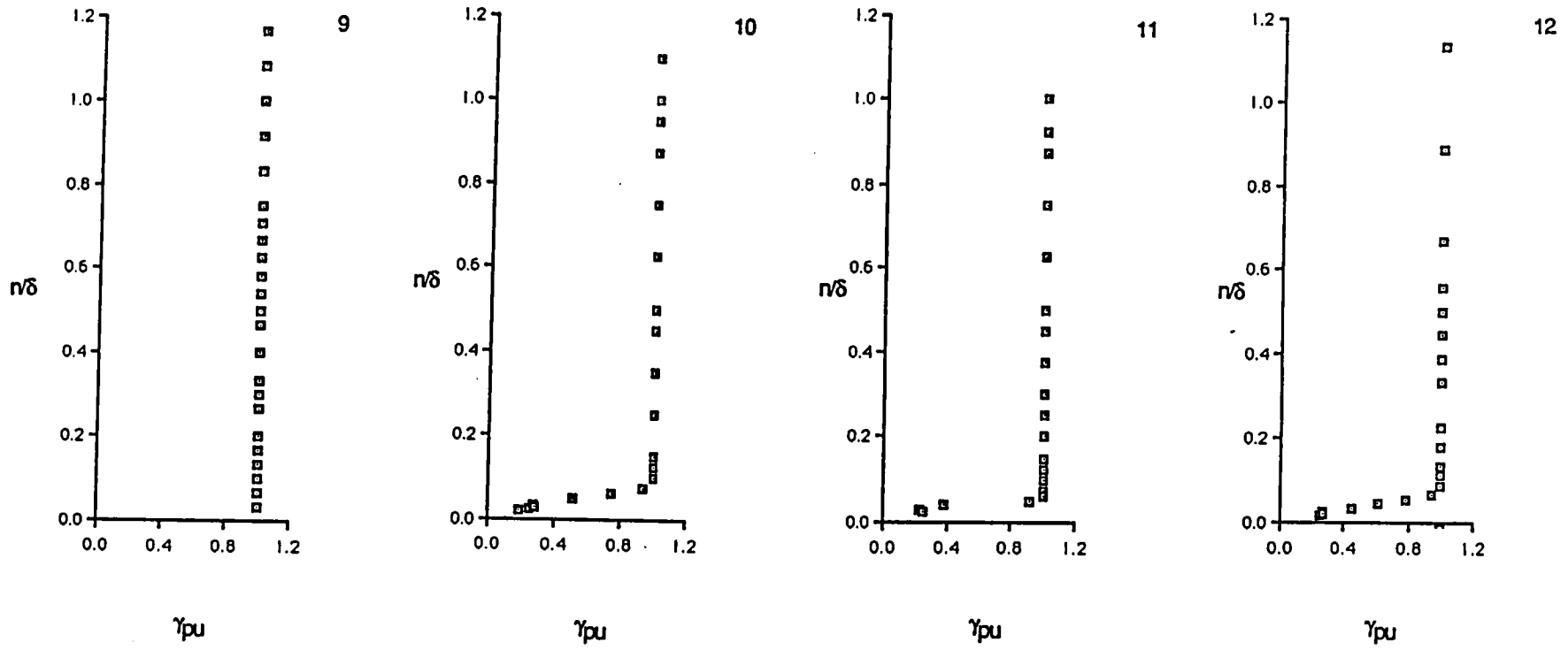


Figure 15.- Probability of positive velocity (Station numbers refer to Table 1 and Fig. 5).

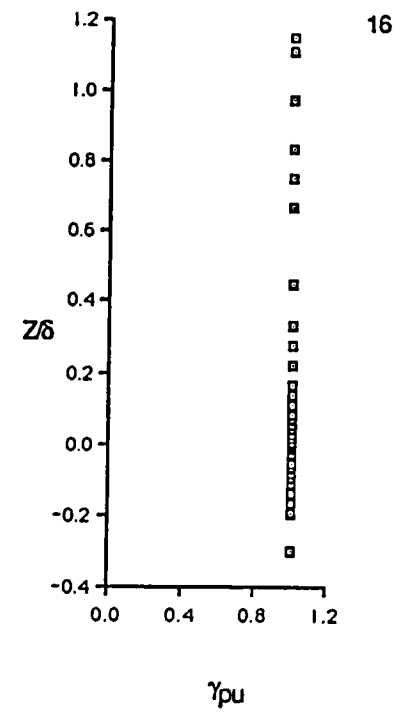
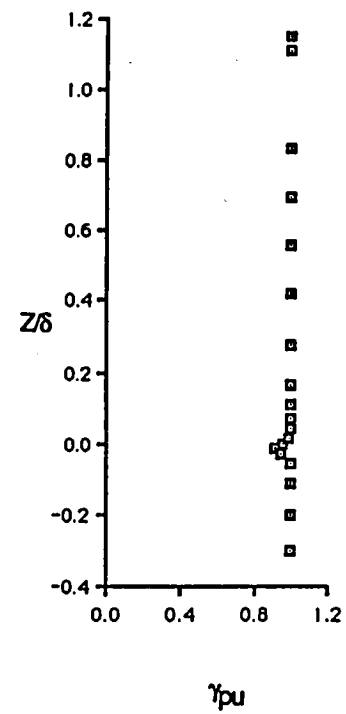
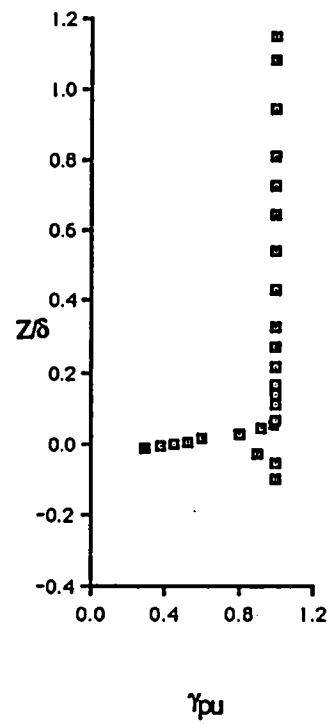
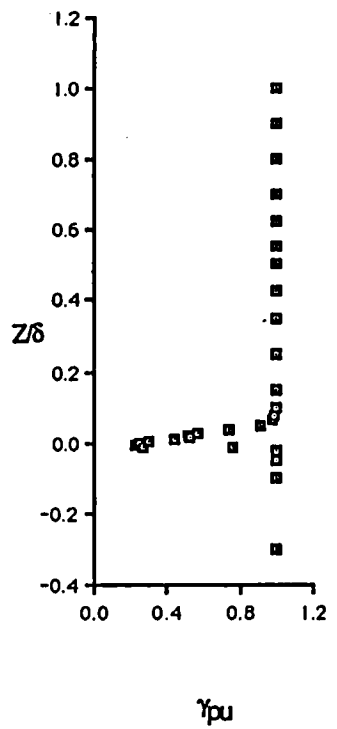


Figure 15.(concluded)- Probability of positive velocity (Station numbers refer to Table 1 and Fig. 5).

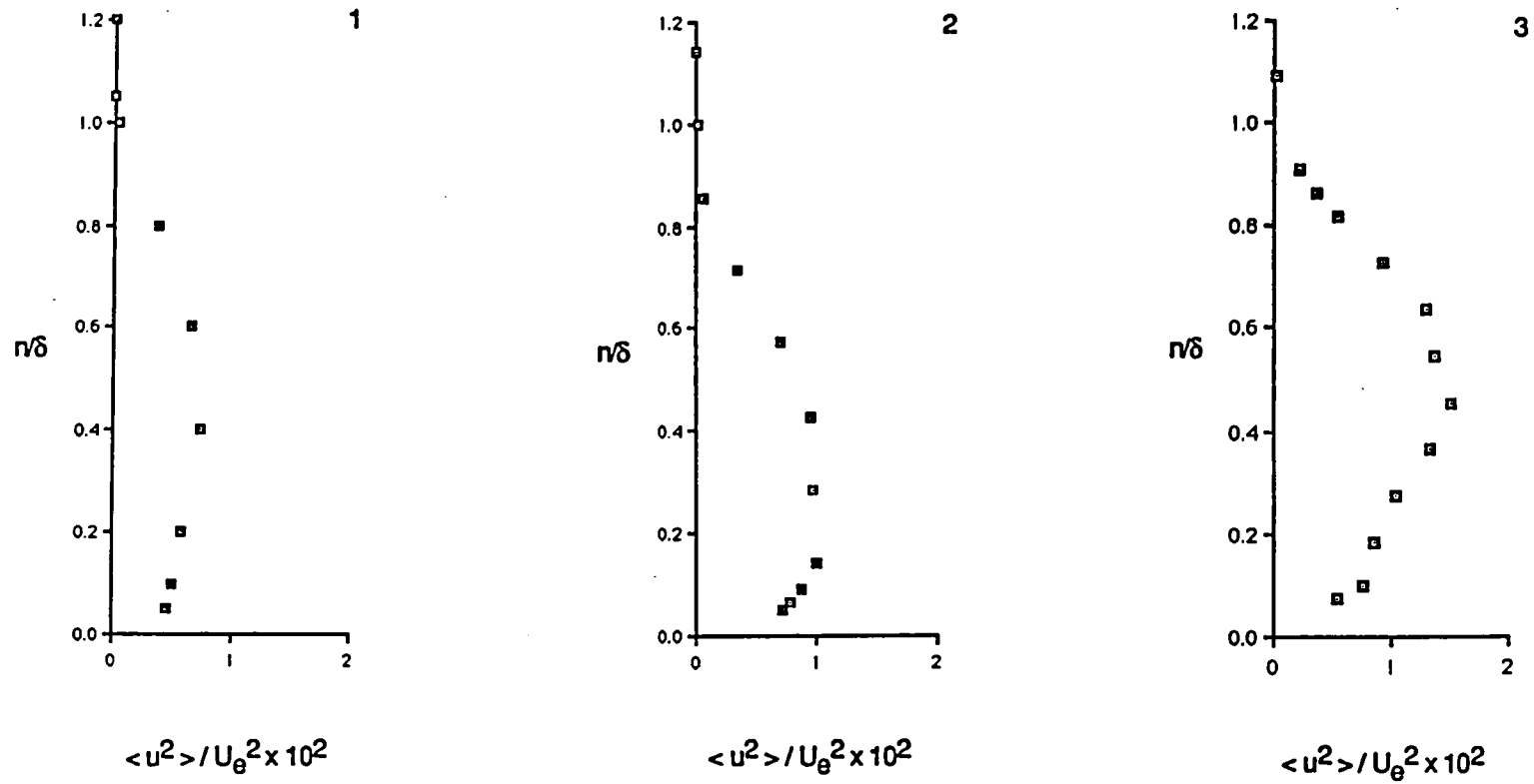


Figure 16.- Distribution of Reynolds normal stresses (Station numbers refer to Table 1 and Fig. 5).

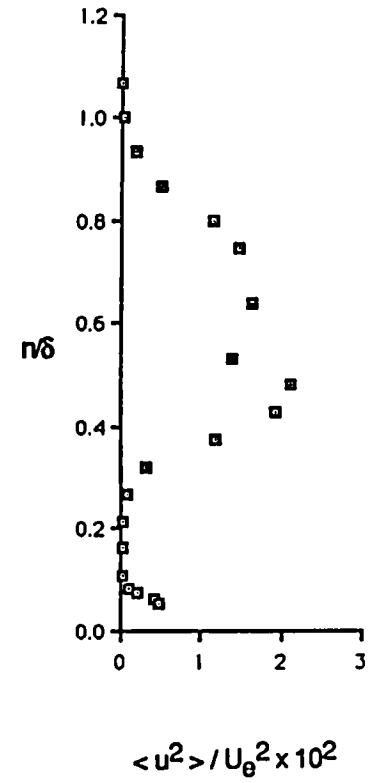
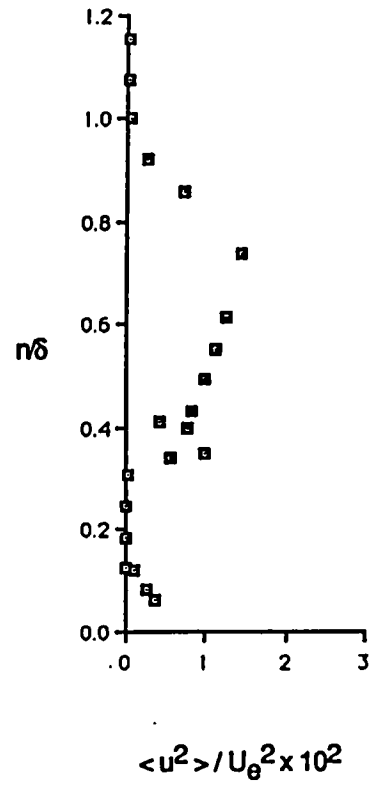
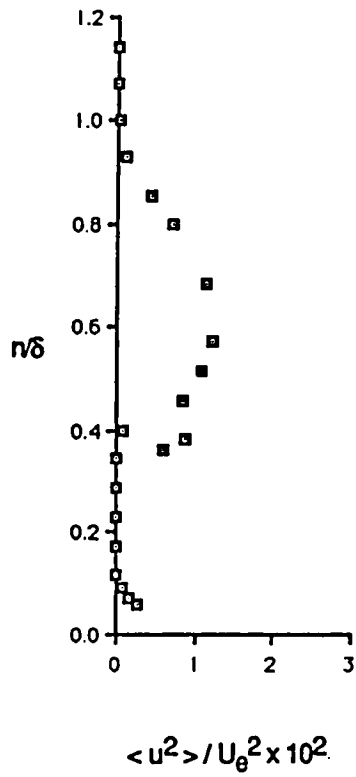


Figure 16.(cont'd)- Distribution of Reynolds normal stresses (Station numbers refer to Table 1 and Fig. 5).

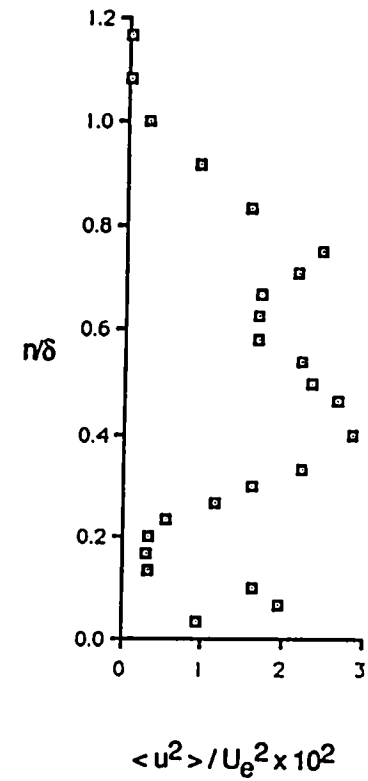
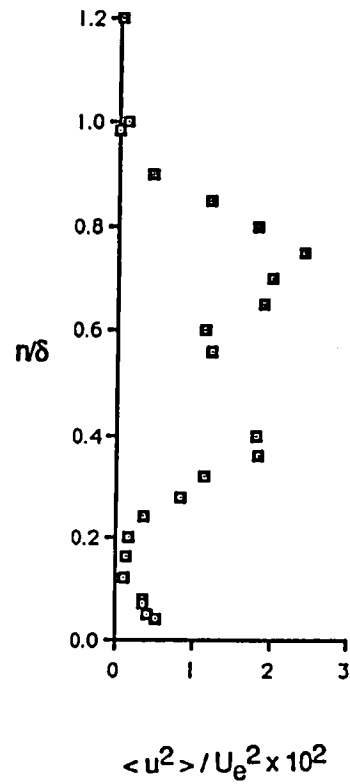
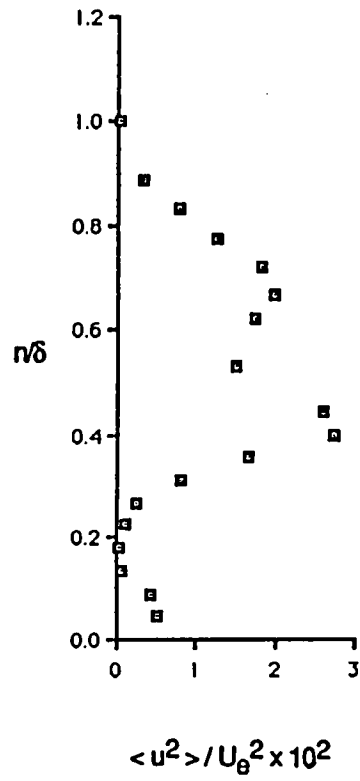


Figure 16.(cont'd)- Distribution of Reynolds normal stresses (Station numbers refer to Table 1 and Fig. 5).

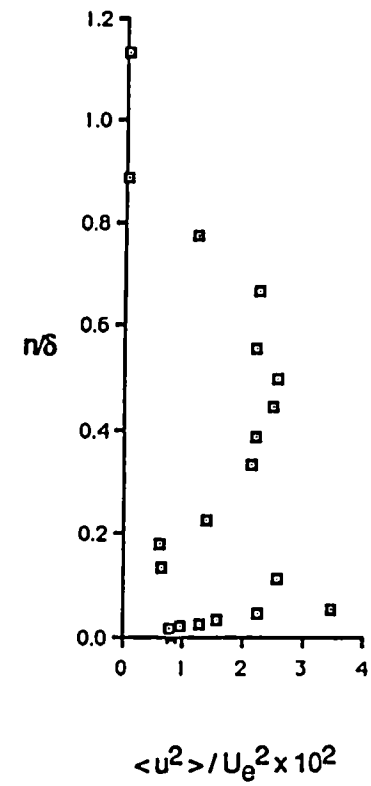
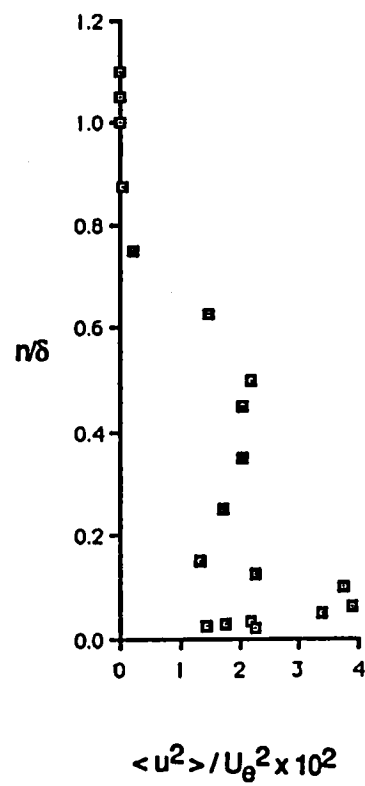
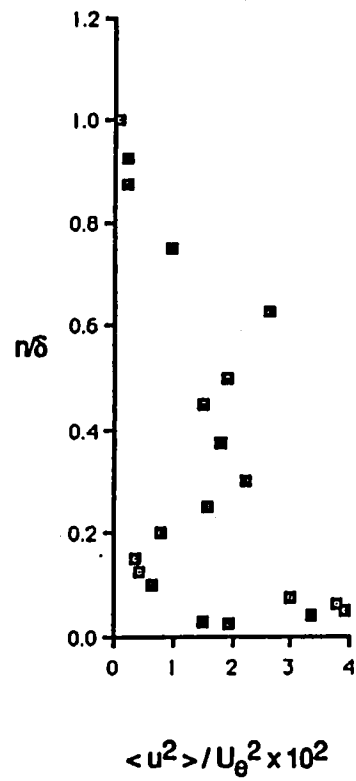


Figure 16.(cont'd)- Distribution of Reynolds normal stresses (Station numbers refer to Table 1 and Fig. 5).

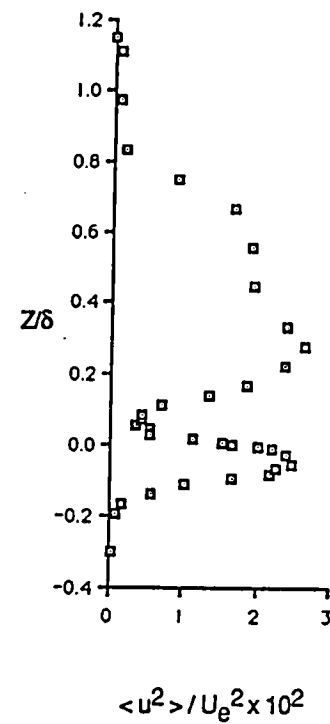
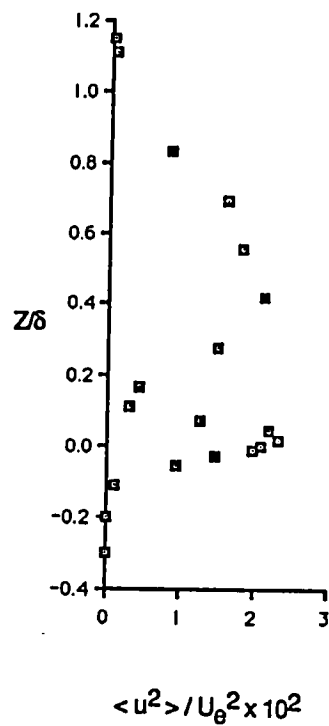
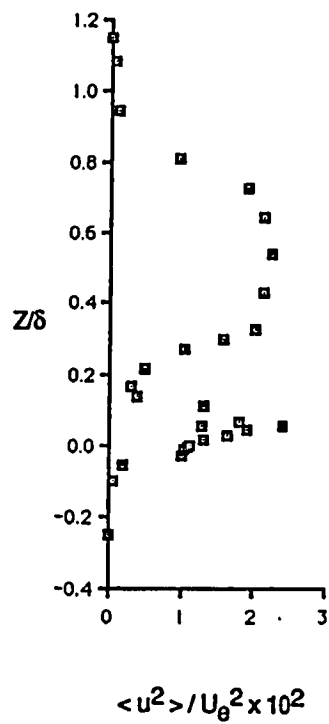
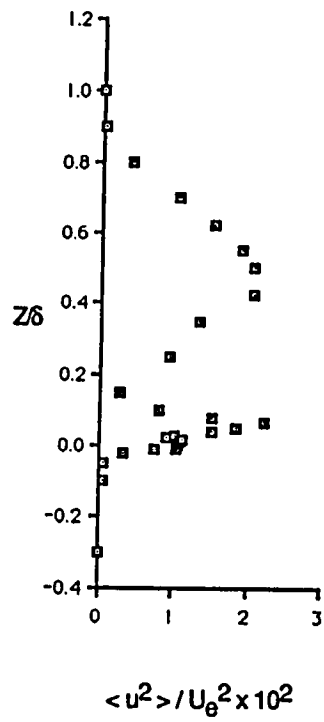


Figure 16.(cont'd)- Distribution of Reynolds normal stresses (Station numbers refer to Table 1 and Fig. 5).

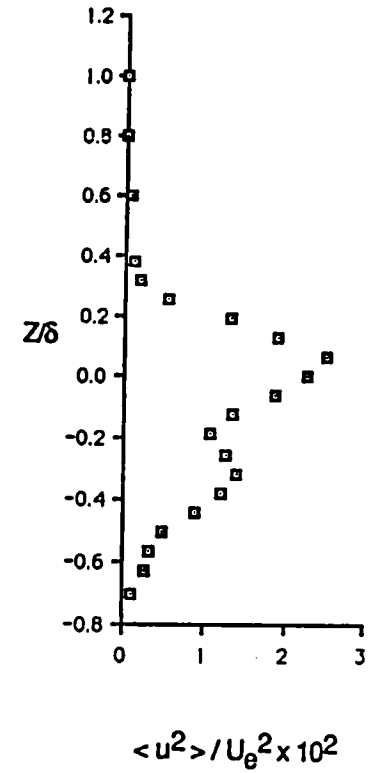
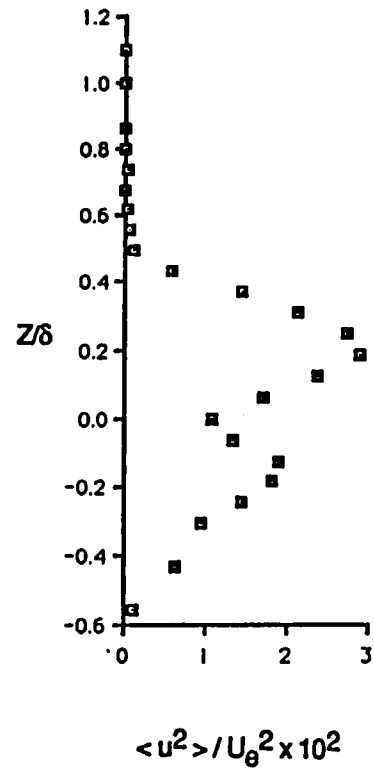
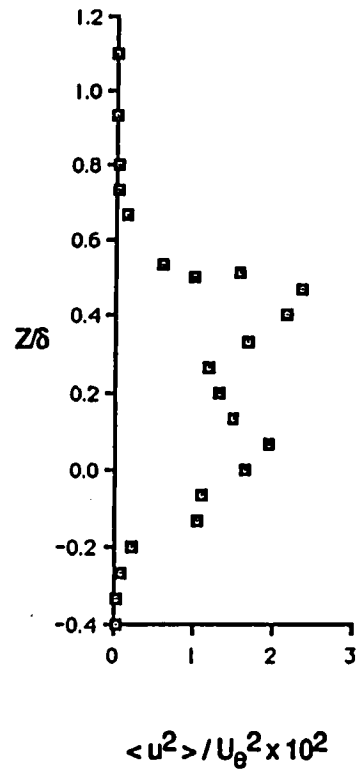


Figure 16.(cont'd)- Distribution of Reynolds normal stresses (Station numbers refer to Table 1 and Fig. 5).

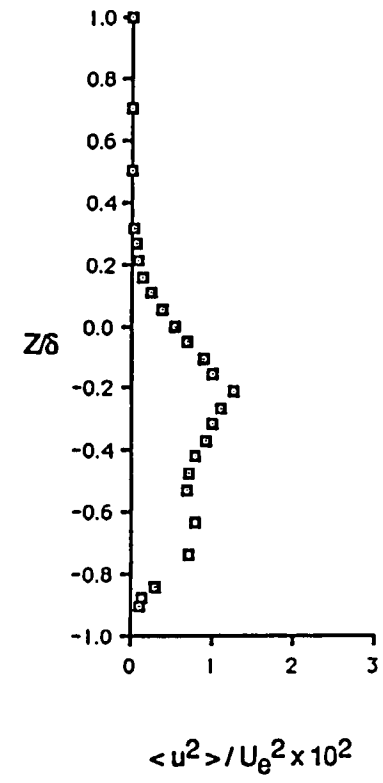
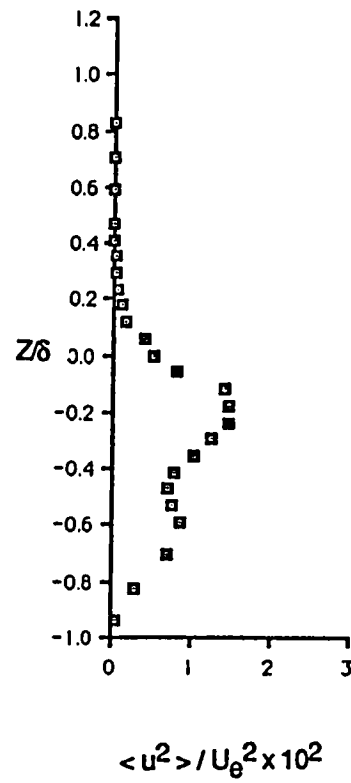
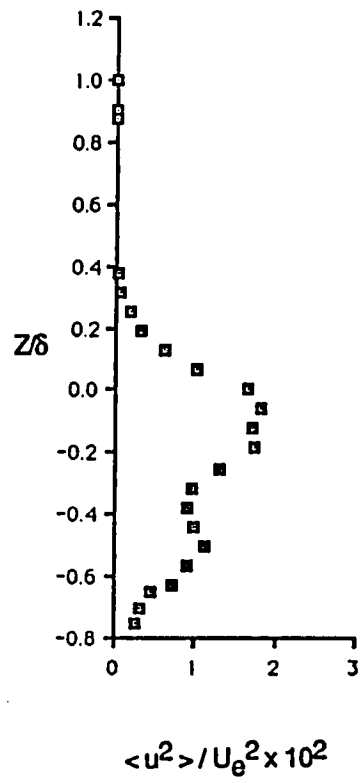


Figure 16.(concluded)- Distribution of Reynolds normal stresses (Station numbers refer to Table 1 and Fig. 5).

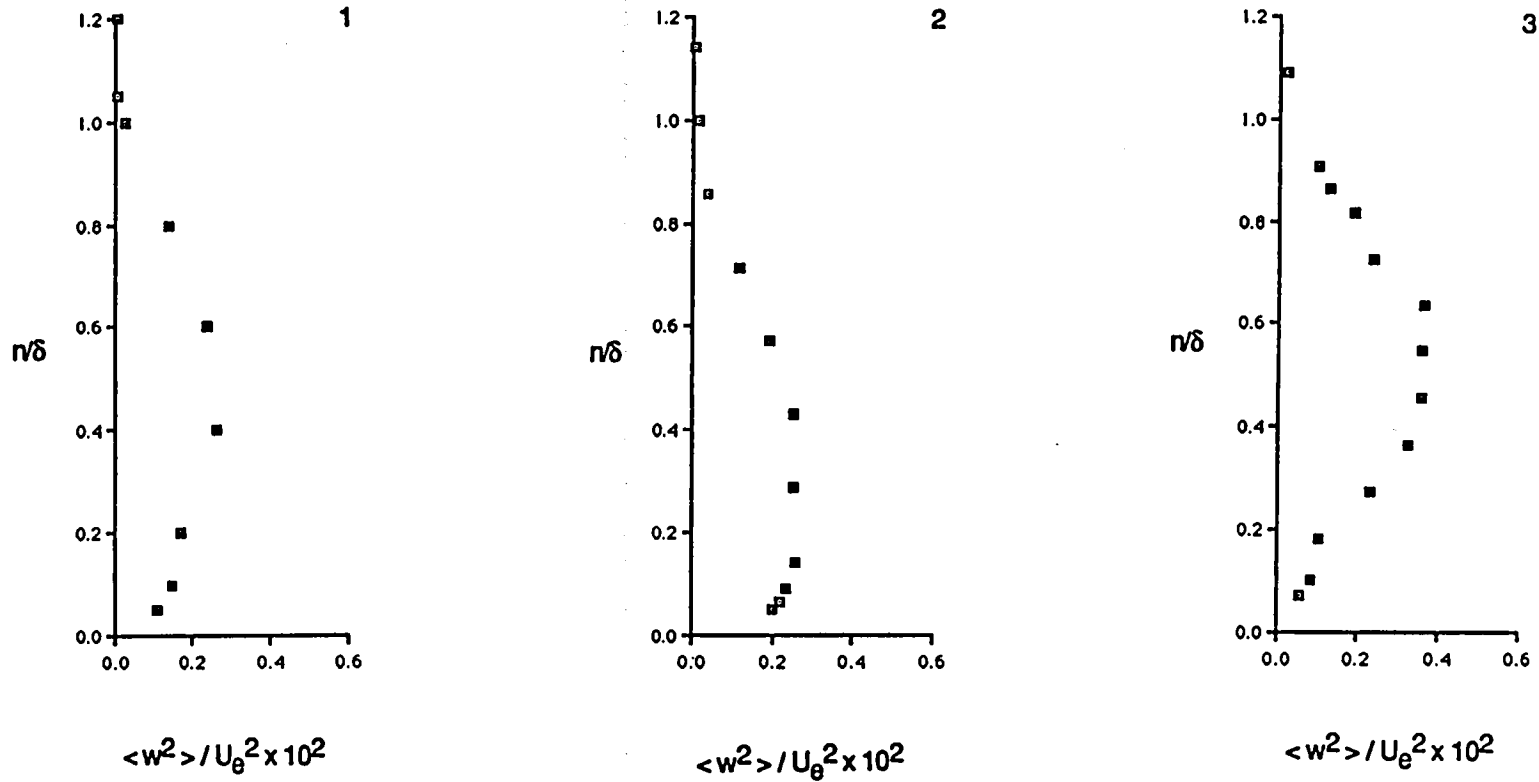


Figure 17.- Distribution of Reynolds normal stresses (Station numbers refer to Table 1 and Fig. 5).

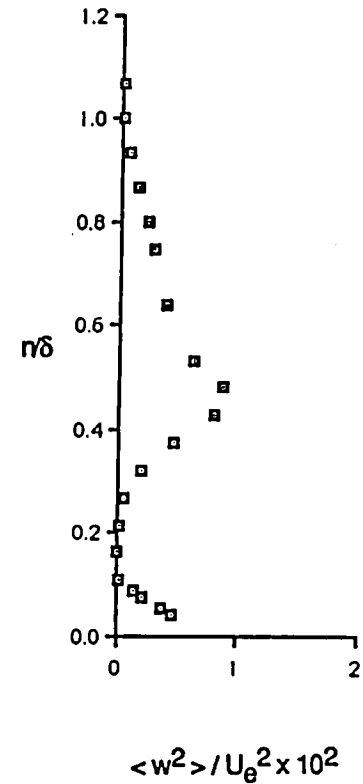
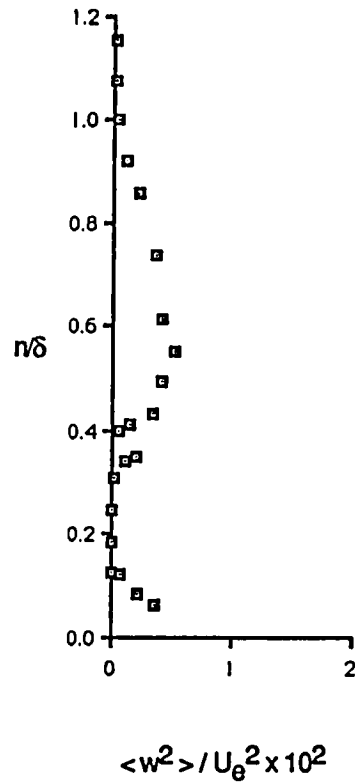
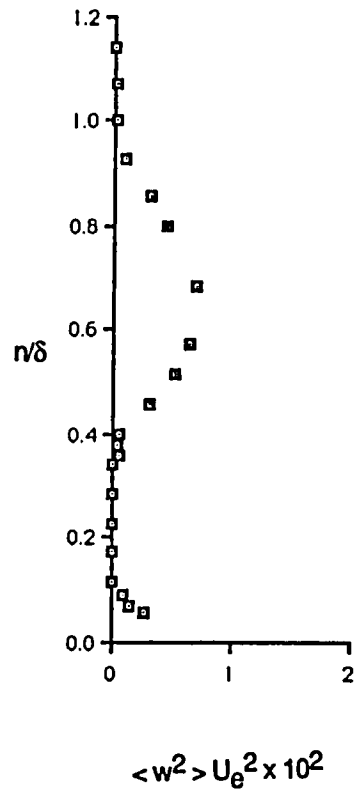


Figure 17.(cont'd) - Distribution of Reynolds normal stresses (Station numbers refer to Table 1 and Fig. 5).

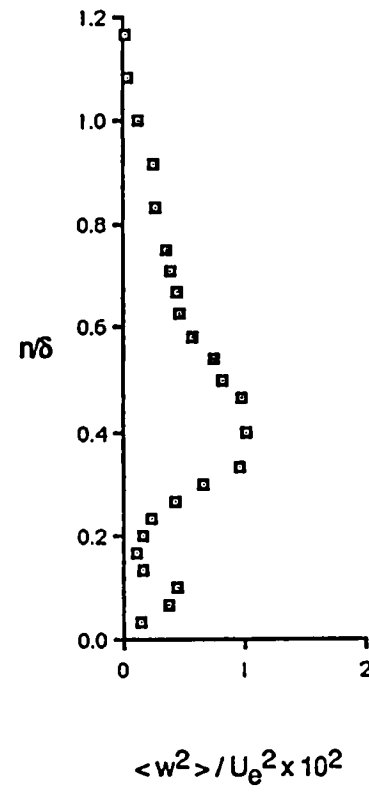
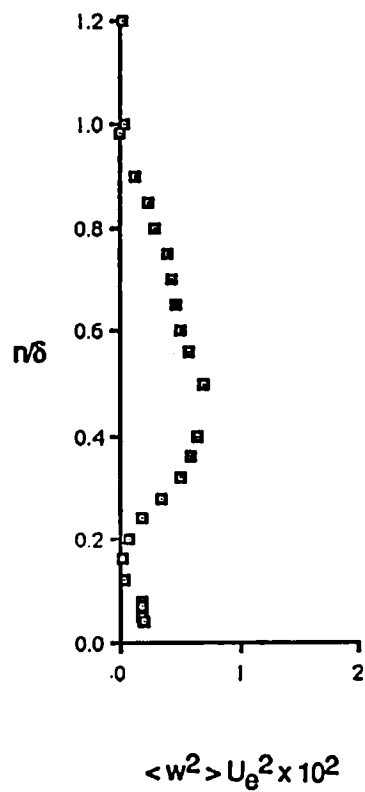
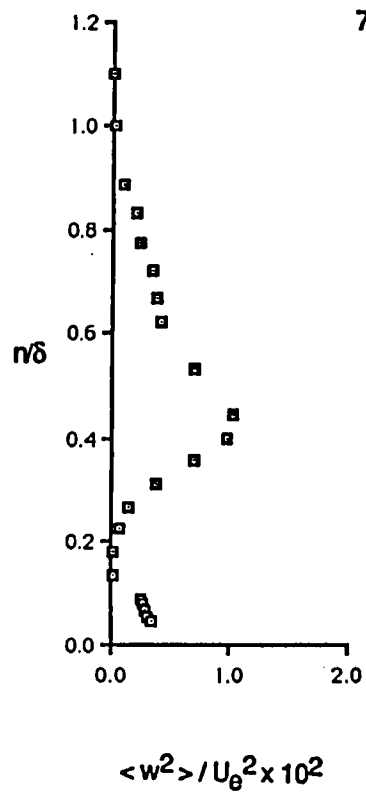


Figure 17.(cont'd) - Distribution of Reynolds normal stresses (Station numbers refer to Table 1 and Fig. 5).

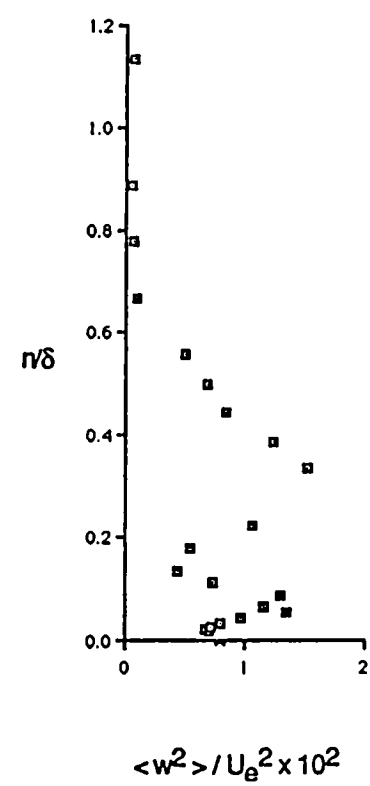
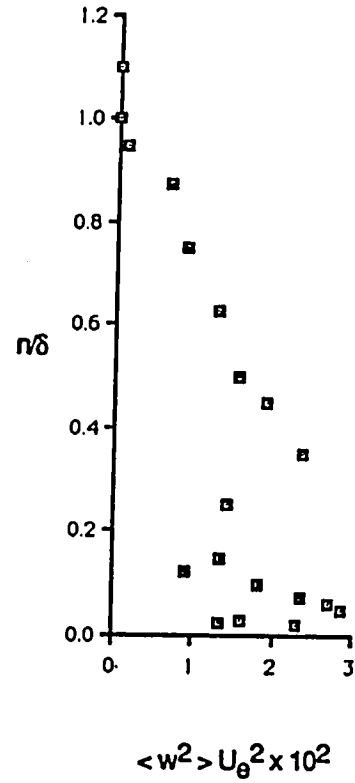
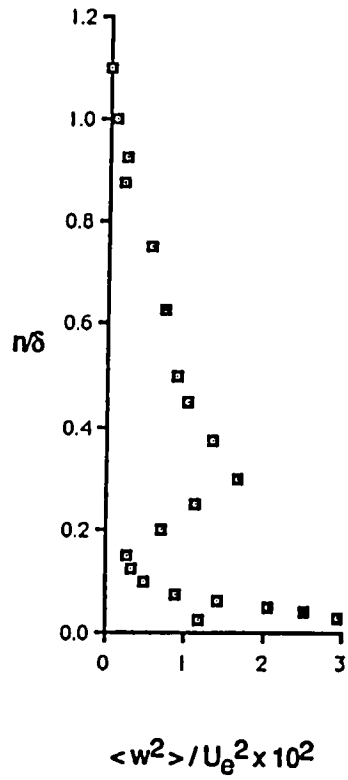


Figure 17.(cont'd) - Distribution of Reynolds normal stresses (Station numbers refer to Table 1 and Fig. 5).

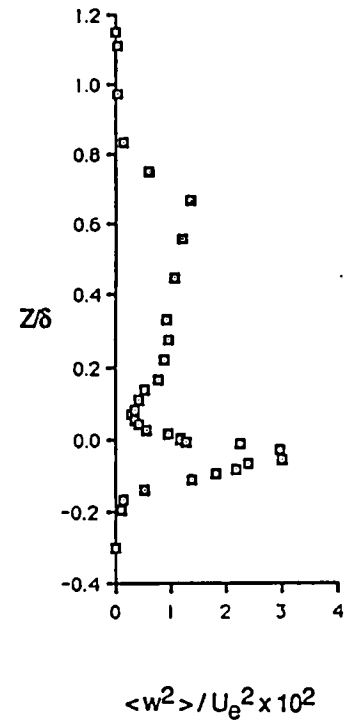
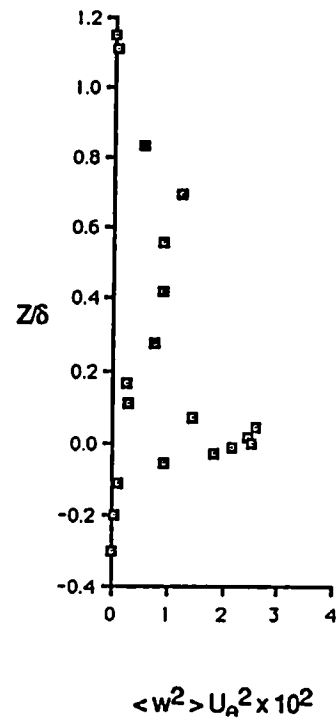
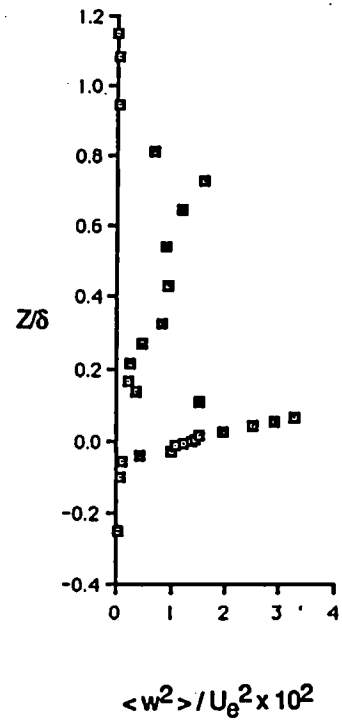
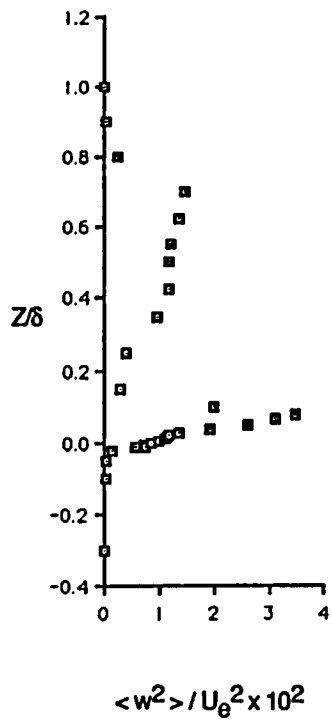


Figure 17.(cont'd) - Distribution of Reynolds normal stresses (Station numbers refer to Table 1 and Fig. 5).

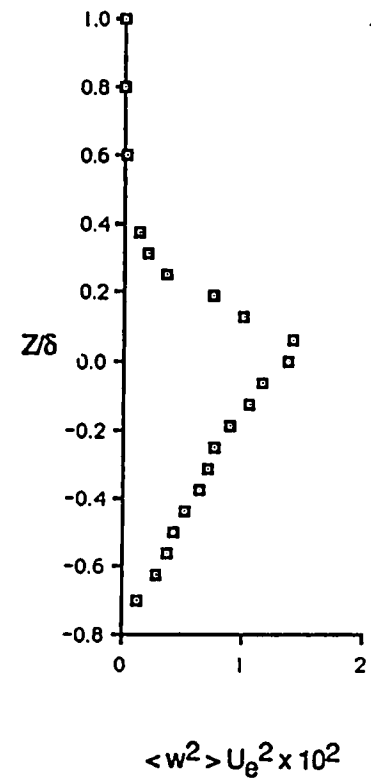
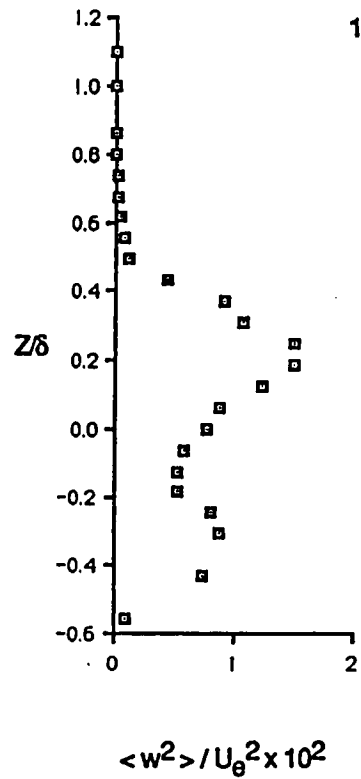
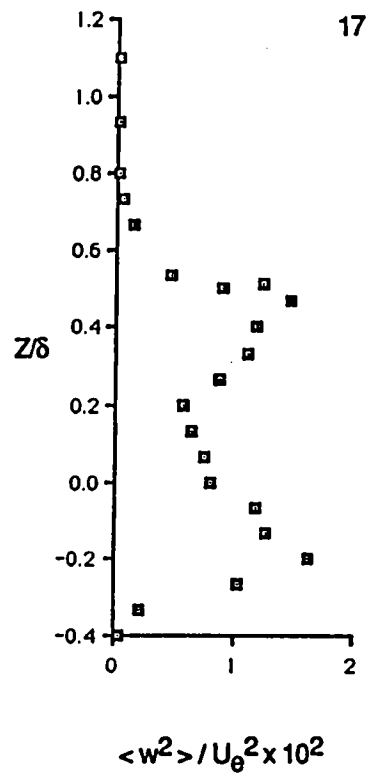


Figure 17.(cont'd) - Distribution of Reynolds normal stresses (Station numbers refer to Table 1 and Fig. 5).

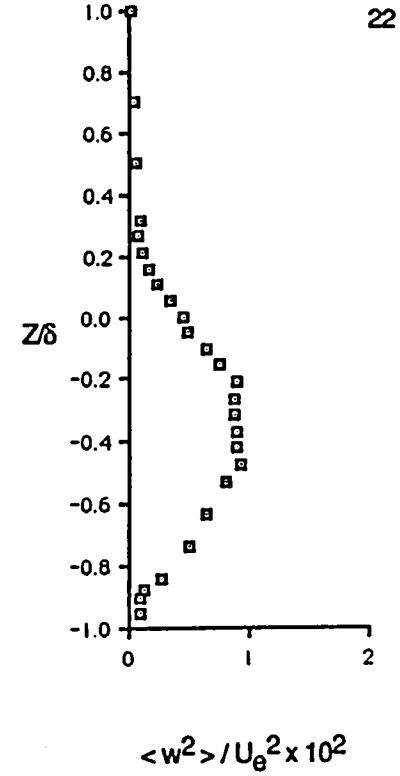
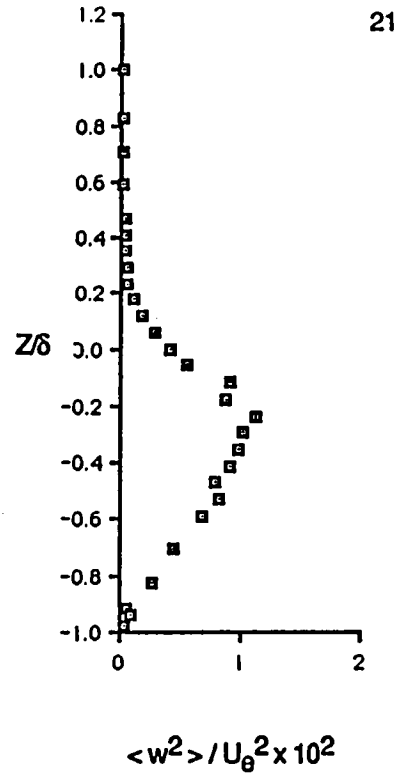
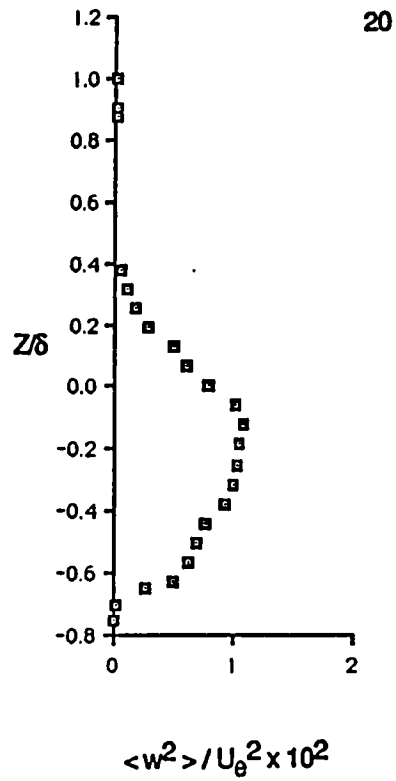


Figure 17.(concluded) - Distribution of Reynolds normal stresses (Station numbers refer to Table 1 and Fig. 5).

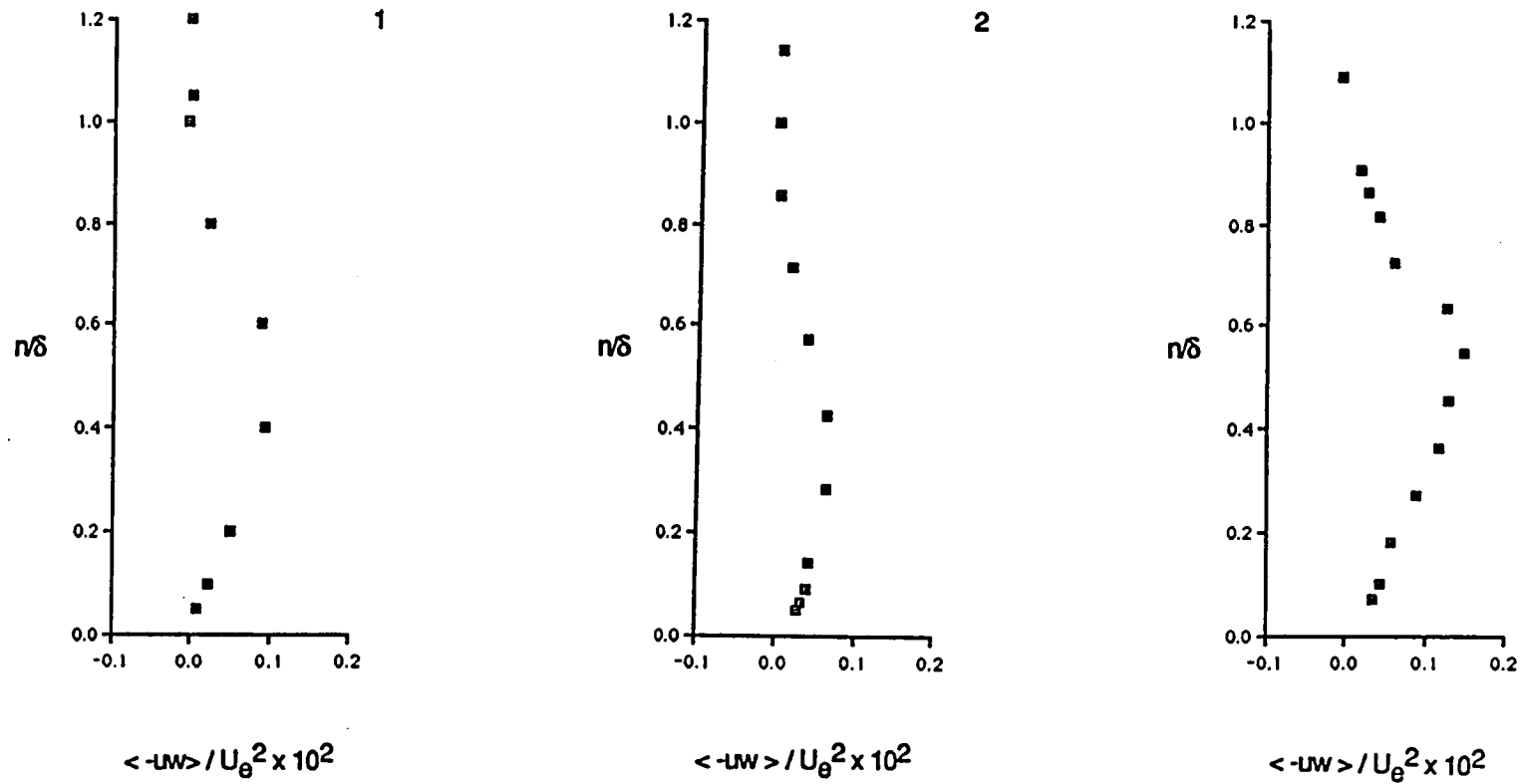


Figure 18.- Distribution of Reynolds shear stresses (Station numbers refer to Table 1 and Fig. 5).

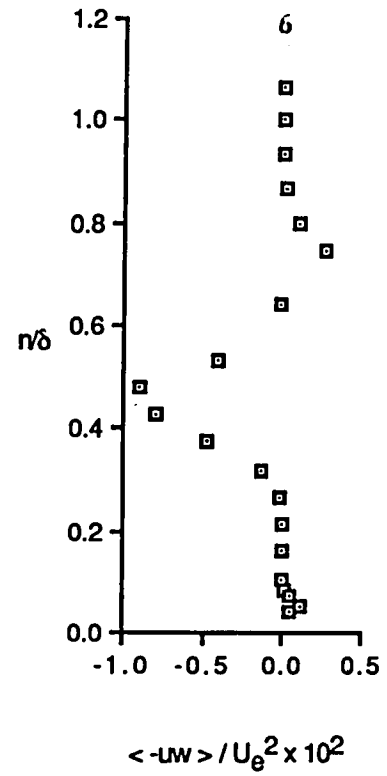
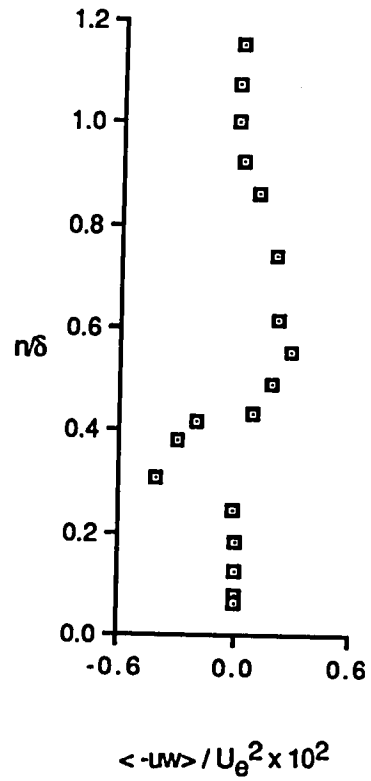
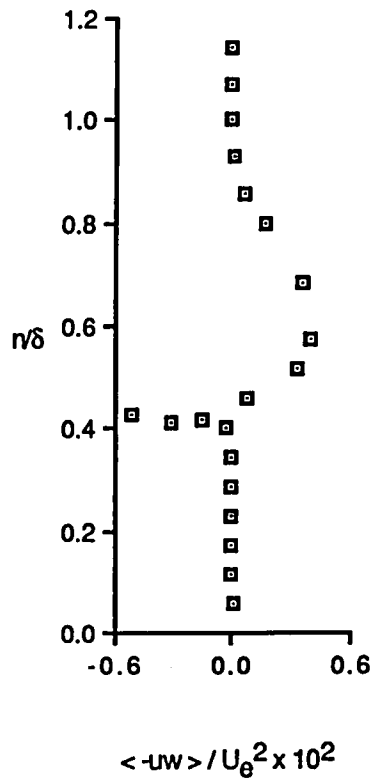


Figure 18.(cont'd)- Distribution of Reynolds shear stresses (Station numbers refer to Table 1 and Fig. 5).

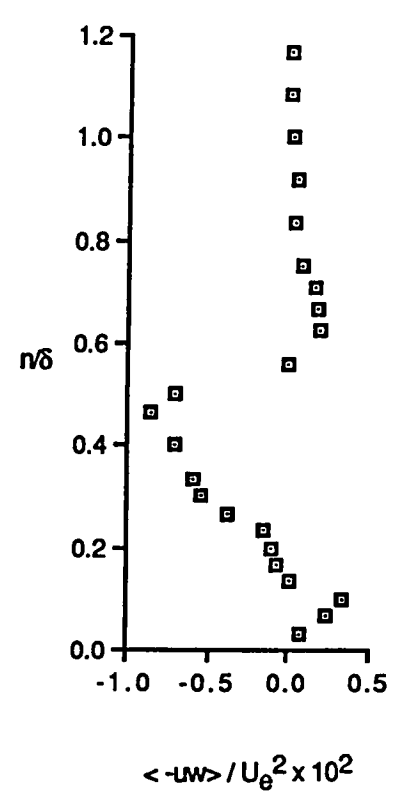
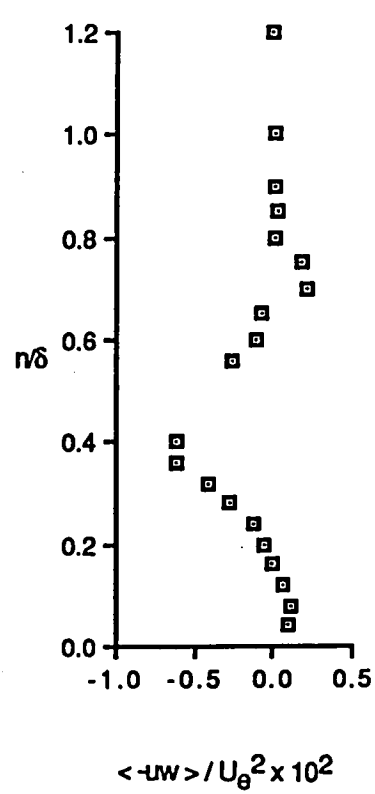
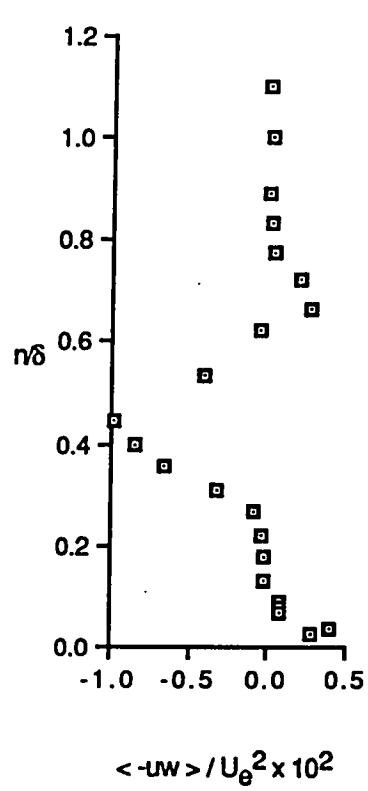


Figure 18.(cont'd)- Distribution of Reynolds shear stresses (Station numbers refer to Table 1 and Fig. 5).

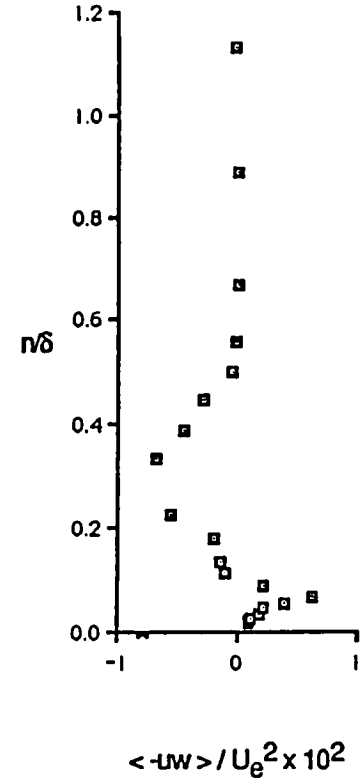
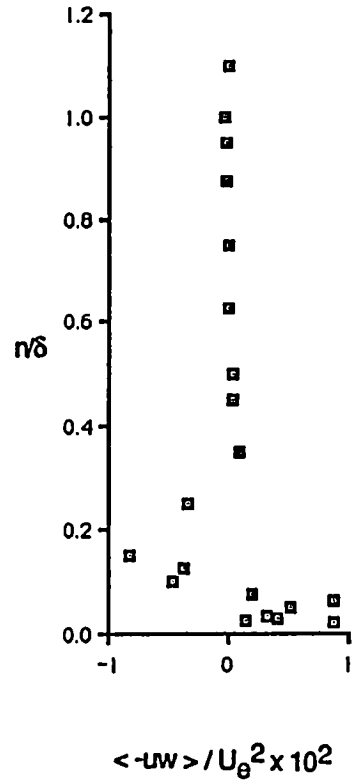
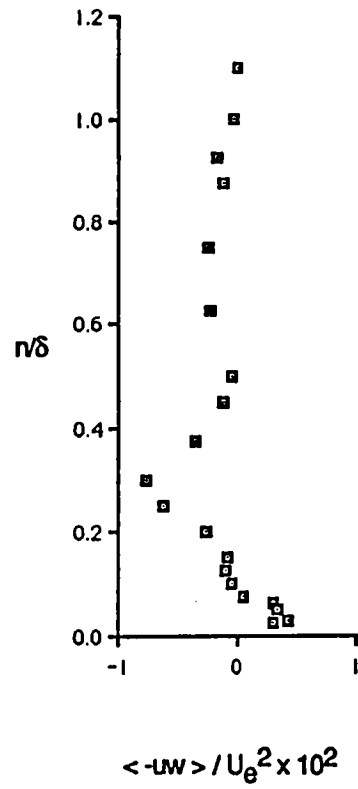


Figure 18.(cont'd)- Distribution of Reynolds shear stresses (Station numbers refer to Table 1 and Fig. 5).

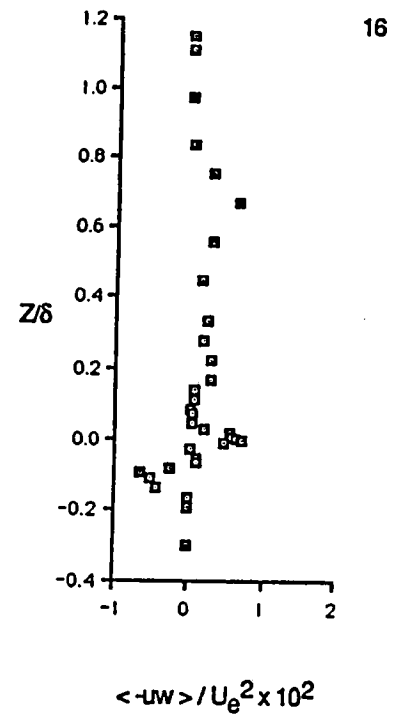
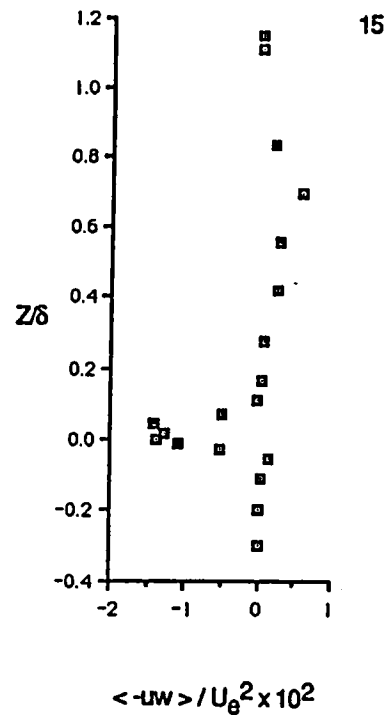
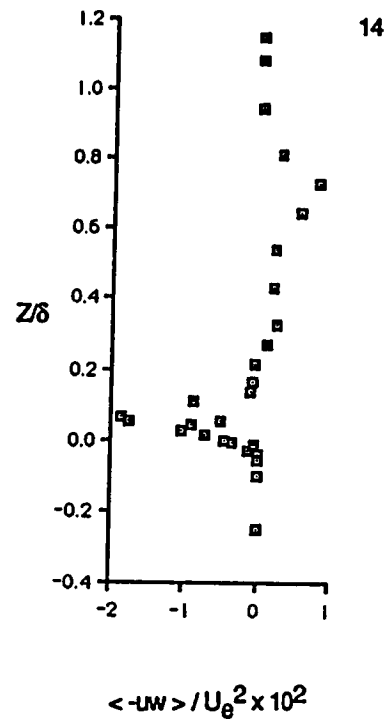
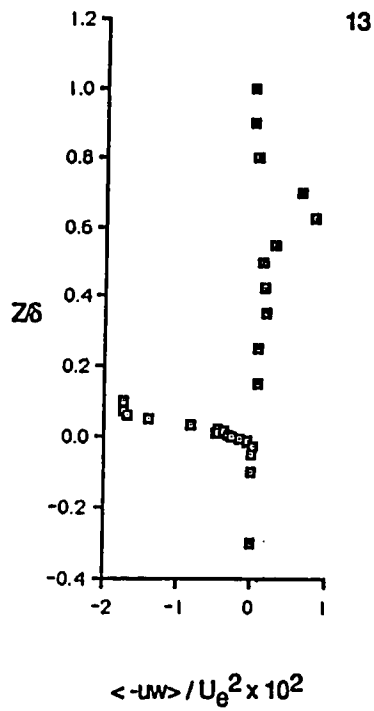
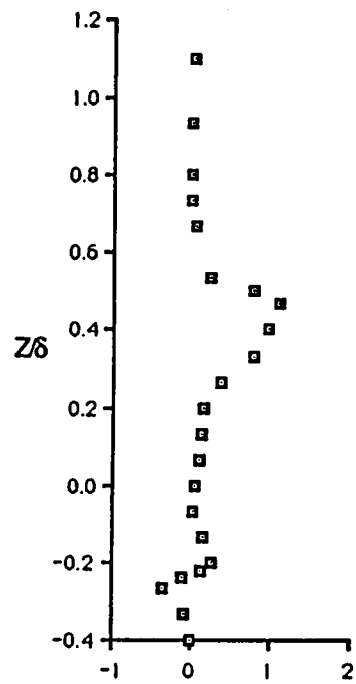
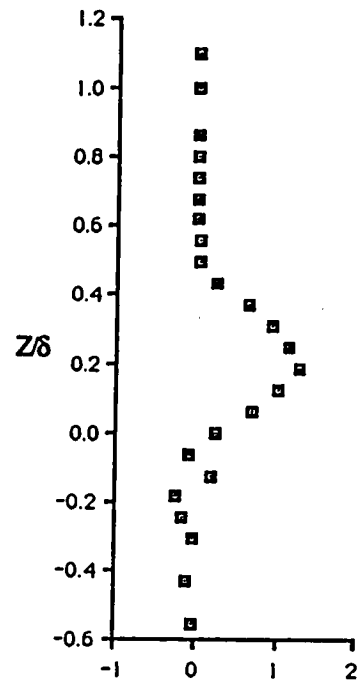
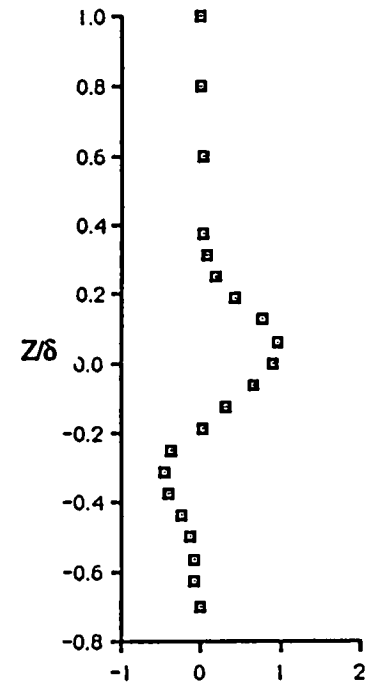


Figure 18.(cont'd)- Distribution of Reynolds shear stresses (Station numbers refer to Table 1 and Fig. 5).



$$\langle -uw \rangle / U_e^2 \times 10^2$$


$$\langle -uw \rangle / U_e^2 \times 10^2$$


$$\langle -uw \rangle / U_e^2 \times 10^2$$

Figure 18.(cont'd)- Distribution of Reynolds shear stresses (Station numbers refer to Table 1 and Fig. 5).

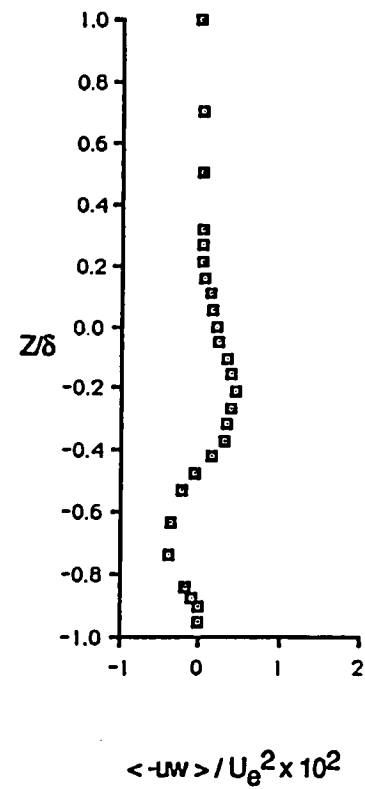
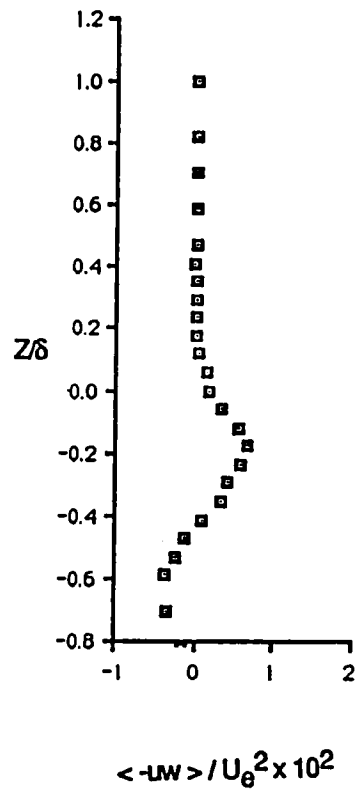
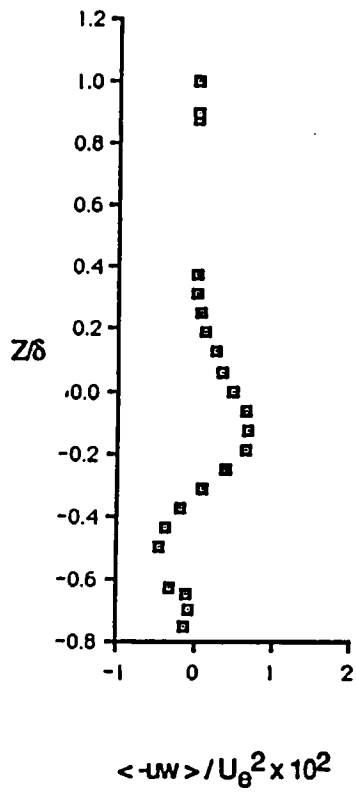


Figure 18.(concluded)- Distribution of Reynolds shear stresses (Station numbers refer to Table 1 and Fig. 5).

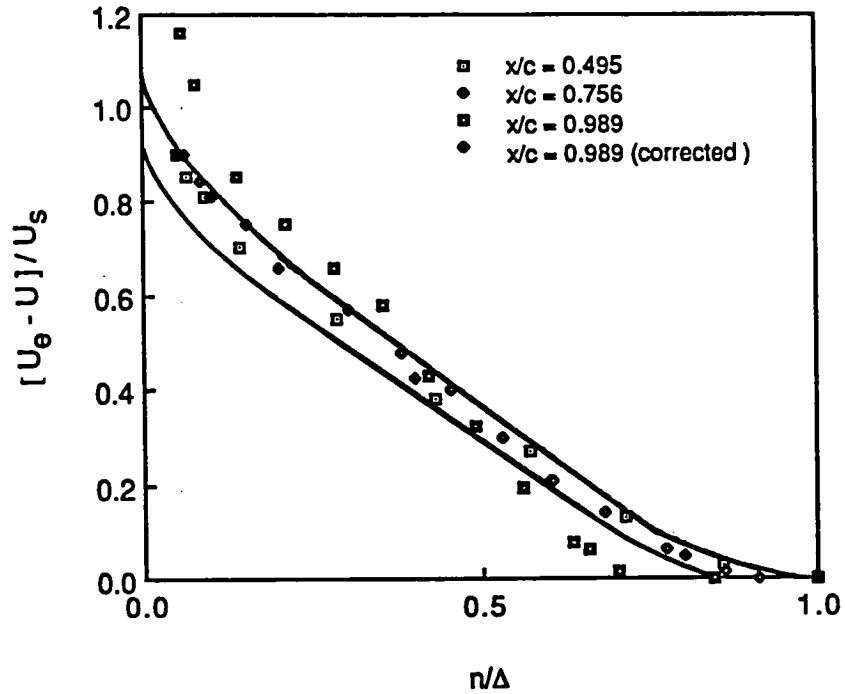


Figure 19.- Mean velocity profiles normalized by Perry-Schofield (1973) profile. Solid lines are the limits of scatter in data used by Perry and Schofield.

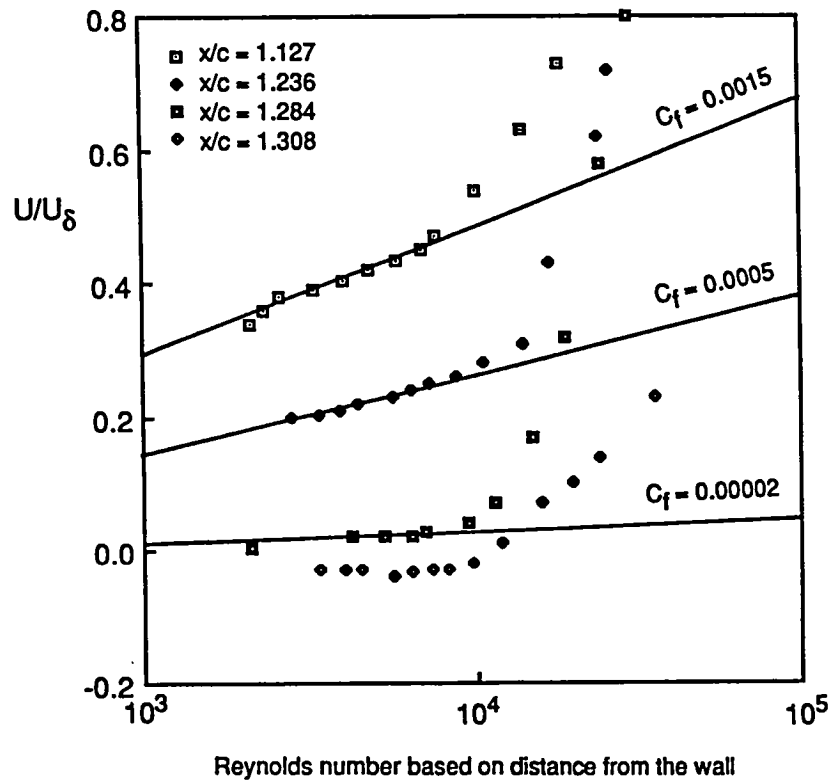


Figure 20.- Near-wall mean velocities upstream of and in the vicinity of the backflow.

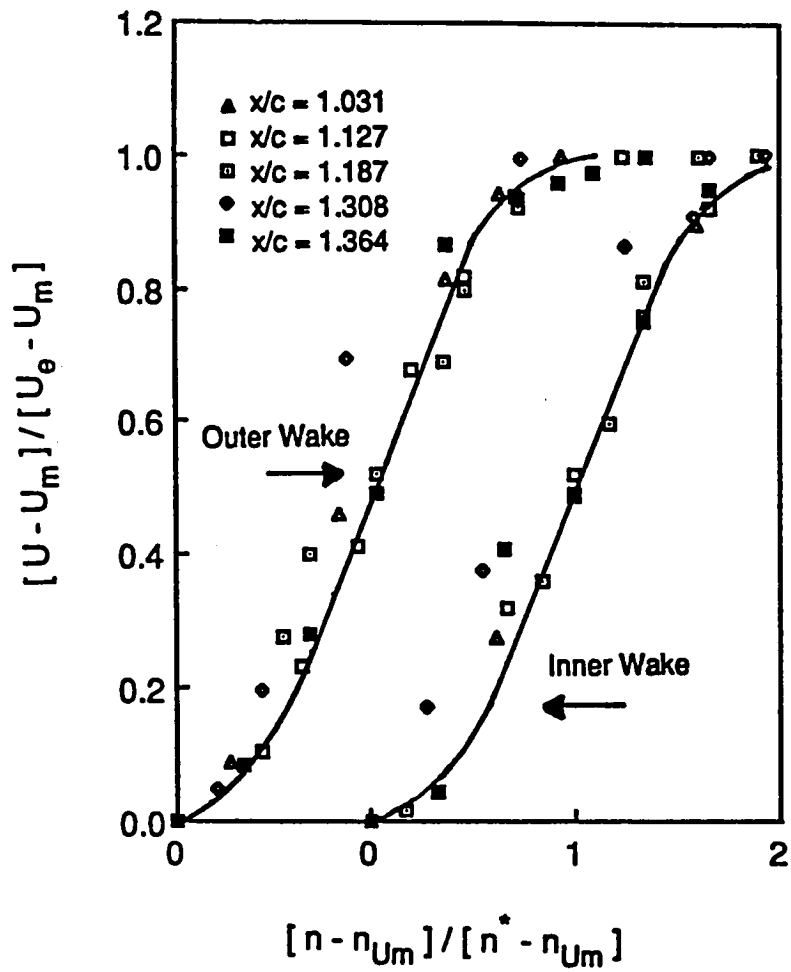


Figure 21.- The velocity distribution in the main airfoil wake. Solid lines derived from Equation 4.

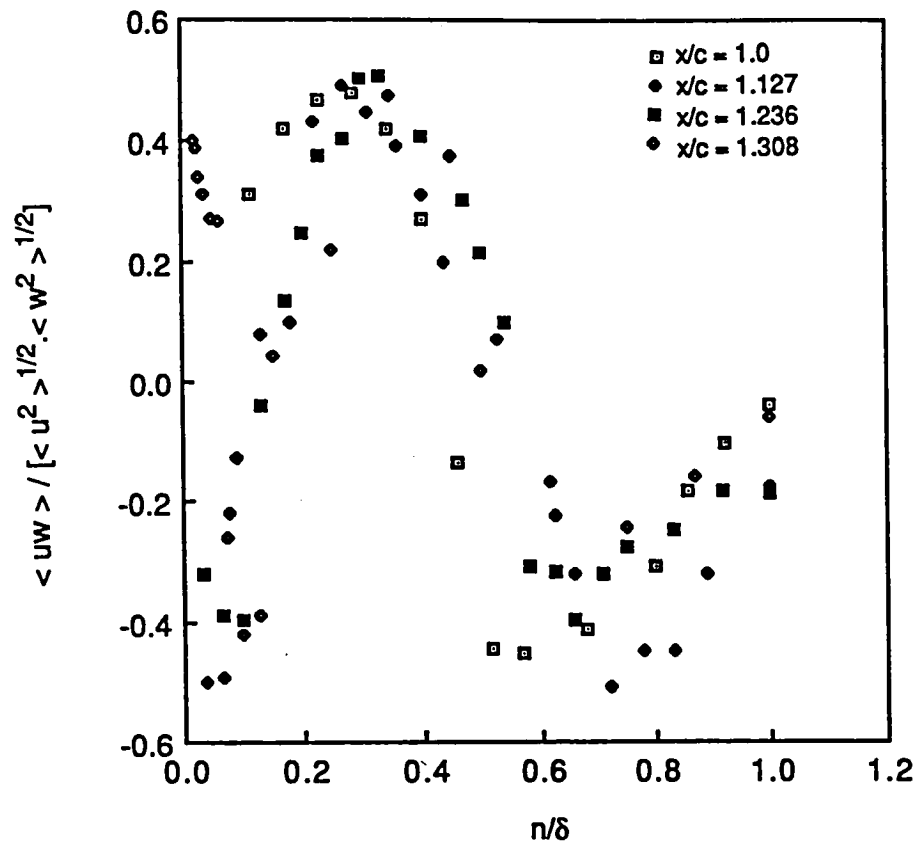


Figure 22.- Shear correlation coefficient.

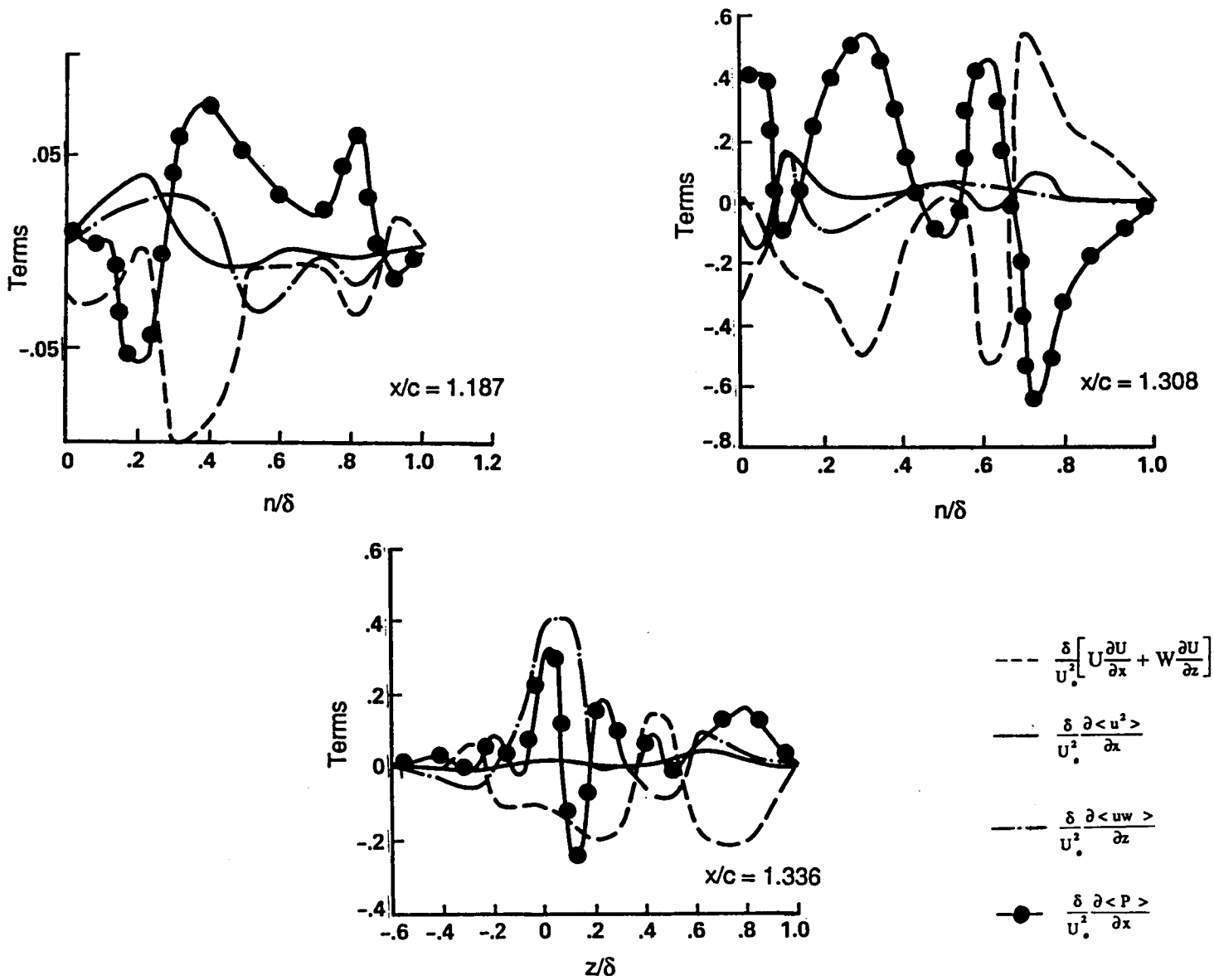


Figure 23.- Terms in the streamwise momentum transport equation.

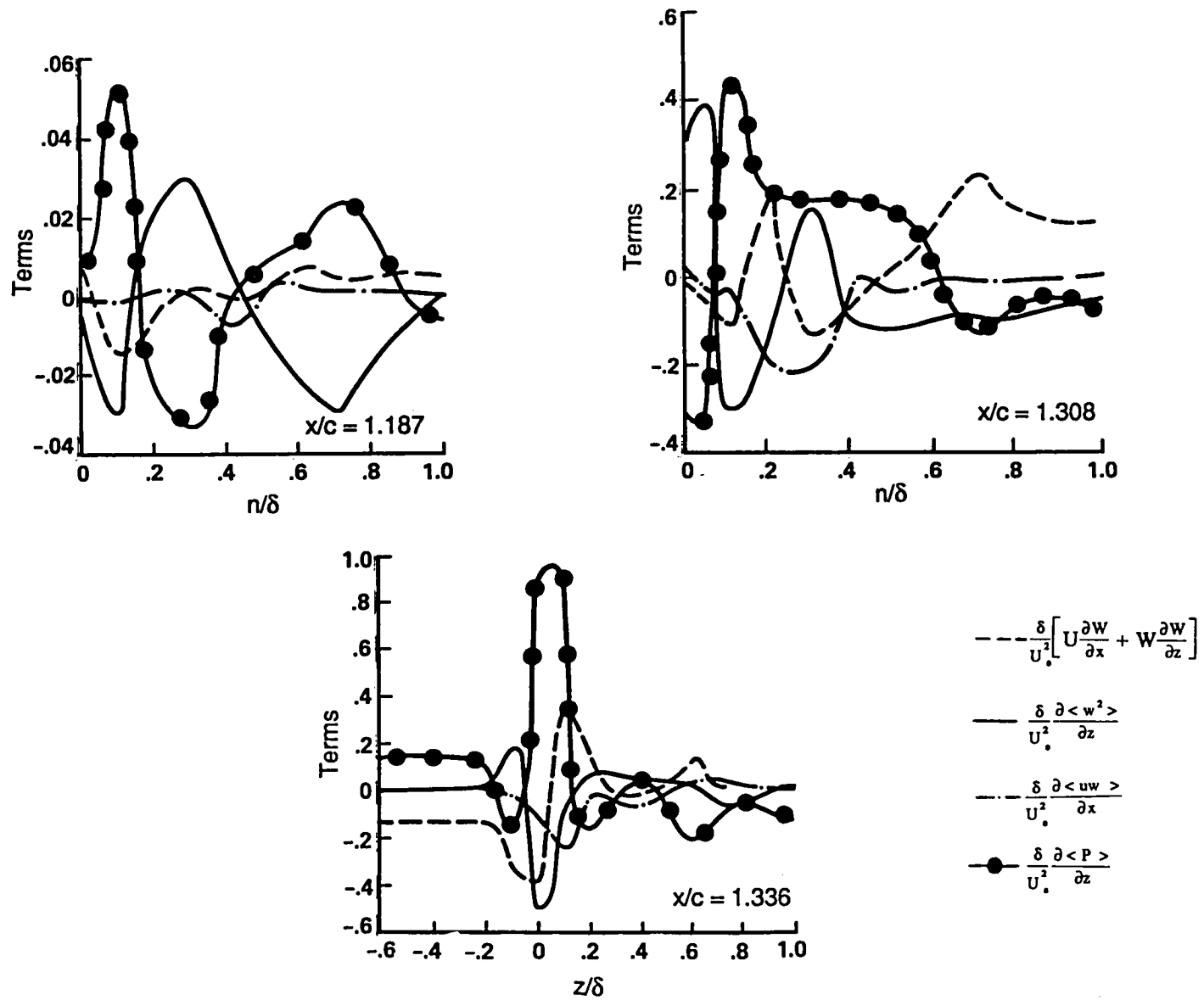


Figure 24.- Terms in the cross-stream momentum transport equation.

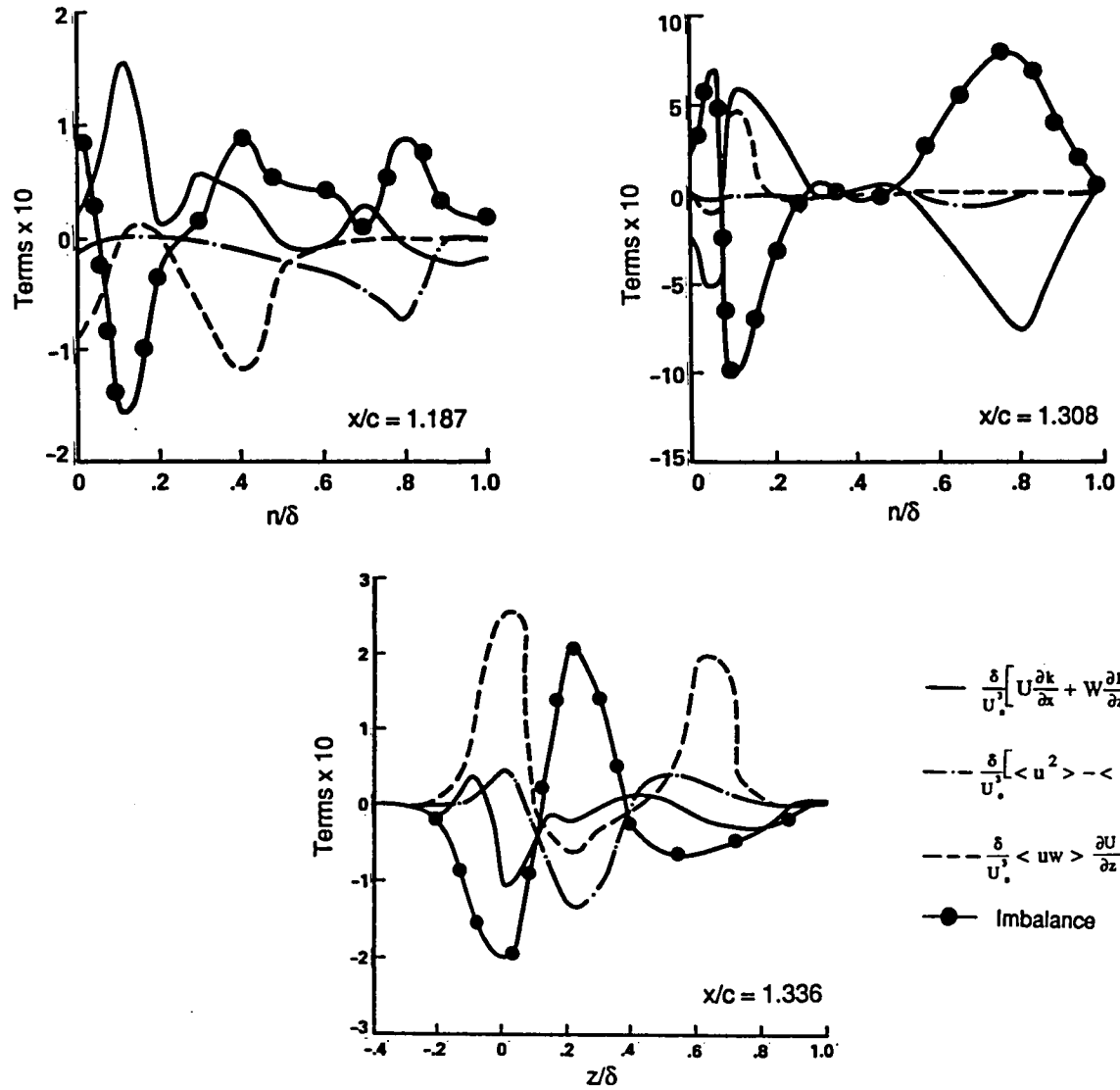


Figure 25.- Terms in the turbulence kinetic energy transport equation.



Report Documentation Page

1. Report No. NASA TM-100053		2. Government Accession No.		3. Recipient's Catalog No.	
4. Title and Subtitle Characteristics of Merging Shear Layers and Turbulent Wakes of a Multi-Element Airfoil				5. Report Date February 1988	
				6. Performing Organization Code	
7. Author(s) Desmond Adair and W. Clifton Horne				8. Performing Organization Report No. A-88048	
				10. Work Unit No. 505-60-21	
9. Performing Organization Name and Address Ames Research Center Moffett Field, CA 94035				11. Contract or Grant No.	
				13. Type of Report and Period Covered Technical Memorandum	
12. Sponsoring Agency Name and Address National Aeronautics and Space Administration Washington, DC 20546-0001				14. Sponsoring Agency Code	
15. Supplementary Notes Point of Contact: W. Clifton Horne, Ames Research Center, MS 247-2 Moffett Field, CA 94035 (415) 694-6680 or FTS 464-6680					
16. Abstract <p>Flow characteristics in the vicinity of the trailing edge of a single-slotted airfoil flap are presented and analyzed. The experimental arrangement consisted of a NACA 4412 airfoil equipped with a NACA 4415 flap whose angle of deflection was 21.8°. The flow remained attached over the model surfaces except in the vicinity of the flap trailing edge where a small region of boundary-layer separation extended over the aft 7% of flap chord. The flow was complicated by the presence of a strong, initially inviscid jet emanating from the slot between airfoil and flap, and a gradual merging of the main airfoil wake and flap suction-side boundary layer. Downstream of the flap, the airfoil and flap wakes fully merged to form an asymmetric curved wake.</p> <p>The airfoil configuration was tested at an angle of attack of 8.2°, at a Mach number of 0.09, and chord based Reynolds number of 1.8×10^6 in the Ames Research Center 7- by 10-Foot Wind Tunnel. Surface pressure measurements were made on the airfoil and flap and on the wind tunnel roof and floor. It was estimated that the wall interference increased the C_L by 7% and decreased the C_M by 4.5%. Velocity characteristics were quantified using hot-wire anemometry in regions of flow with preferred direction and low turbulence intensity. A 3-D laser velocimeter was used in regions of flow recirculation and relatively high turbulence intensity.</p> <p>Detailed measurements of pressure and velocity characteristics are reported in the following sections with emphasis on flow over the suction surface of the flap and in the downstream wake. The relative importance of the terms in the momentum and turbulence kinetic energy equations is quantified for flow in the vicinity of the flap trailing edge.</p>					
17. Key Words (Suggested by Author(s)) Turbulent separated flow Multi-element airfoil 3-D laser velocimeter			18. Distribution Statement Unclassified-Unlimited Subject Category - 34		
19. Security Classif. (of this report) Unclassified		20. Security Classif. (of this page) Unclassified		21. No. of pages 78	22. Price AO-5